Department of Physics and Astronomy

University of Heidelberg

Master thesis

in Physics

submitted by

Marvin Holten

born in Heidelberg

2017

Collective Modes and Turbulence in Two-Dimensional Fermi Gases

This Master thesis has been carried out by Marvin Holten

at the

Physikalisches Institut Heidelberg

under the supervision of

Prof. Dr. Selim Jochim

Collective Modes and Turbulence in Two-Dimensional Fermi Gases:

Collective modes are an essential instrument for the study of many-body systems and provide access to many observables like for example the equation of state. In this thesis we explore collective modes of a quasi-two-dimensional Fermi gas in a harmonic confinement in general and from the viewpoint of turbulence in particular. Turbulence represents a field that has always been elusive to theoretical descriptions and that to date relies primarily on experimental observations.
We have studied the interaction dependence of the monopole and quadrupole modes with unprecedented accuracy and have been able to extend existing measurements in this field to both lower temperatures and to the bosonic regime. We present the first clear evidence for a previously unobserved quantum anomaly predicted to occur in two dimensions. In addition we present the first measurements of the quadrupole mode far in the hydrodynamic limit and compare them to kinetic theory. To find evidence for turbulent dynamics we have studied the collective modes in both real and momentum space and extracted different observables as for example the energy spectrum of the cloud. We came to the conclusion that these lowest order collective modes are inapplicable for the excitation of turbulence. At the end of this thesis an add-on to our experimental apparatus is presented. This new setup provides us with experimental capabilities that we will use to tailor time-dependent potentials and to excite turbulence in our cloud in the future.

Kollektive Moden und Turbulenz in Zweidimensionalen Fermi Gasen:

Kollektive Moden sind ein unverzichtbares Mittel zur Untersuchung von Vielteilchensystemen und liefern Zugang zu vielen Observablen wie zum Beispiel der Zustandsgleichung. In dieser Arbeit untersuchen wir kollektive Moden eines zweidimensionalen Fermi Gases in einem harmonischen Potential im Allgemeinen und im Hinblick auf Turbulenz. Wir haben die Abhängigkeit der Mono und Quadrupol Mode von Wechselwirkungen mit beispielloser Präzession untersucht und konnten die schon existierenden Messungen in diesem Feld hin zu niedrigeren Temperaturen sowie auch in den bosonischen Bereich erweitern. Wir präsentieren die ersten deutlichen Anzeichen einer Quanten Anomalie, die in zwei Dimensionen vorhergesagt wurde, aber bisher nicht beobachtet werden konnte. Zusätzlich zeigen wir die ersten Messungen der Quadrupole Mode weit im hydrodynamischen Bereich und vergleichen diese mit der kinetischen Gastheorie. Um Anzeichen für Turbulenz zu finden haben wir die kollektiven Moden sowohl im Orts- als auch im Impulsraum untersucht und Observablen wie das Energiespektrum extrahiert. Wir schließen, dass diese kollektiven Moden niedrigster Ordnung für die Anregung von Turbulenz ungeeignet sind. Am Ende dieser Arbeit wird eine Erweiterung unseres experimentellen Aufbaus vorgestellt. Wir planen die Fähigkeiten zur Erzeugung von zeitabhängigen Potentialen, die wir durch den Umbau erwerben, in naher Zukunft für die Anregung von Turbulenz in unserem Gas zu nutzen.

Contents

1 Introduction

1.1 Systems out of Equilibrium

The most common description of quantum many-body systems relies on statistical ensembles and provides predictions about statistic properties like energy and particle number in equilibrium or linear response functions. The dynamic evolution of such systems far from equilibrium and how they eventually reach some equilibrium state is far less well understood in general [Eis15]. Equilibrium states constitute only a tiny amount of the available phase space for quantum many body systems. Therefore, it is desirable to improve our general understanding of far from equilibrium dynamics. Consequently, many of the topics that currently attract large attention in physics are directly connected to non-thermalized systems. Examples include time crystals [Cho17; Zha17], many body localization [Sch15; Smi16] or transport properties in general.

A remarkable attribute of quantum systems very far from equilibrium is that they often show universal scaling behaviour. The latter can be described in the framework of so-called *non-thermal fixed points*. The time evolution of systems that are excited close to such fixed points back to equilibrium shows a *critical slow down* and correlations in the system follow universal scaling laws [Now13]. One particular case that is ubiquitous in nature and where self-similar and universal dynamics are generally observed very far from thermal equilibrium is turbulence in fluids.

In a classical picture hydrodynamic turbulence can be understood from the viewpoint of symmetries [Fri95]. At low velocities the flow of a fluid is laminar and it exhibits all the symmetries of the Hamiltonian. If the velocity of the fluid increases, the flow becomes unstable at some point and the symmetries of the Hamiltonian are broken. This regime represents one of the greatest remaining scientific challenges in classical physics and as of yet no complete theories could be developed.

Finally, when increasing the flow velocity even further, the symmetries of the Hamiltonian are restored in a statistical sense and a probabilistic theory becomes applicable. There are currently no theories that can make reliable predictions about the critical velocities at which the transitions from one to another regime of turbulent flow occur. As a result, the field of turbulence relies on and is driven by experimental observations to a very large extent.

The discovery of the superfluid phase of helium in 1938 has brought the whole new field of quantum turbulence to life [All38; Kap38]. The most important difference of superfluid and classical flow is that vorticity is always quantized in the former. As a result, turbulence in superfluids can be pinned down to the presence of phase defects in the form of vortices. For many years helium was the only experimentally available superfluid in nature and most if not all of our current understanding of quantum turbulence originates from helium experiments. This includes questions like what mechanism for dissipation exists in superfluids and to what extent they satisfy the correspondence principle. However, experiments in helium also come with a few drawbacks like very small vortex cores that cannot be observed directly and no control over interactions or the dimensionality. Therefore many open questions in the field remain.

With the first experimental realization of a Bose-Einstein condensate (BEC) in a cold atom gas and the subsequent proof of its superfluid character in 2005 a new exciting era for the field of quantum turbulence has yet begun again [Dav95; Zwi05]. Experiments with cold gases provide a large amount of control over many of the system parameters that are fixed in the case of superfluid helium. Thus they could advance the field of turbulence by a significant amount. Very recently, the first experimental efforts in this direction started and it has been shown that it is in fact possible to excite turbulence in cold gases [Tsa15].

In this thesis we explore the feasibility of exciting quantum turbulence in our current experimental setup in an ultracold two component Fermi gas that is confined to two dimensions. Two component fermionic fluids are special from the viewpoint of turbulence since they can undergo a phase transition into a superfluid with the highest known vortex density. Additionally, the restriction to two dimensions has important implications on the vortex dynamics as we will discuss at a later point. All the turbulence experiments in cold atom clouds to date were performed with bosonic particles while turbulence in ultracold Fermi gases is an experimentally completely unexplored area as of yet. We hope that our efforts in this direction could lead to the first experimental observation of turbulence in the two dimensional BEC-BCS crossover. One open question in this regime is, for example, whether the superfluid BCS state can even survive a turbulent excitation.

All the measurements that were performed during the work for this thesis were executed by exciting different collective modes in a two dimensional harmonic confinement. We explored to what degree these collective modes are useful for the excitation of turbulent states in our cloud. To this end a very precise characterisation of the dynamics in both position and momentum space was performed. We were not able to observe evidence for turbulence as of yet, however we are very confident that building on this work the first observation of turbulence in our experiments is imminent.

1.2 Outline

In the first chapter of this thesis we will provide an overview over the field of turbulence in general. To this end, the most important results of classical turbulence are recalled and sequentially compared to the situation in superfluids. For both cases the most important regimes and scales of turbulence will be discussed. After this general introduction, we focus on features that are important in the context of our experiment, namely turbulence in reduced dimensions and in cold atom clouds. At the end of the chapter we will present some of the experiments that were realised within the cold atom community so far and discuss open questions in the field.

In chapter 3 we present the current state of our experimental setup and the most important experimental tools that are used for preparing and detecting ultracold atom clouds. Additionally, a brief derivation of the theoretical framework that is needed to describe such experiments is given. This includes the most important interaction and temperature scales for cold Fermi gases.

Afterwards, all the experimental results are presented in chapter 4. We will discuss the different excitation procedures that were used for the excitation of collective modes. A very precise characterization of the latter was performed and the dependence of their dynamics on inter-particle interactions will be discussed. We also present momentum distributions of the collective modes that were measured to search for evidence of turbulent dynamics. At the end of chapter 4 we will present some initially unexpected behaviour of the breathing mode in our trap that we spotted in our experiment recently.

At the end of this thesis an outlook on the future plans for our experimental setup is given. During the work for this thesis a large add-on to the experimental setup was designed. The main components of this extension, namely a high resolution objective, a new camera and a spatial light modulator, are presented at this point. Our initial intention was to use the new experimental capabilities that we gain in this way for the assembly of many-body states at extremely low entropy. With respect to this thesis we will also explore how the add-on can be used for creating and detecting turbulence in the near future.

2 Introduction to Turbulence

2.1 Classical Turbulence

Turbulent behaviour is observed across all length scales in nature, starting from everyday phenomena like the plume rising from a candle to weather phenomena in the atmosphere and finally to the dynamics of interstellar gases on vast distances (see Figure 2.1). Existing on all these length scales, turbulence has had a crucial influence on forming the universe as we observe it today. It plays an important role in the formation of galaxies [Kru05] and drives essential mechanisms for life on earth, for example the distribution of seeds and pollen [Oku89].

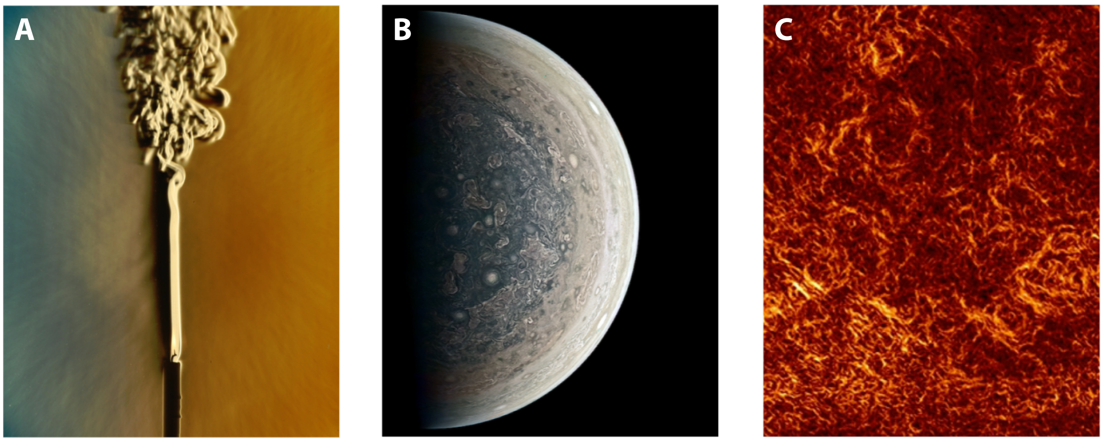

Figure 2.1: **A:** The plume rising from a candle shows a transition from laminar to turbulent flow at a fixed distance from the flame. The transition occurs because the gas accelerates as it moves upwards. Taken from [Set09].
B: This picture taken by NASA's Juno spacecraft shows large turbulent storms in atmosphere at the south pole of Jupiter. Taken from [Nas17].
C: Polarization gradient measurement of interstellar gas reveal turbulent motions on length scales ranging from 1000 km up to 100 parsecs (10^{18} m). Taken from [Gae11].

This ubiquitous nature of turbulence brings up the question to what extent it is already part of the fundamental laws of nature, i.e. in quantum mechanics. Cold atom systems are especially suited to investigate this matter since they provide a large degree of control over the system and direct access to the most important observables such as the momentum distribution. Recently, several cold atom experiments, some of which will be discussed at a later point, were able to observe evidence for turbulent behaviour in degenerate bose and fermi gases [Hen09; Nee13; Nav16].

Here, we focus on the special case of strongly correlated fermions in two dimensions. This case is of special interest because the early universe consisted of a strongly interacting quark gluon plasma with fluid dynamics that are possibly very similar to those of fermionic cold atom systems [Ada12]. Understanding how turbulence emerges in these strongly correlated systems could lead to a better understanding of the dynamics in the early universe and in high energy collision experiments, in the long run.

In order to search for evidence for turbulence in quantum degenerate systems, it is first necessary to specify what we mean exactly by the term turbulence. After defining the term, we will recall some results of classical hydrodynamics to be compared with the quantum mechanical picture in the following section. Afterwards, we focus on the effects that are special for two-dimensional systems. A thorough derivation of the results, that are recalled in the following sections, can be found in textbooks on hydrodynamics [Lan87; Fri95] or numerous reviews on the matter [Kra80; Bof12].

2.1.1 Definition of Turbulence

In contrast to the order parameter of a phase transition, there is no single physical quantity which determines whether a physical system is turbulent or not. As a result, no consensus exists on how to define the term turbulence. Yet, the main features of turbulence are agreed upon. We will follow the definition suggested by Tsatsos et al. [Tsa15] here:

> *Turbulence is the time-dependent, space-dependent state of irregular motion, characterized by a huge number of degrees of freedom which interact via the fundamental non-linearity of the Euler equation.*

It is important to note that this definition does not limit turbulence to fluid motion but also covers other systems like electromagnetic waves or neurons which can show such a behaviour [Pao11]. The restriction to the non-linearity of the Euler-Equation (i.e. of the form $(\boldsymbol{v} \cdot \nabla)\boldsymbol{v}$) keeps the definition from becoming too generic (otherwise any nonlinear system with many degrees of freedom would be turbulent) [Tsa15].

2.1.2 Classical Description

Following Landau and Lifshitz [Lan87], under given steady boundary conditions a steady solution of the equations of motion (here: *Euler equation*) must exist for any hydrodynamic system. Yet, these solutions will only occur in nature if they are also stable. Stability means that small perturbations of the flow Δv decay quickly in time. If, in contrast, these perturbations grow indefinitely with time, then the flow solution is unstable and can not actually exist — the system will become turbulent instead.

A mathematical derivation of stability is very difficult and still unsolved for many important cases (for example the flow of a fluid around a finite sized obstacle). Instead, the *Reynolds number* defined as

$$R = \frac{\rho v d}{\eta}, \tag{2.1}$$

where ρ is the fluid density, v the flow velocity, η the viscosity and d the characteristic length of the system (for example the obstacle size) is used to estimate if the flow is turbulent. The Reynolds number is given by the ratio of the largest to the smallest eddy currents in the fluid, approximately. In general, systems with large Reynolds numbers tend to show turbulent flow, while low Reynolds numbers indicate that stable laminar flow solutions exist. The critical value R_{crit} where the system changes its behaviour has to be determined for each class of systems empirically.

The next question arising immediately, is how one can describe a system once it is in a state of so-called *fully developed turbulence* where $R > R_{\text{crit}}$ holds. Because of the interplay between a large range of length scales and the chaotic character of the motion, perturbative approaches break down [Pao11]. Since complete solutions are not known to date either, there exists no quantitative theory of turbulence at the moment [Lan87]. Nevertheless, a probabilistic description, which yields several quantitative predictions of averaged quantities like the energy spectrum, has been developed [Fri95].

2.1.3 Turbulent Cascades

Starting with the simplest case of an incompressible fluid in three dimensions and following Nazarenko [Naz11], we define the energy spectrum as follows:

$$E^{3\mathrm{D}}(\boldsymbol{k}) = \frac{1}{2}\int\limits_{\mathbb{R}^3} \langle \mathbf{u}(\boldsymbol{x}) \cdot \mathbf{u}(\boldsymbol{x}+\boldsymbol{r})\rangle\, e^{-i\boldsymbol{k}\cdot\boldsymbol{r}} \frac{d\boldsymbol{r}}{(2\pi)^3}, \tag{2.2}$$

where $\mathbf{u}(\boldsymbol{x})$ is the local velocity of the fluid at position $\boldsymbol{x}$. As a consequence $E^{3\mathrm{D}}(\boldsymbol{k})$ represents the kinetic energy density per unit mass in $\boldsymbol{k}$-space. In the case of *homogeneous* and *isotropic* turbulence the $\boldsymbol{x}$ and direction of $\boldsymbol{k}$-dependence drop out ($E^{3\mathrm{D}}(\boldsymbol{k}) \equiv E^{3\mathrm{D}}(k)$) and we get:

$$\frac{\mathrm{E_{kin}}}{m} = \int\limits_{\mathbb{R}^3} E^{3\mathrm{D}}(\boldsymbol{k})\; d\boldsymbol{k} = \int\limits_0^\infty E^{1\mathrm{D}}(k)\; dk. \tag{2.3}$$

Here, we defined the 1D energy spectrum $E^{1\mathrm{D}}(k)$ as:

$$E^{1\mathrm{D}} := 4\pi k^2 E^{3\mathrm{D}}(k)\,. \tag{2.4}$$

A general prediction on the dependence of this one dimensional energy spectrum on k was first made by Kolmogorov [Kol41] based on the cascade picture of Richardson [Ric26]. Richardson tried to describe turbulence in the picture of locally interacting eddy currents in the fluid (see Figure 2.2 A). In his picture eddy currents at large length scales are created by some driving force which adds energy to the system. These large eddy currents subsequently decay into smaller and smaller ones until viscous dissipation kicks in at some small length scale (also known as Kolgomorov length scale η). This flow of energy from large to small length scales through the decay of vortices in the system is known as *Richardson-* or *direct cascade*.

Based on the assumption that these eddy currents interact only locally in momentum space, meaning they interact only with similar sized eddy currents, Kolmogorov formulated his famous $-5/3$ law (also known as *K41-law*) [Kol41]. The main result is quickly recovered by a dimensional analysis, presented in the following.

Since the interaction of eddy currents is local, the turbulence properties within the *inertial range* l with $l_{\mathrm{drive}} \gg l \gg \eta_{\mathrm{visc}}$ (or accordingly in k-space $k_{\mathrm{drive}} < k < k_{\mathrm{visc}}$) depend only on the energy cascade rate ε while the details of the drive and dissipation dynamics do not matter. By this argument, the one dimensional kinetic energy

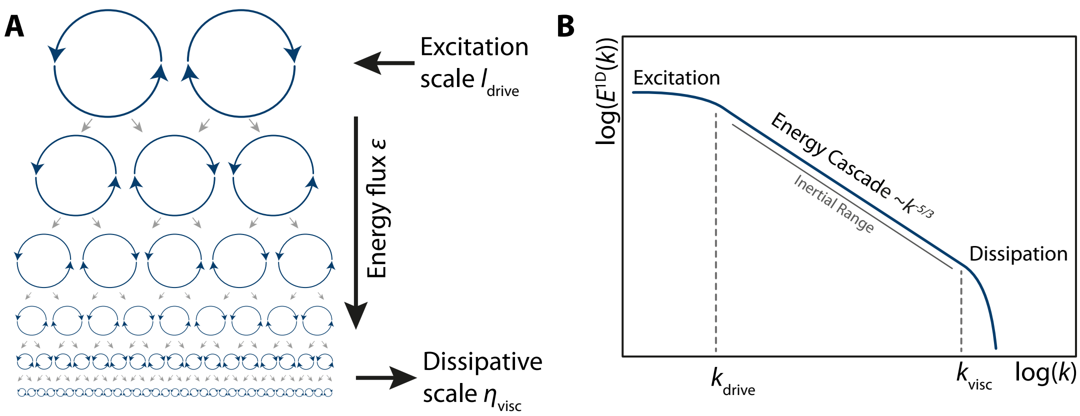

Figure 2.2: **A:** Richardsons picture of turbulence. Energy is injected into the system at some lengthscale l_{drive} and moves down to smaller and smaller scales until it is dissipated at some scale η_{visc}.
B: Prediction of the energy density spectrum $E^{1\mathrm{D}}(k)$ for a three dimensional incompressible fluid with fully developed turbulence by the Kolmogorov law. In the inertial range between k_{drive} and k_{visc} the only relevant scale is the energy cascade rate which leads to the fixed exponent of $-5/3$.

density should only depend on k and ε as these are the only remaining quantities of the system

$$E^{1\mathrm{D}} \propto \varepsilon^{\alpha} k^{\beta}. \tag{2.5}$$

Comparing the dimensions on both sides of the equation, i.e. $\left[E^{1\mathrm{D}}\right] = \frac{l^3}{t^2}$, $[\varepsilon] = \frac{l^2}{t^3}$ and $[k] = \frac{1}{l}$, we arrive at

$$E^{1\mathrm{D}} = C \cdot \varepsilon^{3/2} k^{-5/3} \tag{2.6}$$

as only possible solution under the previous assumptions. The constant factor C of order one is also known as *Kolgomorov Constant*. The general form of this energy spectrum for an incompressible fluid in three dimensions is depicted in Figure 2.2 B.

Since Kolgomorov developed his theory in 1941, countless experiments have verified his energy cascade picture and often the $k^{-5/3}$ dependence is observable over many orders of magnitude (see Figure 2.3). As a result, power-law dependencies in the momentum or energy density are now often interpreted as indication for turbulent motion in the system [Zak92].

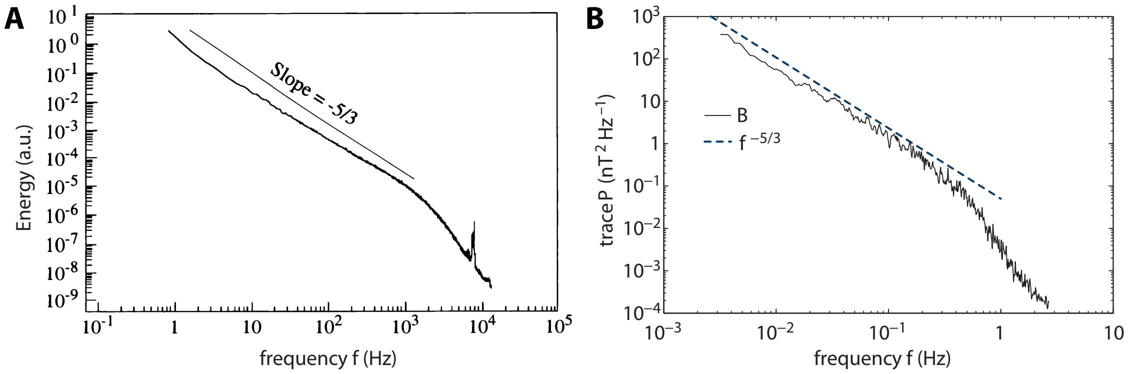

Figure 2.3: Kolgomorovs power law prediction for the energy spectrum of turbulence could be verified by various experiments, for example in wind tunnel setups **A** [Ans84] or in the spectrum of the solar wind **B** [Gol15].

Nevertheless, many systems also show deviations from the simple Kolgomorov spectrum. These can come from additional conserved quantities like the enstrophy in two dimensions, discussed later, or from the so-called turbulent intermittency phenomenon [Fri95]. In general, also quantum degenerate gases fall into the category of systems where the simple Richardson cascade picture breaks down. This can be understood easily because in the superfluid phase all the particles are described by a single wavefunction and spatially extended vortices are not the correct language to describe the system any more. In the next section we will take a closer look at this special case of *quantum turbulence*.

2.2 Quantum Turbulence

Even though the definition of turbulence introduced above is applicable to arbitrary quantum systems, the term *quantum turbulence* is usually associated with turbulence of superfluids in particular. In 1955 Richard Feynman was among the first to realize that despite of the absence of viscosity in a superfluid it can nevertheless show turbulent behaviour through interaction of vortices [Fey55]. The reason why the notion of *quantum turbulence* instead of *superfluid turbulence* has established itself, is that, interestingly enough, the quantization and not the superfluidity is the relevant feature of these systems, as will be discussed later [Tsa15].

We will begin this section by recalling some basics about vortices in superfluids. Afterwards, the energy spectra for different cases of quantum turbulence are discussed. In the limit of many quanta one usually expects that the quantum systems approximate their classical counterpart [Pao11] and we will discuss to what extent this *correspondence principle* is realised in quantum turbulence. Finally, the experimental progress to date and remaining open questions in the field are reviewed. Excellent, in-depth reviews on quantum turbulence are found in [Skr11; Pao11; Tsa15].

2.2.1 Vorticity in Superfluids

Superfluidity is usually explained in the context of Bose-Einstein condensation. At some temperature T_C, when the thermal de Broglie wavelength $\lambda_{\text{th}} = h/\sqrt{2\pi k_\text{B} T}$ becomes of the order of the inter-particle spacing $1/\rho^{-1/3}$, a gas of interacting bosonic particles exhibits a second-order phase transition into a *condensed phase*. This transition is connected to a macroscopic occupation of the ground state and thus the complete system can be approximated by a single wavefunction

$$\Psi\left(\boldsymbol{r},t\right) = \sqrt{\rho(\boldsymbol{r},t)}e^{i\phi(r,t)}, \tag{2.7}$$

where ρ is the normalized condensate density and ϕ the condensate phase. Using this description we can derive the probability current $\boldsymbol{j}$ in the system as

$$\boldsymbol{j}\left(\boldsymbol{r},t\right) := \frac{\hbar}{2mi}\left(\Psi^*\nabla\Psi - \Psi\nabla\Psi^*\right) = \rho(\boldsymbol{r},t)\frac{\hbar}{m}\nabla\phi(\boldsymbol{r},t). \tag{2.8}$$

The probability current describes the flux of the probability density $\rho = |\Psi|^2$ and obeys the continuity equation:

$$\frac{\partial\rho(\boldsymbol{r},t)}{\partial t} + \nabla\cdot\boldsymbol{j(r,t)=0}. \tag{2.9}$$

Comparing this to the continuity equation of classical hydrodynamics ($\partial\rho/\partial t + \text{div}(\rho\boldsymbol{v}) = 0$) motivates the definition of the superfluid velocity

$$\boldsymbol{v}_\text{s}(\boldsymbol{r},t) := \frac{\boldsymbol{j}(\boldsymbol{r},t)}{\rho} = \frac{\hbar}{m}\nabla\phi(\boldsymbol{r},t). \tag{2.10}$$

It immediately follows that the velocity field of a superfluid has to be curl free, thus confirming the statement above that extended eddies do not exist in quantum fluids, since

$$\nabla \times \boldsymbol{v}_{\mathrm{s}} = \nabla \times \left(\frac{\hbar}{m} \nabla \phi \right) = 0. \tag{2.11}$$

This statement is, however, only true as long as the phase ϕ is continuous in its first two derivatives. Whereas a discontinuity of the phase at some point $\boldsymbol{r}$ in space is only physically consistent if the superfluid density ρ is zero at that same point.

This observation together with the fact that the wavefunction Ψ has to be single valued (a circulation along a closed path C has to leave Ψ invariant) lead Onsager in 1949 [Ons49] to the observation that the circulation Γ in a superfluid has to be quantized

$$\Gamma = \oint_C \boldsymbol{v}_{\mathrm{s}} \, d\boldsymbol{r} = \oint_C \frac{\hbar}{m} \nabla \phi \, d\boldsymbol{r} = \frac{\hbar}{m} \Delta \phi, \tag{2.12}$$

with $\Delta\phi = 2\pi n$ where n is an integer number and thus

$$\Gamma = \frac{2\pi\hbar}{m} n, \qquad n \in \mathbb{Z}. \tag{2.13}$$

This term is also known as the *Onsager-Feynman quantization condition.*

To summarize the derivation above, we see that circulation in superfluids is quantised and it can only be non-zero around so called *quantum vortices* with the geometry of lines in three dimensions and points in two dimensions, respectively. At the position of the vortex the velocity diverges, which is nevertheless fully consistent, since the particle density at the vortex center is exactly zero (see Figure 2.4 A and B). The size of these vortex cores with zero particle density is approximately given by the *healing length* ξ of the system which describes the typical distance from a local pertubation over which the wavefunction tends back towards its mean field value.

2.2.2 Two Fluid Model

Up to now we assumed that all the particles of the superfluid contribute to the condensed phase, i.e. $\rho_{\mathrm{s}} = \rho_{\mathrm{ges}}$. This is only true at zero temperature T = 0. Since any experiment can only be carried out at a finite temperature it is necessary to consider the thermal contribution of the fluid, for example using the two-fluid

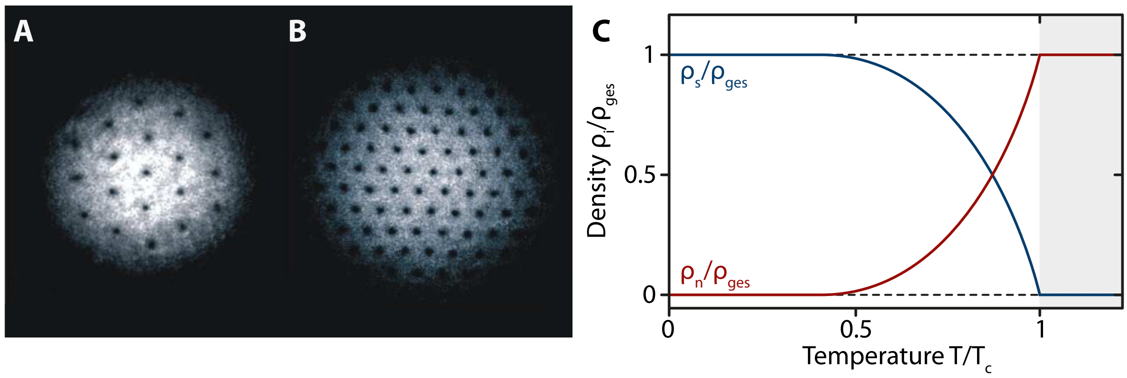

Figure 2.4: Vortex lattices in a rotating BEC at slower (**A**) and faster (**B**) rotations. Here, we emphasise the fact that vortex lattices are not turbulent (by our definition above). Taken from [Sch07]. **C:** The two fluid model describes fluids below T_{C} as a mixture of two components ρ_{s} and ρ_{n} in the condensed and normal phase respectively. Their ratio $\rho_{\mathrm{s}}/\rho_{\mathrm{n}}$ strongly depends on the temperature T of the fluid.

model, originally introduced by Tisza [Tis38]. He assumed that the system can be described by a fully condensed part ρ_{s} with no entropy and all particles occupying the same ground state and a thermal part ρ_{n} in the normal phase which carries all the entropy of the system. The ratio of superfluid to normal density $\rho_{\mathrm{s}}/\rho_{\mathrm{n}}$ with the constraint $\rho_{\mathrm{s}} + \rho_{\mathrm{n}} = \rho_{\mathrm{ges}}$ is then given by the temperature T of the fluid (see Figure 2.4 C).

The reason why we put such an emphasis on the presence of the normal component is that it interacts with the superfluid component through scattering of thermal quasiparticles with the vortex lines [Bar83]. Due to this coupling it is necessary to distinguish different regimes of quantum turbulence [Bar14]:

1) The very low temperature regime $T \ll T_{\mathrm{C}}$ where the presence of normal component is negligible since $\rho_{\mathrm{n}} \approx 0$.

2) The high temperature regime $T_{\mathrm{C}}/2 \lesssim T < T_{\mathrm{C}}$ where only the superfluid part is in a turbulent state and dissipates its energy through friction with the normal fluid.

3) The high temperature regime where both components are in a turbulent state and energy exchange is possible in both directions.

The implications of these different possible situations on the nature of turbulence and the corresponding energy spectra are discussed in the next section.

2.2.3 Phenomenology of Quantum Turbulence

As displayed in Figure 2.4 A and B, the mere presence of vortices in a superfluid can not be identified with turbulent dynamics in the system. Naturally, the question comes up whether there exists a corresponding quantity to the Reynolds number R which, as a reminder, compares the size of the largest to the smallest eddy current in the fluid. It is obvious that the classical Reynolds number itself is not defined in a superfluid since vortices are discrete. However, intuitively R quantifies the available length scale range (i.e. the number of degrees of freedom) for turbulence. As a result, one can argue that the corresponding "number" in a superfluid is proportional to the total length (number) of vortices in a three-(two-)dimensional fluid. How many vortices in different systems are required in order to observe chaotic behaviour is still an open question [Tsa15]. Analogous to the classical case we will now review the statistical results for turbulent spectra for the case of *fully developed turbulence*.

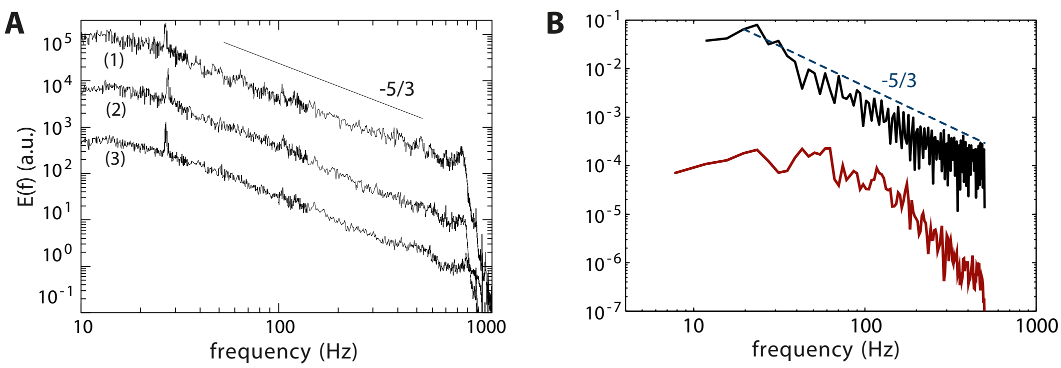

Figure 2.5: **A:** Liquid ^{4}He driven by two counter-rotating discs, above (1), at (2) and below (3) T_C. The spectra clearly follow Kolgomorovs $-5/3$ law. The experimental curves are shifted vertically to prevent overlapping. Taken from [Mau98]. **B:** Numerical simulation of the energy spectrum for a turbulent superfluid (black). Kolgomorov scaling emerges because several vortex lines form parallelly aligned bundles which mimic the classical behaviour in the coarse grained flow (compare with Figure 2.6). The red line shows the energy spectra of these bundles alone, where randomly aligned vortices were removed. Taken from [And12].

Remarkably, in many superfluid systems one observes the same Kolgomorov scaling as in classical fluids (see Figure 2.5), for example when driving them mechanically at large lengthscales. This is easily understood in the high temperature regime (3) when the classical part of the fluid is turbulent as well and dominates the energy spectrum. However, also in low temperature fluids (1) or for a non-turbulent classical part (2) the same Kolgomorov scaling can be observed. All regimes, where the Kolgomorov picture is valid, are referred to as *quasiclassical* or *Kolgomorov turbulence* [Bar14].

Quasiclassical turbulence can be understood for example by using numerical simulations (see Figure 2.6). They reveal that a seemingly random vortex tangle of the superfluid contains several bundles of parallelly aligned vortices. These bundles mimic the classical, continuous vorticity on larger scales $l \gg l_{\mathrm{vort}}$, where l_{vort} is the mean distance in between vortices. This quasiclassical regime is the paragon of the *correspondence principle* that was already mentioned above. In this sense the laws of quantum mechanics already contain the foundation for classical turbulence.

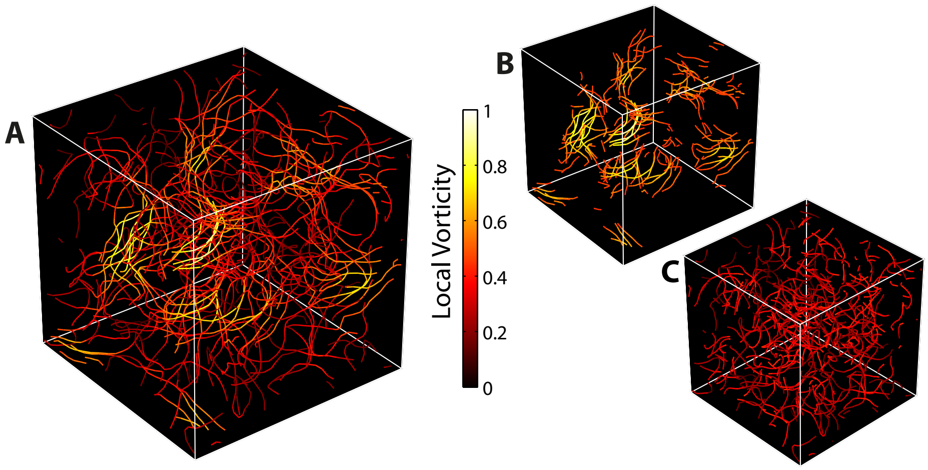

Figure 2.6: **A:** Numerical simulation of the vortex distribution for a turbulent three dimensional superfluid. The vortices are colored according to the local magnitude of the coarse grained vorticity. In **B** and **C** the distribution is split into its polarized and random part, respectivly. Taken from [And12].

As derived in the previous section on classical turbulence, the $-5/3$ scaling is connected to a direct energy cascade from large to small lengthscales until dissipation occurs at some scale η_{visc} through viscosity. Viscosity drops out as dissipative mechanism for the inviscid superfluid and therefore a different process has to occur when Kolgomorov scaling is observed. Again, at high temperatures the solution is found quickly, since the superfluid interacts with its normal component where subsequently the energy is dissipated classically. In the low temperature limit a completely different dissipative mechanism through the dynamics of vortices has been found.

So far, we have just assumed that vortices are smooth lines that move in some chaotic way (in the turbulent situation) through the three dimensional space (see Figure 2.6 A). However, vortices also contain non-trivial dynamics by themselves through so-called *Kelvin waves*. A Kelvin wave is a transverse, circularly polarized displacement of a vortex line that is restored by the tension produced by the kinetic energy along the vortex length [Pao11]. These waves are produced through vortex reconnection (see Figure 2.7 A and B) and were recently observed directly in ^{4}He experiments [Fon14]. Kelvin waves are underamped and interact non-linearly in a way that oscillations of higher and higher frequencies are produced until they become high enough to emit phonons. These phonons are absorbed by the boundary and thus provide a dissipative mechanism for Kolgomorov scaling at low temperatures [Pao11].

This *Kelvin-wave cascade* happens on length scales $l \ll l_{\text{vort}}$ and thus the energy spectrum of turbulent superfluids at low temperatures is believed to contain both the Richardson at larger, and the Kelvin-wave cascade at smaller length scales (see Figure 2.7 C). To what extend this two cascade picture actually holds in nature, is yet still a debated topic in ongoing research. For example, the possibility of a bottleneck in-between the two cascades, which would alter the spectrum is discussed in literature [Tsa15].

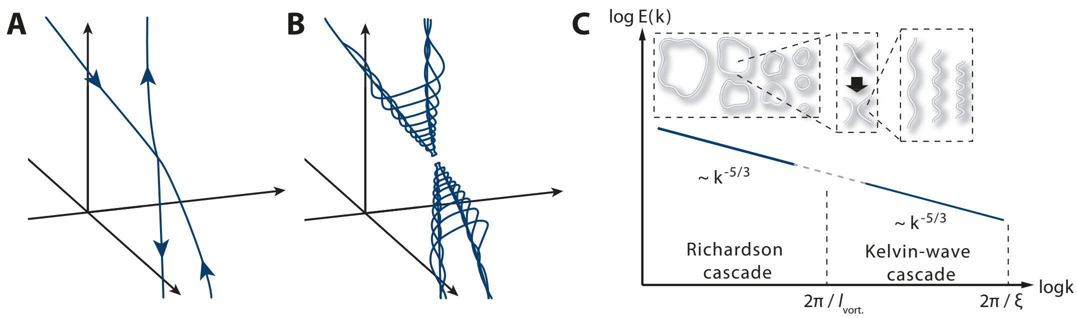

Figure 2.7: **A:** Numerical simulation of the reconnection of two vortex lines. **B:** After reconnection the vortex lines quickly retract while emitting Kelvin waves. This process was direcly observed in a recent experiment [Fon14]. Figure adapted from [Sch85]. **C:** The dissipation through kelvin waves provides the necessary dissipative mechanism for an energy cascade also at low temperatures. As a result the energy spectrum for homogeneous and isotropic quantum turbulence is believed to contain both the Richardson as well as the Kelvin-wave cascade. Taken from [Tsu13].

It is also possible to excite turbulence in superfluids such that no energy cascade appears. These turbulent states have no classical counterpart and are therefore purely quantum mechanical effects. This kind of turbulence is referred to as *ultra-quantum* or *Vinen turbulence* [Bar16]. It can be excited by driving the system at very short length scales $l_{\text{drive}} < l_{\text{vort.}}$ (for example thermally) such that the fluid is missing energy at large length scales. In this state the vortex tangle is completely random and contains no large scale eddy currents (or polarized vortex bundles). Numerical simulations confirm that the energy spectrum shows the k^{-1} fall-off expected for smooth isolated vortices [Bag12].

Up to this point we considered turbulent behaviour of the flow or vorticity of the (super-)fluid. However, there exists a form of turbulence of non-linearly interacting waves in addition. *Wave turbulence* can develop in both classical and quantum mechanical systems and since it was recently observed in a degenerate quantum gas [Nav16], we provide a quick overview over the main results at this point.

2.2.4 Wave Turbulence

Wave turbulence is very similar to hydrodynamic turbulence in the sense that it describes the chaotic dynamics of waves over many length and time scales. Even though the degrees of freedom are now given by waves rather than vortices, most results of the statistical description for hydrodynamic turbulence do still hold. Wave turbulence is likewise described best by an energy flux through scales with spectra similar to the Kolgomorov spectra. The exact form of these *Kolgomorov-Zakharov* spectra is derived using dimensional arguments once more [Naz11]

$$E^{1\text{D}} \propto \varepsilon^{1/(N-1)} k^{y}, \tag{2.14}$$

where

$$y = d - 6 + 2\alpha + \frac{5 - d - 3\alpha}{N - 1}. \tag{2.15}$$

Here α is defined by the dispersion relation of the waves $\omega \propto k^{\alpha}$, d is the dimension and N is the smallest number of waves that interact non-linearly. For example, for phonon turbulence ($\alpha = 1$) in a three dimensional BEC ($d = 3$) and with three-wave scattering ($N = 3$) we obtain $E^{1\text{D}} \propto k^{-3/2}$.

There is an important difference between hydrodynamic and wave turbulence in the case of *weak non-linearity*, which is often assumed. Using the latter assumption together with the dispersion relation $\omega(k)$ it is possible to obtain the energy spectra from exact analytical solutions. Furthermore, wave turbulence for even-N systems shows a dual cascade behaviour with the direct energy cascade exponent as in the equation above and an inverse *waveaction cascade* with a different exponent [Naz11].

Wave turbulence is especially important if one generalises the discussion of incompressible fluids above to compressible fluids. The most straightforward approach is to separate the flow into an incompressible $\boldsymbol{v}^{\mathrm{i}}$ and a compressible $\boldsymbol{v}^{\mathrm{c}}$ contribution. Accordingly, in the incompressible energy density spectrum $E^{\mathrm{i}}(k)$ all the different hydrodynamic turbulence cascades discussed above can show up, while in the compressible energy density spectrum $E^{\mathrm{c}}(k)$ wave turbulent cascades can emerge, for example generated from sound waves (phonons) [Tsu08].

2.2.5 Length scales

To recap the foregoing results for the different classes of turbulence, it is useful to compare some of the length scales involved in the different systems. We saw that in the classical case the turbulent energy cascade is connected to a large separation of the driven l_{drive} from the dissipate length scale η_{visc}. The sizes of eddy currents span many orders of magnitude within a single fluid (from 3/4 up to 12, see Figure 2.1).

In quantum mechanical turbulence all vorticity becomes discrete and not the size but rather the amount of vortices becomes the important scale. From the total vortex length per unit Volume L one obtains the mean inter-vortex distance as $l_{vort.} = L^{-1/2}$. The latter length scale separates the regime where quasiclassical cascades are observable in some coarse grained flow ($l > l_{\mathrm{vort.}}$) from the ultraquantum regime $l < l_{\mathrm{vort.}}$ without classical analogue. Which of the latter cases arises strongly depends on the scale l_{drive} at which energy is fed to the system.

The spatial extend of the vortices is of the order of the healing length ξ given by:

$$\xi^{\mathrm{3D}} = \frac{\hbar}{\sqrt{2mg_{\mathrm{3D}}\rho_{\mathrm{3D}}}}, \tag{2.16}$$

or, in two dimensions:

$$\xi_{2\mathrm{D}} = \frac{\hbar}{\sqrt{m g_{2\mathrm{D}} \rho_{2\mathrm{D}}}}, \tag{2.17}$$

with coupling strength g, the particle mass m and density ρ. The available range Δl for an energy cascade is thus $\xi < l < D$, where D is the total size of the system. In typical helium experiments one gets $\xi \approx 10^{-8}\,\mathrm{m}$ and $D \approx 10^{-1}\,\mathrm{m}$, implying $\Delta l = 10^7$ [Tsa15]. The situation in cold bosonic atom experiments is quite different, as $\xi \approx 10^{-6}$ while $D \approx 10^{-4}$ (i.e. $\Delta l \approx 10^2$). This small range for possible cascade phenomena is currently one of the largest limitations for research in the field of quantum turbulence with cold atom setups [Tsa15].

2.3 Turbulence in Two Dimensions

Initially, turbulence in two dimensions was introduced as a toy model for three dimensional turbulence with simpler dynamics (by just restricting the flow $\boldsymbol{v}$ to x- and y- direction). Yet, it turned out that two dimensional turbulence approximates many systems in nature very well. Examples include planetary or geophysical flow (see Figure 2.8) [Fri95]. Along with the advances in the field of cold atoms experiments, physics in reduced dimensions has attracted completely new attention, because in these laboratory experiments it is possible to create systems where all dynamics are completely constrained to one or two dimensions (see chapter 2).

We will begin this section by again taking a look at the implications of reducing the dimensions for classical turbulence first [Kra80; Naz11]. Afterwards, we will review how these differences translate to the quantum world [Tsa15].

2.3.1 Inverse Energy Cascade

As already remarked in Section 2.1, Kolgomorovs cascade picture has to be modified as soon as energy is not the sole conserved quantity of motion in the system any more. This occurs in two dimensions where the *enstrophy* defined as:

$$\mathcal{E} = \int_{\mathbb{R}^2} (\nabla \times \boldsymbol{v})^2 \, d\boldsymbol{r} = \int_{\mathbb{R}^2} \boldsymbol{\omega}^2 \, d\boldsymbol{r}, \tag{2.18}$$

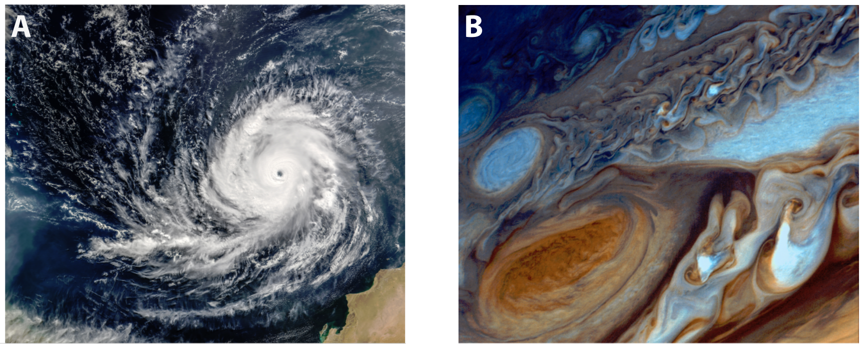

Figure 2.8: Many turbulent systems in nature behave two dimensional. The prominent cases are weather phenomena in the atmosphere, for example cyclones here on earth (**A**) or the *Great Red Spot* of Jupiter (**B**). Source: NASA.

is conserved in an incompressible, inviscid flow [Kra80]. Here, we inserted the definition of the vorticity $\boldsymbol{\omega} := \nabla \times \boldsymbol{v}$.

The fact that the system has a second conserved quantity of motion leads to the observation that steady turbulence requires now an equal rate of enstrophy injection and dissipation (in line with injection and dissipation of energy for 3D turbulence). Thus a second cascade of enstrophy from the driven l_{drive} to the dissipative lengthscale l_{dis} emerges. The respective directions of energy and enstrophy cascade in momentum space can be derived by some simple ad absurdum arguments following Nazarenko [Naz11].

From Fourier transforming equation (2.18) and by comparing to equation (2.3) we obtain:

$$\mathcal{E} = \int_0^\infty k^2 E^{1\text{D}}(k)\, dk. \tag{2.19}$$

Therefore, the energy injection (dissipation) rate ε is related to the enstrophy injection (dissipation) rate κ through:

$$\kappa \propto \varepsilon k_{\text{drive}}^2. \tag{2.20}$$

A direct energy cascade implies that energy is dissipated at larger wavenumbers $k_{\text{dis}} > k_{\text{drive}}$ with the injection rate ε. The rate of enstrophy dissipation is then given by $\kappa_{\text{dis}} \sim \varepsilon k_{\text{dis}}^2 \gg \varepsilon k_{\text{drive}}^2 \sim \kappa_{\text{drive}}$. The latter is a direct contradiction to the assumption of steadiness and as a result the only possible solution for steady turbulence requires $k_{\text{dis}} < k_{\text{drive}}$ for the energy flow in two dimensions. This flow of energy to larger length scales is named *inverse energy cascade* and in the picture of Richardson it describes the merging of vortices to larger and larger structures. This behaviour is clearly observed for the examples shown in Figure 2.8.

Repeating the argumentation above for the flow of enstrophy reveals that a steady solution can only exist for $k_{\text{dis}} > k_{\text{drive}}$, or in words a *direct enstrophie cascade*. The energy spectra are obtained from a dimensional analysis, as before [Naz11]:

$$\begin{aligned} E_{\varepsilon}^{1\text{D}} &= C_{\varepsilon} \cdot \varepsilon^{2/3} k^{-5/3} \\ E_{\kappa}^{1\text{D}} &= C_{\kappa} \cdot \kappa^{2/3} k^{-3} \end{aligned} \tag{2.21}$$

To summarize, we see that the inverse energy cascade has the same Kolgomorov spectrum as derived before while the direct enstrophy cascade has a different spectrum (the *Kraichnan spectrum*, see Figure 2.9).

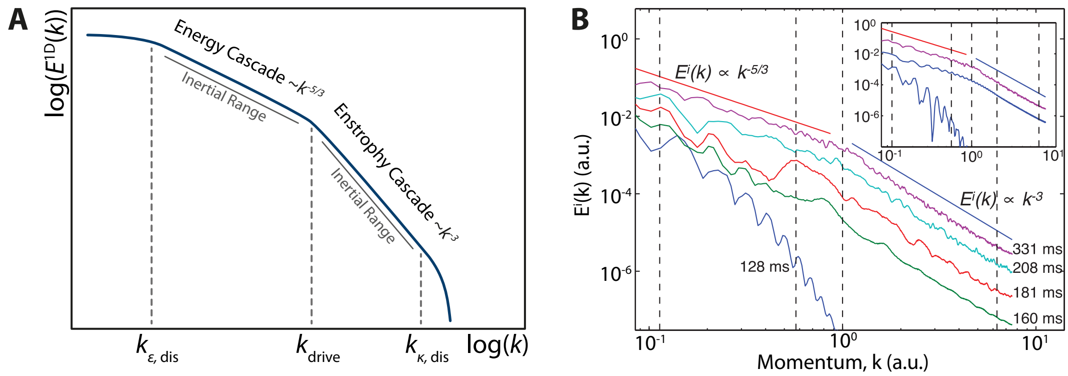

Figure 2.9: **A:** Expected dual cascade energy spectrum for steady turbulence in two dimensions. The inverse energy cascade is accompanied by a direct enstrophy cascade. **B:** Simulations of driven and decaying turbulence in a BEC. With increasing drive time a clear dual cascade behaviour of the energy spectrum develops. Inset: After stopping the drive the turbulent state decays to equilibrium again (top to bottom show the spectra after increasing times of decay). Taken from [Nee13].

2.3.2 2D Quantum Turbulence

The reduction to two dimensions has substantial effects on turbulent dynamics in superfluid systems as well. The first observation is that vortices have the geometry of points instead of lines. These vortex points are characterised by their quantised circulation alone without any additional distinguishing features (in contrast to the infinite possibilities of aligning a vortex line in 3D-space). This purely two dimensional effect has immediate consequences on the existing vortex dynamics and interactions. What is most important is that Kelvin waves are completely absent as degrees of freedom for these zero dimensional vortices. As a result, also the dissipative mechanism through emittance of phonons at very high momenta is lost. However, a new decay process becomes available since pair annihilation of reversely rotating vortices is now possible [Tsa15].

Nevertheless, many of the concepts derived from the three dimensional model can be transferred to the two dimensional world directly, among others the two-fluid model and the respective high and low temperature regimes of turbulence. The concepts of ultraquantum and quasiclassical turbulence are also still applicable. One difference is that the quasiclassical large scale flow patterns are now created by clusters of vortices with the same sign instead of polarized bundles of vortex lines.

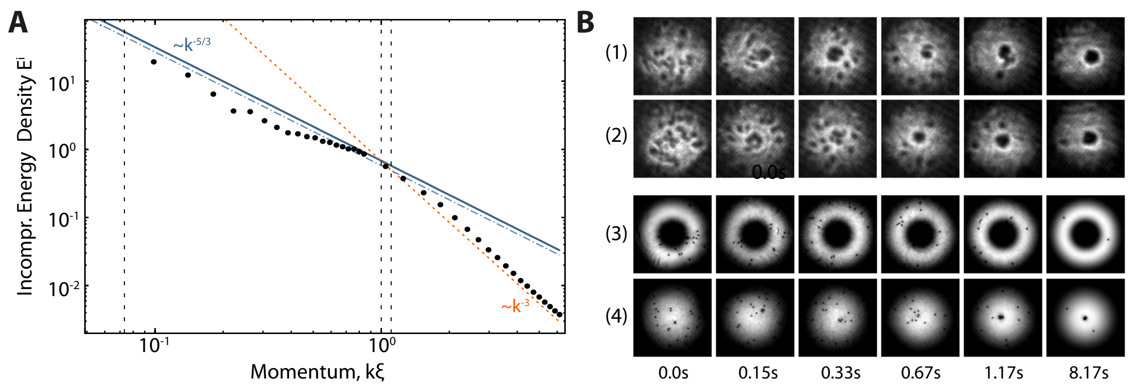

Figure 2.10: **A:** Numerical simulation of a Gross-Pitaevskii model for a two dimensional forced BEC, damped by a stationary cloud. The spectrum shows clear evidence for an inverse energy cascade. Taken from [Ree13].
B: Experimental (1-2) and numerical (3-4) investigation of turbulence in an annularly trapped two dimensional compressible superfluid by Neely et al. [Nee13]. Both the experimental (time of flight) and the numerical (insitu) data reveal a clustering behaviour of vortices which is interpreted as evidence for inverse energy transport.

Both experimental and numerical investigations of quantum turbulence in two dimensions show clear indications for the presence of an inverse energy flow (see Figure 2.10). Compared to classical turbulence we see that in the superfluid enstrophy is not well defined ($\boldsymbol{\omega} \equiv 0$) and the origin of the k^{-3} dependence at large momenta in Figure 2.10 A is not a direct enstrophy cascade. Instead, as Bradley and Anderson [Bra12] show, the k^{-3} dependence is just given by the vortex core structure in two dimensions (analogue to the k^{-1} dependence for vortex lines in three dimensional ultraquantum turbulence). Nevertheless, Reeves et al. [Ree17] were very recently able to find the quantum mechanical analogue to the classical enstrophie cascade using numerical simulations. They show that for special initial conditions of the vortex distribution a k^{-3} spectrum emerges (not linked to the vortex core structure in this case).

Most of the knowledge about quantum turbulence, that was presented to this point, was acquired through numerical simulations and experiments in superfluid ^{3}He and ^{4}He. Only very recently cold atom experimentalists started accessing this field. In the next section, we will present and discuss some of the current research and explore open questions and see how they can be answered, especially by cold atoms experiments.

2.4 Turbulence in Quantum Gases

The progress in experimentally creating and manipulating ultracold Bose and Fermi gases has opened up a completely new playground for the study of quantum turbulence. In contrast to experiments with helium, cold atoms offer a large amount of control over most of the system parameters, such as interactions, external potentials or dimensions (see chapter 3). Additionally, there exist very reliable approaches, such as solving the Gross-Pitaevskii equation, for modelling these dilute gases theoretically. The different length scales compared to Helium (see section 2.2.5) make a direct observation of vortices, the elementary building blocks of turbulence, possible. As mentioned before, the biggest limitation of cold gases is the small range that is available for energy cascades. Numerical and experimental results show that energy cascades (direct or inverse) are nevertheless observable [All14; Nav16].

In this section, we explore the experimental progress with cold atoms to date. First, some of the different methods of turbulence creation in these systems are discussed. Next, we recall some of the available detection methods and finally, we look at the decay of turbulence after the drive has stopped.

2.4.1 Creating Turbulence

Several different schemes of taking a condensate out of equilibrium into a turbulent state have been proposed or already implemented in experiments (see Figure 2.11). Ideally, one would like to force the system at a controlled wavenumber k_{drive} with a known energy injection rate ε. As discussed above, the exact driving scheme determines which forms of turbulence will or can be observed. As a reminder, rotating the condensate around one axis produces a stable lattice of parallely aligned vortices lines which, by definition, is not turbulent (see Figure 2.4). All of the excitation methods rely on the creation of time varying potentials for the atoms. In most cases these potentials are realised using optical dipole traps which are discussed in more detail in chapter 3.

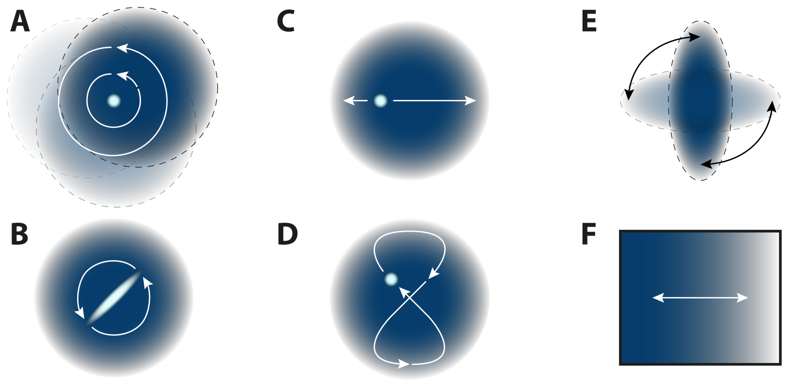

Figure 2.11: Different schemes of creating turbulent clouds of cold atoms.
A: Rotating in the complete cloud along two different axes or along one axis with a barrier in the center. The latter was used in [Nee13]. **B:** Stiring the cloud with a paddle pontential. Numerical study in [Whi12]. **C:** Sweeping a circular potential barrier through the cloud. Applied in [Kwo14]. **D:** Moving a barrier through the cloud on a figure eight path. Numerical study in [All14]. **E:** Periodic deformation of the cloud by trap deformations. Applied in [Hen09]. **F:** Excitation of a dipole mode in a box potential. Used in [Nav16].

The different excitation methods can be grouped in two categories, namely procedures that add angular momentum to the cloud (Figure 2.11 A and B) and others that do not (C-F). This differentiation becomes especially important in two-dimensional systems, where vortices can annihilate each other. If no angular momentum is added to the system, the created number of positive and negative signed vortices is exactly equal.

A different distinction can be made through the length scale on which energy is added to the system. From the discussion in the previous chapter it becomes clear that exciting the system on larger length scales makes the development of a quasiclassical energy cascade in the spectrum more likely (Figure 2.11 A,B,E,F). Using procedures that add energy on small length scales (C and D) the fluid is more likely to enter the regime of ultraquantum turbulence.

Independent of the driving process, the number (or length) of vortices grows with excitation time t_{drive} and the speed of the obstacle ω_{drive} (especially in the low temperature superfluid). The vortex generation rate however, depends on the exact scheme that is applied. As Allen et al. [All14] show, even the contour on which a small obstacle is sweeped through the cloud has a large influence. In their numerical study they observed that a figure eight path (D) generates vortices with a much larger rate compared to when one stirs along a circle.

Finally, some of the driving processes are more likely to introduce also other kinds of turbulence, i.e. non-hydrodynamic turbulence, to the system. Navon et al. [Nav16] excite a dipole mode of the cloud in a box potential (F) and they observe effects that they attribute to the presence of wave turbulence. This can be understood easily, since the hard reflection of the box walls is likely to generate phonons in the compressible part of their fluid.

At this point, we left out some important vortex generation processes like the *Kibble-Zurek mechanism*. The latter describes the formation of topological defects (i.e. vortices) when the system is quenched through the phase transition. Even though these mechanisms introduce vortices to the system, they are less effective than the procedures above [All14] and so far, no turbulence creation using these additional methods has been reported.

2.4.2 Detecting Turbulence

To date, every experiment that reported observations of turbulence in atomic clouds relied on *time of flight* (TOF) measurements. The idea is that at a certain point in the experimental sequence, the confining potential is suddenly switched off and the atoms start to expand freely. After some time t_{TOF}, the resulting atom distribution is then imaged (in general using *absorption imaging*). In our experiment, we employ a sightly modified TOF scheme that we refer to as *T/4-imaging*. A detailed explanation of the experimental implementation of TOF and T/4-imaging will be given in chapter 3, here we will only focus on those observables that can be obtained from these imaging procedures.

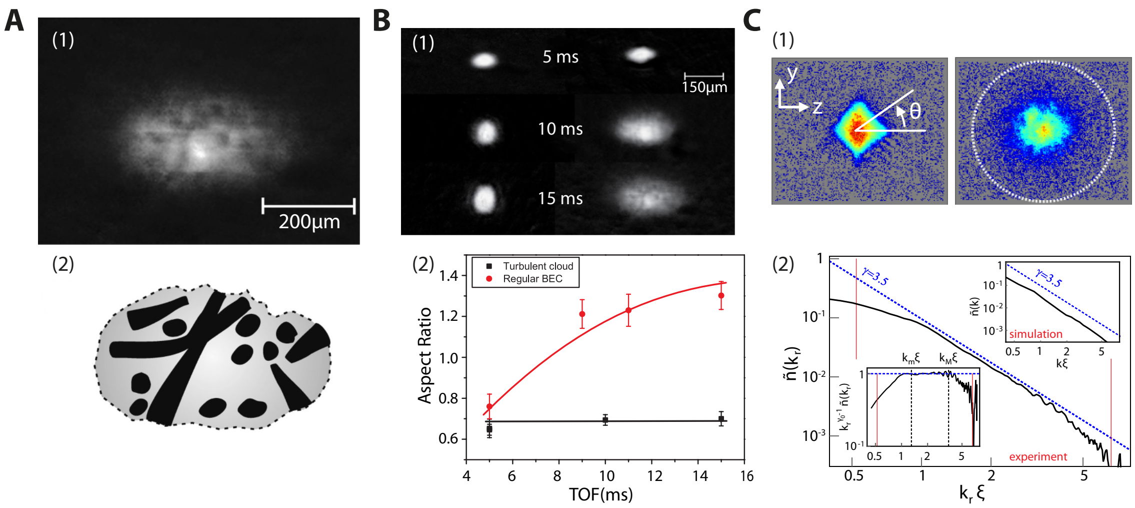

Figure 2.12: Different schemes of detecting turbulence in clouds of cold atoms. **A:** In cold atom systems chaotic vortex tangles can be detected directly by imaging after a short time of flight expansion (1). (2) is a schematic diagram showing the extracted vortex tangle from image (1). Taken from [Hen09]. **B:** A free expansion of a condensate in equilibrium involves an aspect ratio inversion of the cloud (1, left; 2, red curve). Henn et al. observed that when starting from a turbulent state, the aspect ratio stays constant (1, right; 2, black curve). Taken from [Hen09]. **C:** (1) shows the TOF images when starting from a condensate in a three dimensional box trap in equilibrium (left) or a turbulent state (right). Turbulence can be detected through the emergence of a direct energy cascade, visible for example in the momentum distribution of the gas (2). Taken from [Nav16].

Depending on the expansion time t_{TOF}, different observables for turbulence can be extracted out of the TOF images. For a short expansion time it is possible to observe vortices in the cloud density profile directly. This is possible since the healing length ξ (i.e. the vortex core size) is a few orders of magnitude larger in cold atom clouds than in helium. The spatial momentum distribution close to the vortex core (close particles have higher momenta) leads to a quick magnification of the core during time of flight until it gets large enough to be resolved optically (see Figure 2.12 A). A chaotic alignment of vortices as observed by [Hen09] is a direct evidence for turbulence.

A second indication for turbulence can be found when the cloud is observed over a range of expansion times. It is well known that a condensate in equilibrium inverts its aspect ratio during TOF. The reason for this is simply that for short flight times one observes the spatial distributions of the condensed cloud in the trap while for long times one observes its momentum distribution and these two quantities are Fourier transforms of each other. Interestingly enough, this inversion is not observed any more if the condensate is turbulent, the cloud retains its initial aspect ratio instead (see Figure 2.12 B). This expansion of the cloud can be explained by considering its coherence length that is reduced due to phase defects [Tsa15]. An important observation is that a thermal cloud will converge towards an aspect ratio of one during TOF since its momentum is distributed isotropic, thus this case is different again.

Finally, as already noted, for very long expansion times the initial density distribution in the trap is negligible and one obtains the momentum distribution of the fluid. From the one dimensional momentum distribution $n^{1\mathrm{D}}(k)$ defined analogously to the one dimensional energy distribution $E^{1\mathrm{D}}(k)$ (see equation 2.4) one can immediately extract the latter as

$$E^{1\mathrm{D}}(k) \propto n^{1\mathrm{D}}(k)k^2. \tag{2.22}$$

In this way Navon et al. [Nav16] were able to detect a direct energy cascade caused by wave turbulence in their BEC via the momentum distribution (see Figure 2.12 C). To strengthen their confidence, they performed a numerical analysis of their experimental setup as well, which reproduced their measurement results with an impressive accuracy.

The large drawback of TOF imaging is that it is by definition destructive. Thus for each experimental configuration of vortex tangles only a single image is obtained. In this way it is only possible to extract statistical information about the system (such as mean vortex number or length over time). In order to observe the dynamic processes connected to turbulence such as vortex reconnection or annihilation continuous non-destructive imaging is necessary. One method that could possibly allow such measurements in the future is *phase contrast imaging* [Hen09].

2.4.3 Decay of Turbulence

The observation of decaying turbulence, i.e. after the energy injection has been stopped, is another important tool for the study of turbulent dynamics. For example, in three dimensional systems one expects that the total vortex length L decays as $L \propto t^{-3/2}$ when starting from quasiclassical turbulence and as $L \propto t^{-1}$ in the ultraquantum regime. Hence, the decay properties can provide important indications about the initial state of the system before the driving has been stopped [All14].

In reference [Kwo14] Kwon et al. study turbulence in an oblate shaped condensate in order to gain insight in the vortex annihilation dynamics in this system. They identify two main causes for the decay in the form of a single body (vortices that leave the condensate) and a two body (vortex annihilation) process.

2.5 Open Questions

Even though experiments with superfluid helium since the 1950th have already brought significant progress to the field of quantum turbulence, many unsolved questions remain. After the first observation of quantum turbulence in a BEC by Henn et al. [Hen09] the field has attracted more and more attention recently. This is due to the fact that in the well controlled environment of cold atom systems some of the long-time unsolved problems might become addressable soon. Here, we will give a short overview over the most important open questions in the field in general and with respect to fermionic systems in particular.

The first open question addresses the very core of turbulence, namely the definition itself. As mentioned in section 2.1, there exists no unanimous definition of turbulence at the moment. In contrast to classical systems, where the identification of an unambiguous signal for turbulence is difficult, in quantum mechanics vortices are recognized as the sole root for hydrodynamic turbulence. At the moment, the question if some given arrangement of vortices will become turbulent or not is still unsolved in general. By addressing this issue, the discovery of an order parameter which precisely defines the transition from stable to chaotic dynamics could be possible [Tsu13].

Furthermore, as seen in the previous section, the technique of optical dipole traps leads to countless possibilities of driving turbulence in cold gases. Superfluid Helium can be driven either on rather large scales using mechanical obstacles or on very small scales through thermal excitation. In cold atoms, by using more elaborate laser setups (see chapter 5), it is, in principle, possible to continuously scan a complete range of driving length scales within a single experimental machine. This additional freedom could, for example, lead to a better understanding of the crossover from the Kolgomorov cascade to the ultraquantum regime.

Most cold atom experiments additionally offer the ability to tune the coupling strength g via so-called *Feshbach resonances*. The interaction strength g is especially important since it directly modifies the healing length ξ (see equation 2.16). In this way and by changing the system size L one can directly modify the available length scale range $\log(L/\xi)$ in cold atom systems [Tsa15]. Hence, the influence of this length scale range on the turbulent behaviour is one more open question to be tackled by cold atoms experiments.

A very general issue is the theoretical description of turbulence. Currently, the Gross-Pitaevskii equation is applied successfully in many cases. However, as Tsatsos et al. [Tsa15] point out, this approach must fail for very highly excited and correlated systems since the system can not be described by a single coherent wavefunction any more. Cold atom systems with the addition of non-destructive insitu imaging methods could provide the necessary insight in order to model these systems theoretically. A second application of insitu imaging could be to directly observe the formation of a quasiclassical Richardson cascade on the level of single vortices [Tsu13].

Finally, there are also many open questions concerning more complicated systems like bosonic mixtures or spin turbulence that could be addressed experimentally with cold quantum gases [Tsa15]. These are of lesser interest in the context of this thesis and therefore we will now focus on the special case of fermionic gases instead.

2.5.1 Fermionic Systems

When we mentioned turbulence in fermionic quantum gases up to this point, we always implied that the gas consists of at least two spin components. Due to the *Pauli exclusion principle*, a single spin component Fermi gas is non-interacting at low temperature and no superfluid transition is possible. The foundation for turbulence in two component Fermi systems was laid by Zwierlein et al. [Zwi05] in 2005 by directly observing vortices in a rotating gas at low temperatures across all interaction strengths. This observation is interpreted as direct evidence for the superfluid character of the system and provides the prerequisites for quantum turbulence.

The correct microscopic description of this superfluid depends on the inter-particle interactions. For weakly repulsive interactions tightly bound bosonic molecules form, which subsequently condense into a BEC at low temperatures. The regime of weakly attractive interactions is covered by the theory of Bardeen, Cooper and Schriefer (BCS). Here, the particles form *Cooper pairs* in momentum space. These Cooper pairs are rather weakly bound compared to the molecules in the BEC regime and they are not localized in space. In cold quantum gases it is possible to continuously tune the interactions from the BEC to the BCS regime by the means of Feshbach resonances. This is known as the *BEC-BCS crossover*. Readers unfamiliar with this crossover are asked to proceed to the next chapter where it is presented in more detail.

The first question that comes up with regard to fermionic quantum turbulence is directly connected to the BEC-BCS crossover. In the BEC regime of tightly bound molecules the expectation is that the system closely resembles bosonic gases. In the BCS limit it is less clear if the superfluid state can survive during the emergence of turbulence or if it is destroyed by phase defects [Tsa15]. Assuming that quantum turbulence is observable in the entire crossover, the next question is if the BEC regime differs from the BCS side or if both show the same behaviour.

Additionally, the regime of strongest interactions, namely the *unitary Fermi gas* is of great interest in the context of turbulence. This is because the strong interactions lead to the highest vortex density of any known superfluid, being on the order of the interparticle spacing [Wla15]. Besides the unitary Fermi gas is directly applicable to describe neutron stars. In these stars, there exists a pinning mechanism of quantized vortices to nuclei in the neutron star's crust which is still lacking a complete description. Cold atom experiments could provide new insight into this process of vortex pinning [Bul16].

The unitary Fermi gas could also serve as a testbed for theoretical models. Since its vortex density is extremely high, it is already possible to excite turbulent states in very small systems that are still accessible by numerical simulations. Very small systems are also interesting from the viewpoint of quasiclassical and ultraquantum turbulence. A new regime of turbulence could be found, where (quasi-)classical turbulence is suppressed since no large scale flows can form, but where ultraquantum turbulence still persists [Bul16].

Finally, two component fermi systems offer an enormous range of exotic phases that could be studied from the viewpoint of turbulence. We recently observed that pairing correlations persist in the normal phase of our two component fermi gas and that in some regions of the phase diagram the pairing energy is strongly increased by non-trivial (i.e. beyond mean field) many body effects [Mur17]. In spin polarized systems Larkin-Ovchinnikov (LO) and Fulde-Ferrell (FF) phases, connected to a pairing gap oscillating in space, were predicted. Studying the effects of these and other phases on turbulent states opens up an entire new field of research for the future of quantum turbulence [Bul16].

2.6 Collective Modes

In the last section of this chapter a short overview of collective excitations in the harmonic trap of our system is given. The reason is that in our current experimental setup these modes are the only means available to us when attempting to excite turbulent motion. A detailed theoretical discussion of these modes together with experimental data for two dimensional Fermi gases can for example be found in the following references [Vog12; Bau13; Vog13].

2.6.1 Dipole Mode

The dipole mode can be excited by first displacing the atom cloud with respect to the harmonic trap minimum and then releasing it. This leads to a classical harmonic oscillation in the trap without any cloud deformations (see Figure 2.13 A). Since the oscillation is completely independent of the equation of state (EOS) of the cloud, this dipole mode provides a reliable method to calibrate the trap frequencies $\omega_{x,y,z}$ in all directions. In our cylindrically symmetric trap we define the radial trap frequency as $\omega_r = 1/2(\omega_x + \omega_y) \approx \omega_x$.

The dipole mode is completely unsuitable for the excitation of turbulent motion as it does not even excite any dynamics within the cloud itself.

2.6.2 Breathing Mode

The breathing mode corresponds to the oscillation of the cloud radius r (see Figure 2.13 B) and thus involves an alternating compression and expansion of the atom

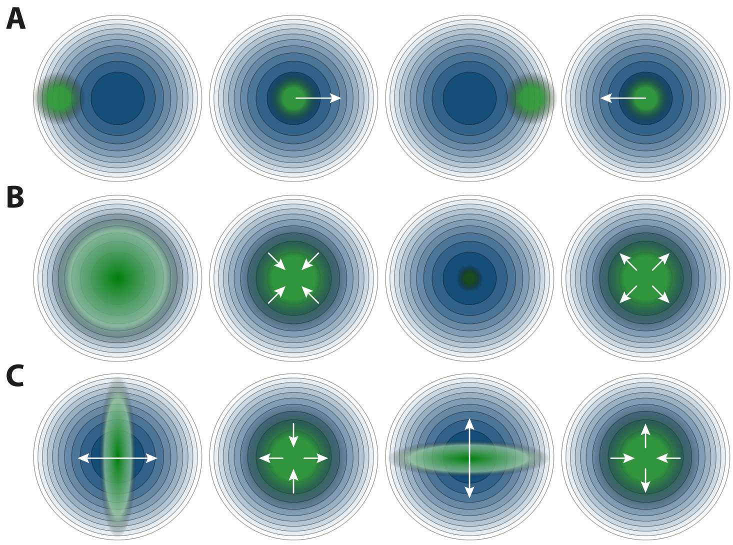

Figure 2.13: Variety of collective modes that can be excited in a harmonic trap. The resonant frequencies ω of the different modes are in general not equal. The white arrows indicate the velocity field of the cloud. The dipole mode is just a collective oscillation of the whole cloud in the harmonic trap (**A**), the breathing mode is an oscillation of the atom cloud radius r (**B**) and the quadrupole mode is a transverse oscillation of a cloud deformation without volume change (**C**).

cloud. As a result it depends on the compressibility and is thereby sensitive to the equation of state $\rho(\mu, T, p)$ of the gas. The breathing mode is (up to technical background heating) completely undamped since no shear forces arise during its motion and the bulk viscosity ζ of our gas is zero [Vog12].

In order to obtain the frequencies ω_B of the breathing mode we distinguish between two limits. In the *collisionless regime*, where the collision rate is smaller than the trap frequency, the atoms oscillate independently and one simply obtains

$$\text{Collisionless Limit:} \qquad \omega_\mathrm{B} = 2\omega_r. \tag{2.23}$$

Following Vogt [Vog13], in the opposite *hydrodynamic limit*, where the collision rate is much larger than the trap frequency one obtains

$$\text{Hydrodynamic Limit:} \qquad \omega_\mathrm{B} = \sqrt{2\gamma + 2}\omega_r. \tag{2.24}$$

Here, γ is defined by the relation between the pressure p to the density (or EOS) ρ

$$p \propto \rho^{\gamma+1}. \tag{2.25}$$

From the fact that the breathing mode is completely undamped it inevitably follows that it can not introduce any kind of turbulence into the system. The energy that is injected into the breathing mode just remains at this large length scale in the system.

2.6.3 Quadrupole Mode

The quadrupole mode is an oscillation of the cloud widths in x- and y-direction with a respective phase shift of π to each other (see Figure 2.13 C). The volume of the cloud remains constant during this oscillation and therefore it does not depend on the EOS. However, in contrast to the breathing mode the quadrupole mode obviously contains shear movement and thus probes the shear viscosity η of the gas.

The frequency ω_{Q} of the mode can be derived for the two interaction limits as

$$\begin{aligned} \text{Collisionless Limit:} \qquad & \omega_{\mathrm{Q}} = 2\omega_r, \\ \text{Hydrodynamic Limit:} \qquad & \omega_{\mathrm{Q}} = \sqrt{2}\omega_r. \end{aligned} \tag{2.26}$$

Since the quadrupole mode depends on the shear viscosity, which is only zero at zero temperature, the oscillation is damped in this case. A universal relation between damping rate Γ_{Q} and frequency ω_{Q} is given by [Bau13]

$$\Gamma_{\mathrm{Q}} = \sqrt{\sqrt{8(\omega_{\mathrm{Q}}\omega_r)^2 - 7\omega_r^4} - \omega_r^2 - \omega_{\mathrm{Q}}^2}. \tag{2.27}$$

From the collective modes discussed, the quadrupole mode is the only one that could possibly drive turbulent motion in the gas. It dissipates its energy on large length scales (collective motion in the trap) through a mechanism existing on small length scales (viscosity) and is a promising candidate for the observation of a direct cascade.

2.6.4 Theoretical Formalism

Both the breathing or monopole and the quadrupole mode can be derived from kinetic theory in a (semi-)classical picture. To this end one has to solve the equation of motion for the phase space distribution $f(\boldsymbol{r}, \boldsymbol{p}, t)$ of the particles, which is given by the Boltzmann equation

$$\left[\frac{\partial}{\partial t} + \frac{\boldsymbol{p}}{m}\nabla_{\boldsymbol{r}} + \left(\nabla_{\boldsymbol{r}} V(\boldsymbol{r})\right)\nabla_{\boldsymbol{p}}\right] f(\boldsymbol{r}, \boldsymbol{p}, t) = -I[f]. \tag{2.28}$$

Here, $V(\boldsymbol{r})$ is the harmonic potential and $I[f]$ is the collision integral for the scattering process of two Fermions with different spin. The collective mode solutions are found by linearising this equation for small deviations from equilibrium

$$\delta f(\boldsymbol{r}, \boldsymbol{p}, t) = f_{\text{eq}}(1 - f_{\text{eq}})\Phi(\boldsymbol{r}, \boldsymbol{p}, t), \tag{2.29}$$

where the additional $f(1-f)$ factor is introduced for convenience [Bau13]. Following Vogt [Vog13] the function $\Phi(\boldsymbol{r}, \boldsymbol{p}, t)$ can be approximated by expanding it into a suitable set of bases ϕ_i that are also referred to as *moments*

$$\Phi(\boldsymbol{r}, \boldsymbol{p}, t) = \sum_0^n c_i(t)\phi_i(\boldsymbol{r}, \boldsymbol{p}). \tag{2.30}$$

One finds that the basis set

$$\phi_1 = \omega_{\text{R}}(x^2 + y^2), \quad \phi_2 = \omega_{\text{R}}(xp_x + yp_y), \quad \phi_3 = \omega_{\text{R}}(p_x^2 + p_y^2), \tag{2.31}$$

leads to a solution $\Phi_{\text{B}}(\boldsymbol{r}, \boldsymbol{p}, t) = e^{-i\omega_{\text{B}}t}\Phi_{\text{B}}(\boldsymbol{r}, \boldsymbol{p})$ under the following mode frequency equation

$$\omega_{\text{B}} - 4\omega_T^2 = 0. \tag{2.32}$$

The collision integral $I[f]$ is zero for all the moments of this solution and therefore we recover the solution of the undamped breathing mode with $\omega_{\text{B}} = 2\omega_{\text{R}}$.

The solution for the quadrupole mode is found by using the following basis set instead

$$\phi_4 = \omega_{\text{R}}(x^2 - y^2), \quad \phi_5 = \omega_{\text{R}}(xp_x - yp_y), \quad \phi_6 = \omega_{\text{R}}(p_x^2 - p_y^2), \tag{2.33}$$

where the last moment does lead to a non zero contribution from the collision integral $I[\phi_6]$ in this case. As a result, the mode frequency equation for the quadrupole solution $\Phi_{\mathrm{Q}}(\boldsymbol{r}, \boldsymbol{p}, t)$ does depend on the collision time τ as

$$(\omega_{\mathrm{Q}}^2 - 4\omega_{\mathrm{R}}^2) + \frac{i}{\tau\omega_{\mathrm{Q}}}(\omega_{\mathrm{Q}}^2 - 2\omega_{\mathrm{R}}^2) = 0 \tag{2.34}$$

In the collisionless ($\tau\omega \gg 1$) and hydrodynamic ($\tau\omega \ll 1$) regime we recover the limiting frequencies as given above.

3 Experimental Background

In this chapter we will recall some of the most important theoretical concepts that are necessary for the experimental work with ultracold fermions. Additionally, some of the techniques to create and probe the two dimensional Fermi gas in our experiment are presented. We will focus only on those aspects that are important in the context of turbulence and collective modes. A complete description of the experimental apparatus is found in [Wen13], the theoretical concepts are reviewed in [Gio07].

3.1 Theoretical Framework

The reason for the continued attention experiments with cold atoms have received for many years now, lies to a large extend in their simple theoretical description. Compared to condensed matter experiments, where some Hamiltonian H describes a substantially reduced system compared to the experiment, cold atoms can simulate the dynamics of simple Hamiltonians very accurately. The root for the validity of simple models lies in the low temperature limit where many physical details, like the inner atom structure, are completely negligible. As a result, ultracold quantum gases are perfectly suited to test our understanding of nature on a very fundamental level.

The theoretical description of cold atom systems is mainly governed by three important attributes of the particles: their quantum statistical behaviour, inter-particle interactions and coupling to external potentials. Consequently, we begin this section by reviewing the most important facts for each of these aspects. Afterwards, we focus on many-body systems of Fermions in two dimensions and discuss their low temperature phase diagram. Some details on the creation of external potentials are found in the following section about the experimental preparation.

3.1.1 Temperature Scales

At high temperatures both bosonic and fermionic gases behave alike and satisfy classical Maxwell-Boltzmann statistics (see Figure 3.1 A). Only after the particles are cooled down and their de Broglie wavelength increases (B), their quantum mechanical nature becomes important. Bosonic atoms, where the many-particle wavefuntion is totally symmetric with respect to particle exchange, can all occupy the same state. Their ground state in a harmonic potential is given when all particles are in the lowest energy state (C). The wavefunction of a fermionic many-body system is totally antisymmetric, which implies that two fermions can never occupy the same state. As a result, the ground state of the fermionic system is given by the state where each level up to some energy defined as *Fermi energy* E_{F} is occupied by exactly one atom (D).

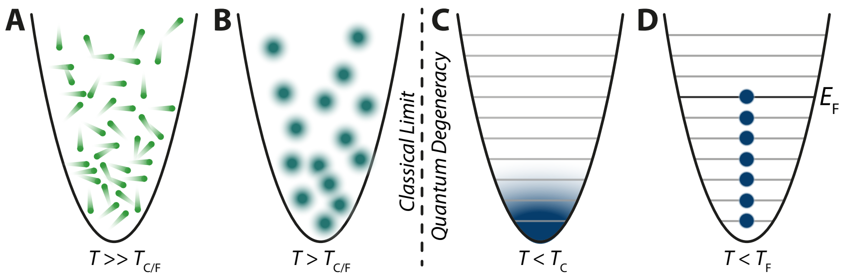

Figure 3.1: At high temperatures all particles behave point-like and the classical description is valid (**A**). Only when the temperature is lowered or in general the phase space density is increased (**B**), a description in terms of quantum mechanical laws becomes necessary. In this quantum degenerate limit bosons tend to accumulate in the lowest state of the system (**C**) while fermions fill up the levels with one particle each, starting at the lowest energy (**D**).

The temperature scale at which this crossover from the classical limit (A,B) to *quantum degeneracy* (C,D) occurs is given by the condensation temperature T_{C} for Bosons or by the Fermi temperature T_{F} for Fermions respectively. The Fermi temperature and the Fermi wave vector k_{F} are defined as

$$T_{\mathrm{F}} := \frac{E_{\mathrm{F}}}{k_{\mathrm{B}}} \qquad \text{and} \tag{3.1}$$

$$k_{\mathrm{F}} := \frac{\sqrt{2mE_{\mathrm{F}}}}{\hbar}. \tag{3.2}$$

The Fermi energy of N non-interacting Fermions in a three dimensional harmonic potential with average trapping frequency $\bar{\omega} = (\omega_x \omega_y \omega_z)^{1/3}$ is given by $E_\mathrm{F} = (6N)^{1/3}\hbar\bar{\omega}$. This E_F describes single component Fermi gases at low temperatures very well since short-range interactions are suppressed by the Pauli exclusion principle. For interacting systems and in order to relate experiments to theoretical models or to nature it is often useful to apply a *local density approximation* (LDA). This means that we assume that locally the gas in our trap behaves like a homogeneous system with a chemical potential $\mu(\boldsymbol{r}) = \mu_0 - V(\boldsymbol{r})$ that is modified by the external potential $V(\boldsymbol{r})$. This approximation is valid as long as the potential varies slowly over the correlation length of the system.

When applying an LDA it is more meaningful to compare the temperature T of the gas to the Fermi temperature of a non-interacting homogeneous gas. The latter is locally varying in a harmonic trap since it depends on the atom density ρ and is, in two dimensions, given by

$$E_\mathrm{F,2D} \equiv k_\mathrm{B} T_\mathrm{F,2D} = \frac{\hbar^2}{2m} 4\pi\rho_\mathrm{2D}. \tag{3.3}$$

Despite the presence of interactions the non-interacting homogeneous Fermi temperature $T_\mathrm{F,2D}$ does still give the approximate temperature scale below which quantum degeneracy is expected.

3.1.2 Interactions at low Temperatures

Alongside quantum statistics, also the inter-particle interactions have a crucial effect on the dynamics of atoms at low temperatures. The description of interactions is simplified a lot by the diluteness and low temperature of the gases. The low atom density justifies neglecting all higher orders than two-body scattering in most situations. Additionally, all atoms are in their electronic ground state and collisions happen at momenta that are too low to excite any internal degrees of freedom. By a transformation into the center-of-mass coordinate system the problem is reduced to the issue of elastic scattering of a single particle wavefunction in a potential. The latter is discussed in every standard textbook on quantum mechanics [Lan81] and we restrict ourselves to recalling the most important results for ultracold gases here.

Starting in three dimensions, the stationary Schrödinger equation for the scattering process in relative coordinates can be written as

$$\left(-\frac{\hbar^2\nabla^2}{2m_r}+V_{\text{int}}(\boldsymbol{r})\right)\Psi_k=E_k\Psi_k, \tag{3.4}$$

where m_r is the reduced mass, $\boldsymbol{r}$ the relative coordinate, and the potential $V_{\text{int}}(\boldsymbol{r})$ can be approximated by a spherically symmetric *Lennard-Jones potential* as depicted in Figure 3.2 A. In general, the only constraint on the form of the potential is that it has a finite range, i.e. $V_{\text{int}}(\boldsymbol{r})\to 0$ rapidly as $|\boldsymbol{r}|\to\infty$. Parallel to the solution of the hydrogen problem, the spherical symmetry of the potential allows us to perform a partial wave expansion of the wavefunction Ψ in terms of *Legendre polynomials* $P_l(\cos\theta)$ as

$$\Psi(r,\theta)=\sum_{l=0}^{\infty}A_lP_l(\cos\theta)R_{kl}(r). \tag{3.5}$$

Accordingly, the radial wavefunction $R_{kl}(r)$ has to satisfy the equation [Pet02]

$$\left[\frac{\partial^2}{\partial r^2}+\frac{2}{r}\frac{\partial}{\partial r}+k^2-\frac{l(l+1)}{r^2}-\frac{2m_r}{\hbar^2}V_{\text{int}}(r)\right]R_{kl}(r)=0. \tag{3.6}$$

The *potential barrier* $E_l=-(l(l+1))/r^2$ is of crucial importance since it suppresses all scattering processes with angular momentum quantum number $l>0$ for low relative particle momenta k. As a result, only *s-wave scattering* processes with $l=0$ contribute to the cross section σ in ultracold gases.

A solution is then obtained by approximating the radial wavefunction $R_{kl}(r)$ for $r\to\infty$ as

$$R_{kl}(r)\simeq\frac{1}{kr}\sin(kr-l\pi/2+\delta_l). \tag{3.7}$$

This term is equivalent to the observation that a finite ranged interaction potential $V_{\text{int}}(r)$ only adds a phase shift δ_l to each scattered spherical wave. At low temperatures all phase shifts δ_l with $l>0$ are suppressed by the potential barrier and the scattering process is described by the single parameter δ_0. Finally, the form 3.7 of the scattered wavefunction with restriction to $l=0$ and the following definition of the *s-wave scattering length a*

$$a=-\lim_{k\to 0}\frac{\tan\delta_0}{k}, \tag{3.8}$$

lead to the result for the total cross section

$$\sigma_{\text{tot}} = \frac{4\pi a^2}{1+k^2a^2}. \tag{3.9}$$

One differentiates between two different limits of this equation. In the first case, if $ka \gg 1$ one obtains

$$\sigma_{\text{tot}} = \frac{4\pi}{k^2}. \tag{3.10}$$

This is called the *unitary regime.* In this limit the dependence on the scattering length a drops out and the only remaining scale of the system is its density. In the second case, if $ka \ll 1$ one arrives at

$$\sigma_{\text{tot}} = 4\pi a^2 \tag{3.11}$$

In this limit the scattering process is independent of the momentum of the particles and the scattering length a is the single scale that describes all interactions.

So far, we completely neglected the symmetry constraints for indistinguishable particles on the wavefunction Ψ. When including these symmetry constraints one obtains

$$\begin{aligned} \text{Bosons}: &\qquad \sigma_{\text{tot}} = 8\pi a^2 \\ \text{Distinguishable Particles}: &\qquad \sigma_{\text{tot}} = 4\pi a^2 \\ \text{Fermions}: &\qquad \sigma_{\text{tot}} = 0 \end{aligned} \tag{3.12}$$

This confirms the statement above, that single component Fermi gases at low temperatures are non-interacting.

In order to simplify the description of the inter-particle interactions further, the realistic short ranged Lennard-Jones potential is replaced by an effective zero range potential $V_{\text{int}} = g\delta(\boldsymbol{r})$ with coupling strength g. Using this simple form of the potential, one can directly calculate dependence of the coupling strength g on the scattering length a. This relation depends on the dimensionality of the sytem and is given by [Wen13]

$$g_{\text{1D}} = \frac{-2\hbar^2}{ma_{\text{1D}}}, \qquad g_{\text{2D}} = \frac{-2\pi\hbar^2}{m\ln(ka_{2D})} \qquad or \qquad g_{\text{3D}} = \frac{4\pi\hbar^2 a_{\text{3D}}}{m}. \tag{3.13}$$

The two dimensional case is special since g does depend on the particle momentum k. One can approximate the momentum dependence k by the typical momentum of particles, which is given by the Fermi wavevector k_F in two- and three-dimensional fermionic systems. This motivates the utilization of the dimensionless scattering parameter $\ln(k_\mathrm{F} a_{2\mathrm{D}})$ to characterize the interactions in fermionic two-dimensional cold atom systems. One feature of such experiments is that this scattering parameter is not fixed but tunable over several orders of magnitude.

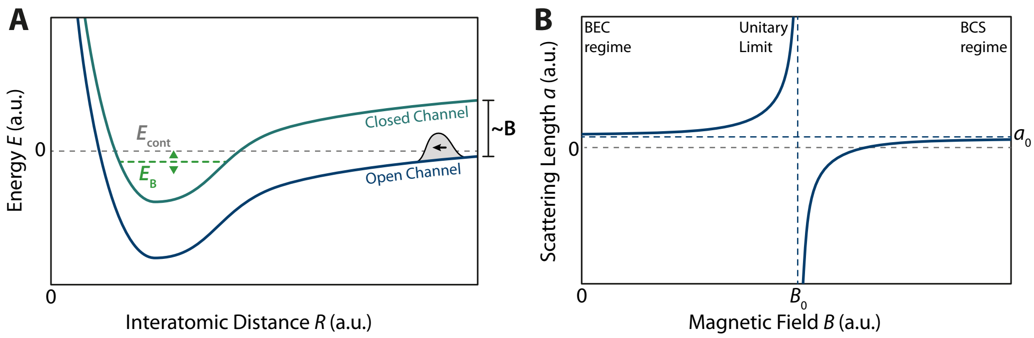

Figure 3.2: Feshbach resonances are used as a tool to tune the s-wave scattering length in atom collisions at low temperatures. A Feshbach resonance occurs when the energy E_B of a bound state of a closed channel coincides with the energy of the scattering particles (**A**). The value of the scattering length (**B**) can then be tuned by applying a magnetic offset field B.

3.1.3 Feshbach Resonances

Many of the achievements of cold atom experiments, especially those using fermionic species, rely on the control of inter-particle interactions via *Feshbach resonances*. Feshbach resonances can be understood in a rather simple picture using *interaction channels* [Chi10]. An interaction channel is given by a complete choice of quantum numbers for all in- and outgoing particles that participate in a scattering process. An *open channel* is a choice of quantum numbers where the total energy matches the actual energy of the scattered particles. A *closed channel* has a different continuum energy and is therefore energetically forbidden for the given set of particles (see Figure 3.2 A).

A Feshbach resonance occurs if the closed channel possesses a bound state with energy E_B close to the continuum energy E_cont of the scattered particles. This allows the incoming particles to scatter into an intermediate bound state in the closed channel which decays back into the open channel sequentially. This intermediate state has a large influence on the effective scattering length a_{eff} of this process, approximately given by [Pet02]

$$a_{\text{eff}} \propto \frac{1}{E_{\text{cont}} - E_{\text{B}}}. \tag{3.14}$$

In case the closed channel comes from a different internal hyperfine state of the atoms it is possible to adjust the distance of the bound state E_{B} to E_{cont} by applying a magnetic field offset B. The consequent shift of the scattering length can be approximated by the following phenomenological relation [Chi10]

$$a_{\text{eff}}(B) = a_0 \left(1 - \frac{\Delta}{B - B_0}\right), \tag{3.15}$$

where a_0 is the background scattering length at $B \to \infty$, B_0 is the resonance position where $E_{\text{B}} = E_{\text{cont}}$ and Δ is the width of the resonance (see Figure 3.2).

3.1.4 BEC-BCS Crossover

Now, that we introduced the relevant temperature and interactions scales for a two component Fermi gas, we will take a brief look on the related phase diagram. Surprisingly the fermionic system becomes superfluid at arbitrary interaction strengths if the temperature is low enough. Currently, there exists no complete theoretical description of the phase diagram, especially in the strongly interacting limit where a small parameter for perturbation theories is absent [Ran14]. Nevertheless, the two limiting mechanisms for superfluidity of weakly repulsive and weakly attractive Fermions are well understood. Experiments have shown that the unitary Fermi gas connects these two limiting cases smoothly. The strongly interacting regime, despite lacking reliable theoretical description, has attracted a lot of interest due to its remarkable properties, among them the highest known condensation temperature at $T_{\text{c}} \approx 0.2/T_{\text{F}}$, a pairing pseudogap in the normal phase and minimal viscosity to entropy ratio. The latter has recently been used to test a conjecture on the minimum of this ratio that was derived using the anti-de Sitter/conformal field theory correspondence [Cao11].

The mechanism of superfluidity is easily understood in the weakly repulsive regime in three dimensions noting that there exists a bound state with energy E_{B} =

$\hbar^2/(ma^2)$ for a scattering length $a > 0$. As a result, more and more fermions will form molecules when the gas is cooled. These tightly bound molecules are bosonic and at some temperature T_c they will therefore form a superfluid by the usual mechanism of Bose-Einstein condensation. Consequently, the repulsive regime with $a > 0$ is named BEC-limit (see Figure 3.3 A).

In the opposite limit of weak attraction there exists no two-body bound state in three dimensions and no tightly bound molecules can form. An alternative explanation for superfluidity was provided by Bardeen, Cooper and Schrieffer [Bar57]. They could show that weakly attractive Fermions possess an instability towards the formation of so-called *Cooper pairs*. In this way their *BCS-theory* provides the required mechanism for condensation of the gas. Contrary to the BEC-limit the Cooper pairing on the BCS-limit is a true many-body effect in the sense that it can only occur in the presence of a Fermi surface. Furthermore, Cooper pairs form in momentum space between particles with opposite momentum that are not localized in position space.

The intermediate region of the unitary Fermi gas is less well understood. However, through theoretical considerations in the zero temperature limit it is known that the unitary Fermi gas provides a smooth crossover between the two limiting regimes. As already mentioned, many experiments, for example from Zwierlein et al. [Zwi05], could provide evidence for this BEC-BCS crossover also at finite temperatures. A similar behaviour is observed in two dimensional Fermi gases (see Figure 3.3 B). In this situation the theoretical description for condensation deviates once more since true long range order is forbidden in two dimensions by the *Mermin-Wagner-Theorem* [Mer66]. Instead, the system can show *marginal behaviour* which will be discussed in the next section.

3.1.5 BKT Transition

The Mermin-Wagner-Theorem states that long-range order is impossible at non zero temperature in all one and two dimensional systems with short-range interactions and a continuous Hamiltonian symmetry. The underlying reason is that a broken symmetry is restored by thermal fluctuations in two dimensions (so-called *Goldstone modes*). As a result the mechanism of spontaneous symmetry breaking fails to explain the presence of the phase transition that is clearly observed in two dimensions. Berezinskii, Kosterlitz and Thouless presented an alternative formulation in the form of a topological phase transition in their celebrated work [Ber72; Kos73].

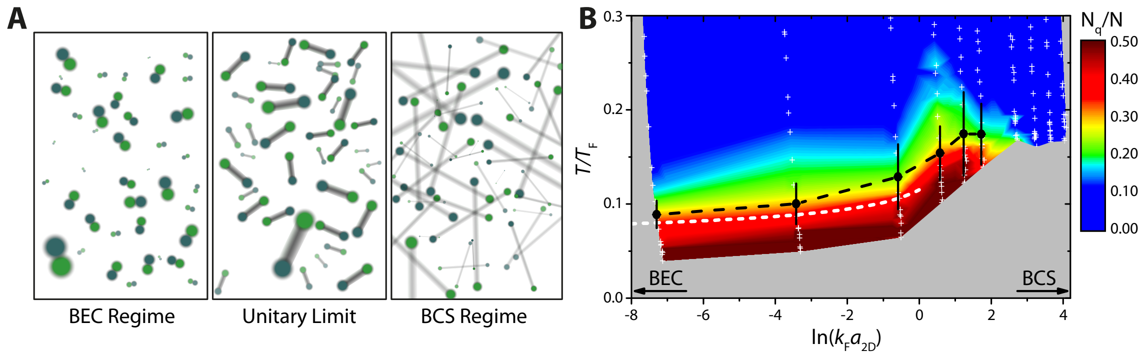

Figure 3.3: **A:** The phase diagram of a two component Fermi gas can be separated into three different regimes. First, the BEC limit where particles form tightly bound molecules which sequentially condense into the superfluid. At the opposite end, the BCS-regime is described by the formation of Cooper pairs in momentum space. In-between these limiting cases lies the strongly interacting regime that lacks a simple description.
B: Measurement of the condensation temperature T_C of a two component Fermi gas in two dimensions. The colour scale shows the fraction of condensed particles $N_\mathrm{q}/N_\mathrm{tot}$ in the system. Taken from [Rie15b].

They predicted that one and two dimensional systems can show *quasi-long-range order* or *marginal behaviour* at low temperatures where the correlations g in the system decay algebraically with distance r as

$$g(r) \propto r^{-\eta}, \tag{3.16}$$

with $\eta = 1/4$ for homogeneous systems. Consequently, we interpret the algebraic decay of correlation functions that we observe in our two dimensional experiment as evidence for the presence of a topological phase transition [Mur15b].

The topological phase transition can be understood in the picture of phase defects [Had09]. Below the transition temperature T_c all vortices with opposite sign form dipole pairs. The total circulation of a vortex dipole is zero and thus the phase defects have no effect on the condensate phase at length scales larger than the healing length ξ (see Figure 3.4 A). As a result quasi-long-range order persists despite the presence of phase defects or fluctuations. If the temperature is raised, it is at some point energetically favourable to break the vortex dipoles (see Figure 3.4 B). The free vortices do not immediately cancel each other out any more and superfluidity is destroyed.

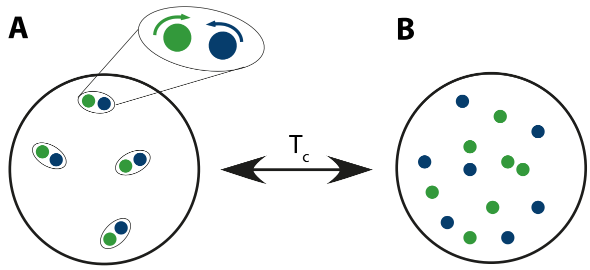

Figure 3.4: Below the transition temperature the vortices form pairs and a quasi-long-range order is restored (**A**). For temperatures above T_c the vortex pairs break up and destroy superfluidity (**B**). Adapted from [Had09].

3.2 Preparation of a Degenerate Fermi Gas

In this section we will present the current status of the experimental setup. The apparatus was initially set up to explore the BEC-BCS crossover in two dimensions. As discussed above, quantum fluctuations are increased in these systems and experiments in this regime are not only interesting from a theoretical viewpoint but they also have connections to quasi two dimensional systems in nature like high-T_c superconductors or graphene. As discussed in detail in chapter 2, two-dimensional systems are special from the viewpoint of turbulence as well, due to their strongly modified vortex dynamics.

In our experiment we are able to prepare the cloud in a highly anisotropic disc shaped trap, such that excited states in one spatial direction are thermodynamically inaccessible. As a result, we can go to a regime where all the dynamics of the system are truly two-dimensional as required for the observation of the two-dimensional BEC-BCS crossover. This requirement is a lot stricter than what is necessary to observe two-dimensional turbulence as was shown by [Kwo14]. Their experiment, in which they observed the relaxation of quantum turbulence, is performed in a trap with an aspect ratio of $\omega_r/\omega_z \approx 20$ in a cloud that was thermodynamically still three dimensional. In this sense we can easily fulfil the requirements for two dimensional turbulence and possibly even explore the crossover from two to three dimensional systems.

All our experiments are conducted in an octagon experimental chamber in ultra-high vacuum. This isolates our system from the environment while providing sufficient optical access through ten high numerical aperture viewports. In our experiment we could already explore many aspects of the BEC-BCS-crossover in the bulk gas successfully [Rie15b; Mur15b; Boe16; Mur17]. For these measurements a rather low optical resolution and static trap geometry were sufficient and therefore the apparatus was only slightly altered since it was built in 2009.

The next milestone we want to achieve now, is to set up experiments that also have single atom resolution and tailor-made and time dependent optical potentials. A large part of the work during the course of this thesis was put into the design, construction and testing of an extension of the experimental machine which is going to be added very soon. The new design includes a Spatial Light Modulator and a very high resolution objective that are described in detail in chapter 5. In this section we will limit ourselves to the current version of the experiment.

3.2.1 Hyperfine Structure of ^{6}Li

For all our experiments we use the isotope lithium ^{6}Li. The nucleus of ^{6}Li contains a total number of six protons and neutrons which leads, together with the three electrons, to fermionic spin statics of the atom in total. As mentioned before, at low temperatures all atoms are in their electronic $2S_{1/2}$ ground state. To produce an interacting Fermi gas of at least two components, we make use of the lowest three hyperfine levels of the ground state. We commonly label these states starting from lowest energy level as states $|1\rangle$,$|2\rangle$ and $|3\rangle$ (see Figure 3.5 A). All of these states are stable and we can convert different hyperfine populations into each other by applying radio frequency pulses, for example in the form of a Landau-Zener sweep.

For each of the three possible two component mixtures exists a broad Feshbach resonance that allows us to tune the interaction strength very precisely by applying a magnetic offset field (see Figure 3.5 B). All the measurements that were done for this thesis were performed in a spin balanced mixture of states $|1\rangle$ and $|2\rangle$ at magnetic fields between 600 and 1400 Gauss.

3.2.2 Experimental Setup

The two dimensional Fermi gas experiment is shown in Figure 3.6. As discussed before, the octagon experiment chamber lies at the heart of the device. A complete experimental cycle ends with the destructive imaging of the atoms and takes around ten to fifteen seconds. The experiment itself lasts only between one and four seconds, during the remaining time the gas is prepared. To this end, several cooling stages

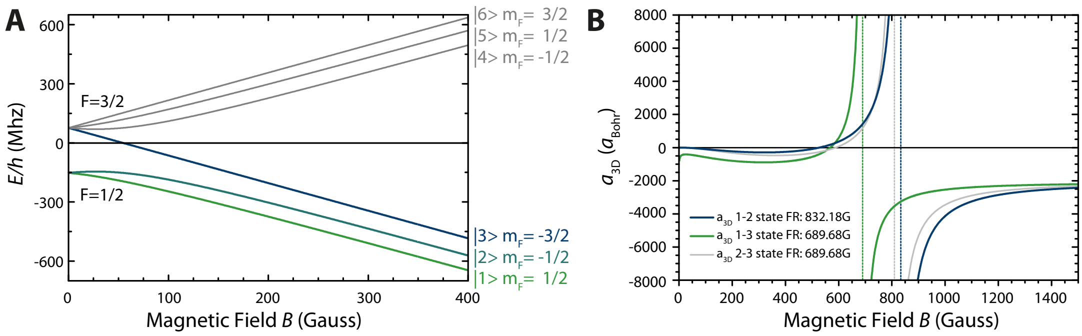

Figure 3.5: **A:** We use ^{6}Li atoms in their lowest three hyperfine levels in our experiment. At the magetic field we work at they are typically split by $\sim 80\,\mathrm{MHz}$.
B: All three possible mixtures have broad Feshbach resonances that allow us to accurately tune the interactions in the system.

were implemented in order to lower the temperature of the gas enough to cross the transition into the superfuid state at $T/T_\mathrm{F} \lesssim 0.2$.

First, lithium vapour is produced in an oven at a temperature of $T \approx 600\,\mathrm{K}$ and enters the machine as a beam of atoms through a small nozzle. The gas beam is cooled to a temperature of the order of one Kelvin by a Zeeman-Slower. The Zeeman-slower ends in the experimental chamber where the atoms are loaded into a magneto optical trap (MOT) which cools the gas down to temperatures of a few hundred microkelvins. Next, quantum degeneracy is achieved by evaporative cooling of the atoms in a high power crossed beam optical dipole trap down to $T \approx 70\,\mathrm{nK}$. Finally, the atoms are transferred from the crossed beam trap into a highly anisotropic optical dipole trap where all dynamics in one dimension are frozen out. The two optical dipole traps that are used in the final stages will be discussed in the next section in more detail.

Two sets of water-cooled coils are embedded into the experimental chamber to control magnetic fields. One set of coils (*MOT-coils*) is used in an anti-Helmholtz configuration to produce the magnetic field gradient of the MOT, while the other set of coils (*Feshbach-coils*) in a Helmholtz configuration produces a magnetic offset field. Both coil sets are stabilized by PID loops and allow us to precisely set experimental parameters like the scattering length.

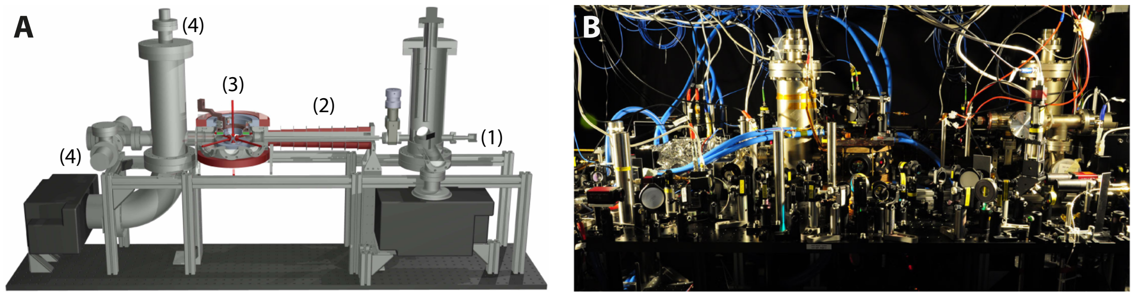

Figure 3.6: **A:** Overview over the experimental setup. Lithium is evaporated in the oven (1) from where it enters the Zeeman-Slower (2). The latter ends in the experimental chamber (3) where all the experiments are performed. The ultra-high vacuum is maintained by ion pumps and titanium sublimators (4). Taken from [Wen13]. **B:** Image of the present state of the experiment taken from the same perspective .

3.2.3 Optical Dipole Traps

In this section we will take a close look at the two optical dipole traps (ODTs) that are used in the final stages of the experiment. These traps will become useful for the excitations of collective modes as shown in chapter 4. The concept of ODTs is also important with regard to the spatial light modulator that we want to add to our experiment soon and thus we will quickly review the most important results here.

ODTs can be fully understood with the help of a quasi classical picture. When atoms are exposed to an oscillating light field $E(t)$, a dipole moment $D(t)$ is induced. This dipole moment oscillates with the frequency ω of the driving field $E(t)$ and leads to a force of the light field on the atoms. Analogous to a driven harmonic oscillator, a red detuned light field, with a driving frequency ω lower than the resonance frequency ω_0 of the atom leads to an oscillation in-phase with the drive. Hence, the resulting force is attractive (see Figure 3.7 A). A blue detuned light field, i.e. the oscillation is faster than the resonance frequency, leads to an out of phase oscillation and a repulsive force. In this way it is possible to shape arbitrary potentials for atoms by interfering laser beams in a clever way. The potential $V_{\mathrm{ODT}}(\boldsymbol{r})$ is directly proportional to the intensity of the light field $I(\boldsymbol{r})$ and is given by [Gri00]

$$V_{\mathrm{ODT}}(\boldsymbol{r}) \propto \left(\frac{1}{\omega_0 - \omega} + \frac{1}{\omega_0 + \omega}\right) I(\boldsymbol{r}). \tag{3.17}$$

For these traps direct photon scattering is highly unwanted since it heats up the

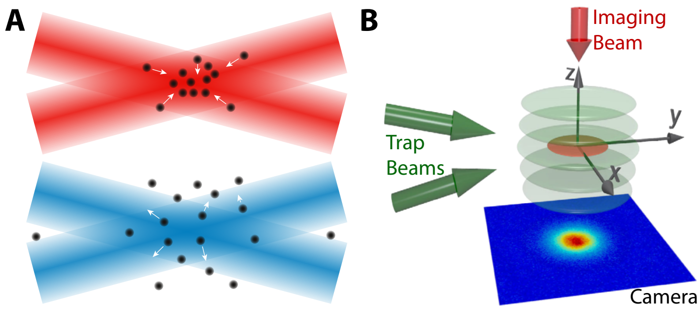

Figure 3.7: **A:** A simple optical dipole trap can be created by intersecting two laser beams. If the beams are red detuned atoms will be attracted towards regions of highest intensity (top). Blue detuned lasers create repulsive potentials (bottom). **B:** The two dimensional confinement is created by interfering two laser beams under a shallow angle. Taken from [Rie15b].

atoms. The background scattering rate Γ_{sc} is given by

$$\Gamma_{\mathrm{sc}} \propto \frac{1}{\omega - \omega_0} V_{\mathrm{ODT}}, \tag{3.18}$$

and therefore photon scattering can be suppressed by detuning the laser beams far from the transition frequency ω_0.

Currently, we make use of two different ODTs in our experiment. The crossed beam ODT is created by crossing two laser beams with powers up to 200 W and with perpendicular polarization such that they do not interfere, as shown in Figure 3.7 A. This creates a cigar shaped trap with an aspect ratio of about 10:1 (see Figure 3.8 A). The evaporative cooling stage is performed in this trap by gradually ramping down the trap depth in a controlled way. To improve the transfer of atoms into the following disc shaped ODT we can adjust the shape of the crossed beam ODT by quickly modulating its center position using acousto optical modulators (see Figure 3.8 B).

The second and most important trap of the experiment is the ODT that creates the two dimensional confinement of the atoms. This trap is created by two laser beams that interfere under a small angle of 14° such that their interference pattern contains several layers of highly anisotropic, disc shaped potentials (see Figure 3.7 B). We are able to load up to 95% of our atoms in one of these layers and measure ratios of trapping frequencies on the order $\omega_z/\omega_r \approx 300$ (see Figure 3.8 C). Here, z

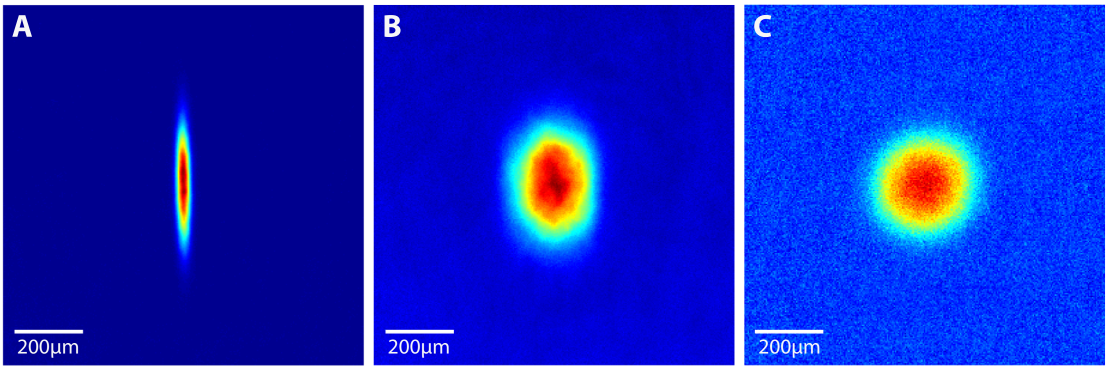

Figure 3.8: Absorption images of atom clouds inside our two ODTs with different geometries. Taken from [Rie15a].
A: The cigar shaped crossed beam ODT is used for evaporative cooling of the atoms **B:** The shape of the crossed beam ODT can be adjusted by fast modulation of the center position of the beams. **C:** Density distributions of atoms inside a single layer of the two dimensional confinement.

points in the direction of the strong confinement and $\omega_r = \omega_x \approx \omega_y$.

For atom numbers up to $N \approx 50000$ per spin state we observe that all the atoms are in the ground state of the confinement in z direction [Rie15a]. This confirms the statement that all the dynamics in the system lie in just two dimensions. As discussed in the beginning this is not a necessary requirement for the observation of two dimensional turbulence and thus we can also work with higher atom numbers in a thermodynamic three dimensional regime.

3.3 Detection Techniques

In cold atom experiments physical information is typically extracted by taking images of the atom cloud at the end of the experimental cycle. It is possible to differentiate between destructive imaging methods like absorption or fluorescence imaging and non-destructive methods like phase contrast imaging. The former rely on resonant light scattering and therefore transfer momentum to the atom cloud. In the current experimental setup we only employ absorption imaging yet, after having installed the extension of the experiment we can also take fluorescence images.

3.3.1 Absorption Imaging

The general idea behind absorption imaging is depicted in Figure 3.7. A resonant beam of light is sent through the atom cloud along the z-direction in our experiment and a camera image $I_{\text{abs}}(\boldsymbol{r})$ is taken. The attenuation of the laser beam is then given by the Lambert-Beer law. Therefore, we can extract the optical column density $n(\boldsymbol{r})$ of the cloud, after taking a second reference image $I_{\text{ref}}(\boldsymbol{r})$ without atoms and a third image $I_{\text{bg}}(\boldsymbol{r})$ without any light, as

$$n(\boldsymbol{r})\sigma_0 = \ln\left(\frac{I_{\text{abs}}(\boldsymbol{r}) - I_{\text{bg}}(\boldsymbol{r})}{I_{\text{ref}}(\boldsymbol{r}) - I_{\text{bg}}(\boldsymbol{r})}\right) \tag{3.19}$$

Here, σ_0 is the scattering cross section. It is worth mentioning that this formula is only accurate for laser intensities far below the saturation intensity I_{sat} of the transition. A detailed discussion of the corrections that need to be taken into account at higher intensities in our system is found in reference [Nei17].

In Figure 3.8, several examples for atom density distributions obtained through absorption imaging are shown. At the magnetic fields we work at, the typical distance of the hyperfine states of ^{6}Li is about 80 MHz with a transition linewidth of around 5 MHz. Therefore a single absorption image contains density distribution of a single spin component only. However, we are able to take a second absorption image that is resonant to the second hyperfine state in quick succession to obtain the full density distribution. This ability, which we refer to as *two state imaging*, enables us to measure spin correlations functions in our cloud.

3.3.2 Fluorescence Imaging

The biggest drawback of absorption imaging is the limited signal-to-noise ratio due to the photon shot noise and the saturation of the optical transition. This makes it very difficult to reach single atom resolution by taking absorption images. Instead, the method of fluorescence imaging has to be applied. The idea is to image the photons that are emitted by the atom cloud through the process of spontaneous decay, while it is excited by a resonant laser for example. These photons are emitted in random directions and have to be refocused on a camera by an objective. The number of collected photons is proportional to the number of atoms and to the time the cloud is imaged. This means that the signal-to-noise ratio can be reduced by increasing the exposure time. With the help of very sensitive cameras it is then possible to achieve single atom resolution with as little as 100 scattered photons as we will show in chapter 5.

3.3.3 T/4 Imaging

We already mentioned that it is possible to access the momentum distributions of cold atom clouds by means of a time of flight (TOF) expansion. The most frequently used procedure is to switch off all potentials to let the atoms spread out in free space according to

$$\boldsymbol{x}(t_{\mathrm{TOF}}) = \boldsymbol{x}_{\mathrm{i}} + \boldsymbol{p}_{\mathrm{i}} \cdot t_{\mathrm{TOF}}, \tag{3.20}$$

where $\boldsymbol{x}_{\mathrm{i}}$ and $\boldsymbol{p}_{\mathrm{i}}$ are initial position and momentum of the particles respectively. After sufficiently long expansion time t_{TOF} the contribution of the unknown initial position becomes negligible and $\boldsymbol{p}_{\mathrm{i}}$ is approximately given by $\boldsymbol{x}(t_{\mathrm{TOF}})$. This approximation becomes exact only at $t \to \infty$.

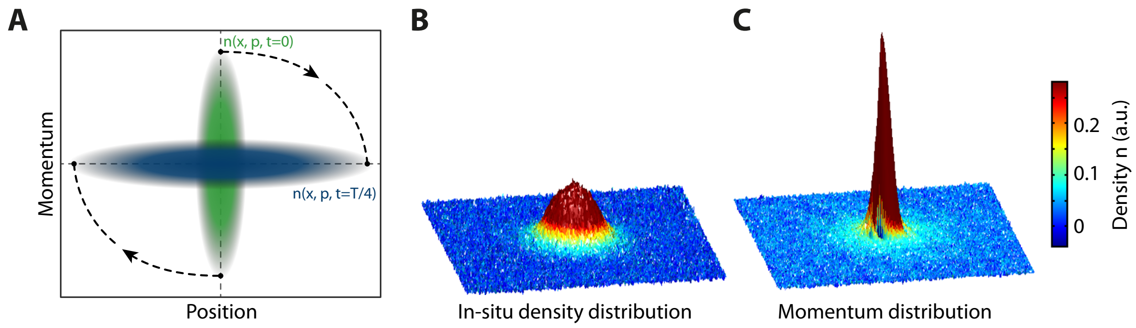

Figure 3.9: A modified time of flight expansion that provides access to the initial momentum distribution at finite times. Taken from [Mur14]. **A:** After a quarter trap period in a harmonic potential the momentum distribution is mapped onto positions and vice versa. **B:** In-situ picture of the cloud below the transition temperature T_{c} for superfluidity. No clear signal for superfluidity is observable. **C:** The Momentum distribution, as obtained via T/4-imaging, of the same cloud clearly show a macroscopic occupation of the ground state.

We implemented an improved version of this TOF expansion in our experiment. Instead of letting the cloud expand in free space we leave a residual, weak harmonic trapping potential switched on. Now, after a quarter of the trap period $t_{\mathrm{TOF}} = T/4$ the initial momentum distribution of the particles gets mapped exactly onto their final position $\boldsymbol{x}(t_{\mathrm{TOF}}) = \boldsymbol{p}_{\mathrm{i}}$ (see Figure 3.9). One can easily verify this claim for a particle in a classical harmonic oscillator and the result also holds in the quantum mechanical picture [Mur14]. In this way we can measure the exact momentum distribution that would appear at infinite times for a standard TOF expansion and a finite time $t_{\mathrm{TOF}} = T/4$, where $T = 2\pi/\omega_{\mathrm{harm}}$.

The consideration above is only valid as long as the atoms do not interact during the TOF expansion. To ensure that this is sufficiently well satisfied we quickly ramp to a magnetic field where inter-particle interactions are small, before starting the expansion. Additionally, the two dimensional confinement leads to a very fast initial expansion of the cloud in the third direction such that the gas quickly becomes too dilute to interact.

4 Measurements

In this section all measurements performed during this thesis are presented. They are based on the excitation of collective dipole, breathing and quadrupole modes in our two dimensional confinement ODT. These modes provide access to different hydrodynamical or equilibrium observables like the equation of state or the viscosity of the gas. We characterized the dependence of the quadrupole frequency and damping rate on inter-particle interactions with an unprecedented accuracy for the two dimensional Fermi gas. In order to search evidence for turbulence in our systems we extracted the momentum distribution of our atoms through TOF measurements. Additionally, we looked for phase defects directly in images taken after a short period of expansion of our gas. At the end of the chapter we will present recent measurements of the breathing mode showing a frequency doubling effect in the superfluid phase.

4.1 Trap Frequencies

In order to normalize the following measurements correctly a precise determination of the harmonic frequencies of our trap is necessary. To this end, we load a single spin component Fermi gas in our trap. As discussed before, a single spin component gas at low temperature is non-interacting and thus the frequency of the breathing mode ω_{B} is exactly given by

$$\omega_{\mathrm{B}} = 2\omega_{\mathrm{R}}. \tag{4.1}$$

We excite this monopole mode in our single component gas and measure the oscillation of the cloud widths over time. The excitation procedure we use to this end is discussed in section 4.3. As expected, we observe an undamped oscillation with a single frequency and some background heating on top (see Figure 4.1 A). By fitting a superposition of a sine and a linear gradient to this data we extract the trap frequencies $\omega_{x,y}$ in x- and y-direction. The latter vary with the magnetic offset field

B since our Feshbach coils produce a magnetic quadrupole confinement in addition to the ODT potential. By measuring the trap frequency at different magnetic fields and fitting its expected dependence on B to this data, given by

$$\omega(B) = \sqrt{\omega_0^2 + aB}, \tag{4.2}$$

we obtain an accurate frequency calibration at arbitrary magnetic field strengths (see Figure 4.1 B). Here, the fit parameters are the frequency ω_0 of the potential that is produced by the ODT alone and some coefficient a that depends, for example, on the geometry of our trap and the magnetic dipole moment of our atoms.

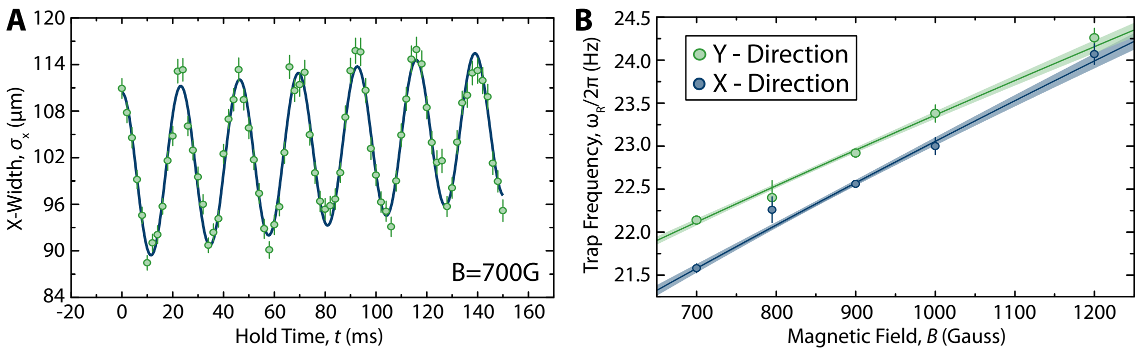

Figure 4.1: **A:** Oscillation of the trap width in x direction after exciting a breathing mode in a single component Fermi gas. **B:** Measurements of the trap frequencies at different magnetic fields B. The solid lines are least square fits of equation 4.2 to this data with 1σ-confidence bands.

In the region we are interested in, we measure trap anisotropies $|\omega_y/\omega_x - 1|$ from 0.5 % at 1250 G up to a maximum of 2.5 % at 690 G . This justifies neglecting these small deviations completely and working with an averaged frequency

$$\omega_\mathrm{R} = \frac{1}{2}(\omega_x + \omega_y) \tag{4.3}$$

instead. The same procedure is used while imaging the cloud along the x axis to obtain the frequency ω_z in the strongly confined direction. It is given by

$$\omega_z = (7.14 \pm 0.09)\,\mathrm{kHz}. \tag{4.4}$$

With a mean radial frequency of approximately $w_\mathrm{R} = 23\,\mathrm{Hz}$ this leads to an anisotropy of $\omega_z/\omega_\mathrm{R} \approx 310$ and restricts all the dynamics to two dimensions.

4.2 Dipole Mode

The dipole mode is an oscillation of the center of mass of the atoms cloud that leaves the density distribution unaltered otherwise. As a result it is completely insensitive to the hydrodynamic properties and the equation of state of the system and we just use it to verify our trap frequency calibration at this point.

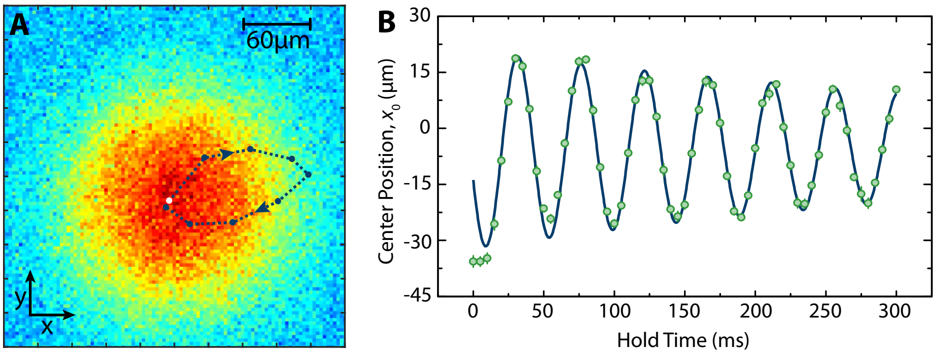

Figure 4.2: **A:** In a harmonic trap the dipole mode leaves the density distribution of the cloud unaltered. Instead the whole cloud moves along an elliptical path in the trap as indicated. **B:** Shift of the center of mass of the cloud in x-direction as function of time. The blue line is a damped sine fit to the data

The dipole mode is excited by adiabatically ramping on the current through the MOT coils. This produces an additional magnetic field gradient that slowly displaces the center position of our trap up to several hundred μm. By suddenly switching the MOT coils off again, a harmonic oscillation of the cloud in both directions is initiated sequentially (see Figure 4.2). A sine function to the center position leads to the following frequencies for a single component Fermi gas at $B = 800\,\mathrm{G}$

$$\begin{aligned} \omega_x &= 2\pi \times (22.22 \pm 0.05)\,\mathrm{Hz}, \\ \omega_y &= 2\pi \times (22.69 \pm 0.17)\,\mathrm{Hz}. \end{aligned} \tag{4.5}$$

These measurements agree well with our breathing mode calibration of $\omega_x = 22.08 \pm 0.03\,\mathrm{Hz}$ and $\omega_y = 22.54 \pm 0.03\,\mathrm{Hz}$ at this magnetic field. The slightly higher frequencies of the dipole mode can be explained by the anharmonicity of our trap. Since our excitation procedure for the dipole mode creates oscillations of significantly higher amplitudes than those we use for the breathing mode, the former is much more sensitive to higher order terms of the potential. The observation that the damping rate of the dipole mode is more than a factor two larger than that of the breathing mode strengthens this theory further. Indeed, a measurement at even higher amplitudes shifts the frequencies of the dipole oscillations of the single component Fermi gas even further to $\omega_x = 22.27 \pm 0.03\,\mathrm{Hz}$ and $\omega_y = 22.86 \pm 0.03\,\mathrm{Hz}$. This dependence of the frequency on the oscillation amplitude is the direct evidence for a small anharmonicity of our potential.

In conclusion, the frequency measurements of the dipole oscillation strengthen our confidence in our trap frequency calibration. We observe the same anisotropy between x- and y-axis of our trap. Additionally, we see that for higher amplitudes the dipole mode damps out more quickly and its frequency shifts by up to 0.5 Hz. If we extrapolate this data to the zero amplitude limit we see a perfect agreement with the breathing mode measurements at very low amplitudes.

4.3 Breathing Mode

The breathing mode is not only useful for a calibration of the trap frequency it is also relevant from a theoretical viewpoint since it is connected to an SO(2,1) symmetry of the system [Pit97]. It is predicted that in two dimensions this symmetry is broken by a quantum anomaly [Ols10]. This quantum anomaly has not yet been observed experimentally so far. Therefore, we repeated the study of the breathing mode, initially reported by Vogt et al. [Vog12], in our experiment.

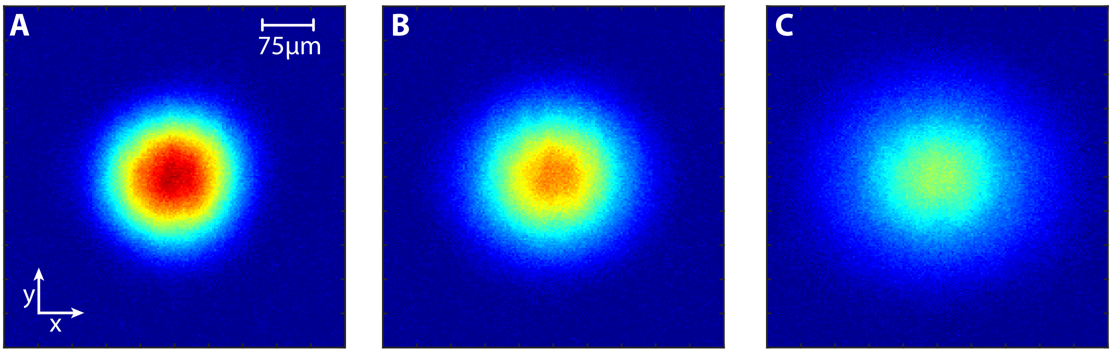

Figure 4.3: Insitu images of the cloud 68, 72 and 80 μs (**A**-**C**) after exciting a breathing mode oscillation. These images have been produced by modulating the inter-particle interactions via the magnetic offset field.

4.3.1 Excitation Procedure

In order to excite the breathing mode, several different techniques can be applied in our experiment. The simplest method is to gradually lower the depth of the two dimensional confinement as far as possible without losing atoms. The weakened confinement leads to an expansion of the cloud in the trap. A sudden ramp of the trap depth back to its original value initiates a breathing mode oscillation of the cloud sequentially. This method works for both single and two component gases and leads to an oscillation of the cloud radius with rather small amplitude, independent of the magnetic field (see Figure 4.4). For this reason we use it for both the trap frequency calibration and the interaction dependence measurements in this section.

A second possibility is a quench or sinusoidal modulation of the magnetic offset field B which allows us to manipulate the inter-particle interactions and the local chemical potential $\mu(\boldsymbol{r})$ of the cloud. For example, a modulation of the magnetic field for ten periods with a sine function at twice the trap frequency $\omega_{\mathrm{drive}} = 2\omega_{\mathrm{R}}$ produces a breathing mode with a very large amplitude (see Figure 4.3). The initial amplitude does depend on the offset field B in this case and thus this procedure is less suited for precise measurements. On the other hand, we can excite a lot higher amplitudes in this way which leads to some interesting observations like a frequency doubling in the superfluid phase that will be discussed later.

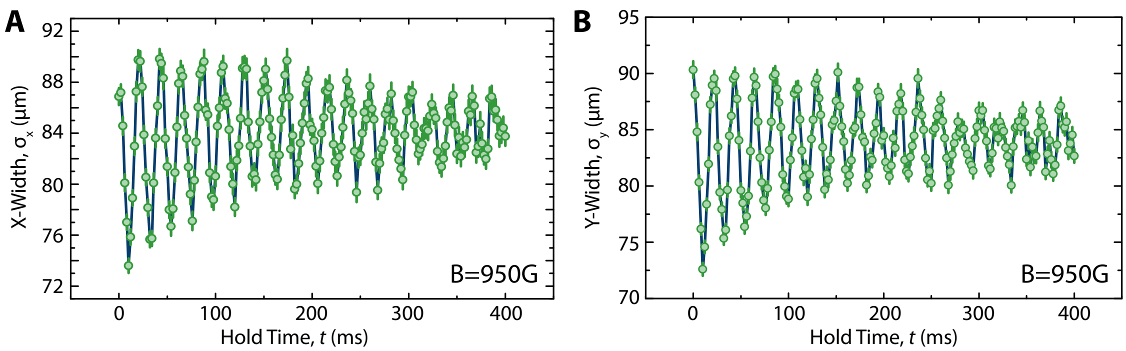

Figure 4.4: Time dependence of the cloud widths in x- and y-direction (**A**, **B**) after adiabatically lowering the ODT potential and suddenly switching it back on at $t = 0$.

4.3.2 Measurements

To extract the dependence of the frequency and damping rate of the breathing mode on the interactions we excite it at different magnetic fields and take insitu images after different hold times t. We sum these images along one axis and fit a Gaussian function to this data to extract the cloud widths σ_x and σ_y respectively. In Figure 4.5 we show both the sum and the difference of σ_x and σ_y for one particular magnetic field over a time of 400 ms or approximately 20 oscillations periods.

The sum of σ_x and σ_y shows very clear breathing mode oscillation without contributions from any higher collective modes up to our measurement accuracy. This is also observed in the difference of the cloud widths, which is consistent with zero for all measured magnetic fields even at very large times. This is expected in the high field regime where the anisotropy of our potential goes to zero. At lower magnetic fields where the anisotropy of 2.5 % is not negligible for non-interacting systems this is a first hint that we enter the hydrodynamic regime of the cloud. In this regime the interactions lock the frequency in x- and y- direction [Vog12].

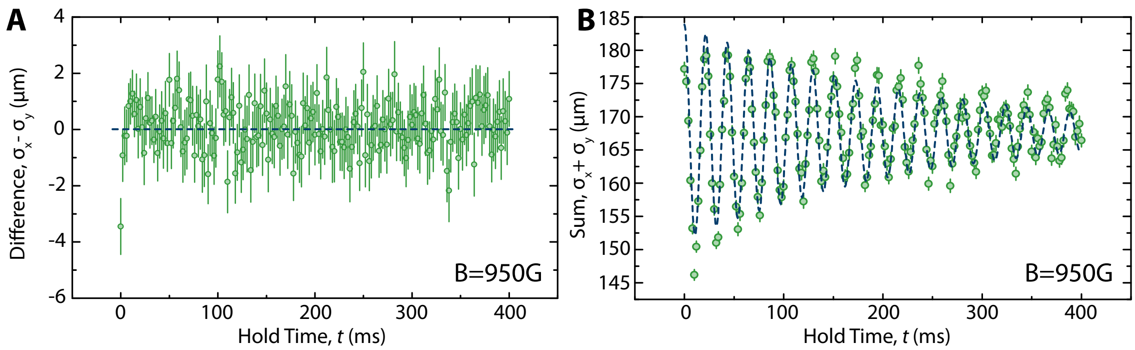

Figure 4.5: **A:** The difference of the cloud widths in x- and y-direction shows no time dependence and stays at zero for all measured times. **B:** The sum $\sigma_x + \sigma_y$ shows a clear sinusoidal oscillation of the breathing mode. We fit a damped sine function to this data (blue line).

In order to extract the frequency ω_{B} and damping rate Γ_{B} of our breathing mode we fit the following damped sine function to the sum of the cloud widths

$$W(t) = Ae^{-\Gamma_{\mathrm{B}}t}\sin(\omega_B t + \phi_0) + h \cdot t + W_0. \tag{4.6}$$

We introduced the second term to account for a technically induced heating of the cloud during the hold time. All the measurements have been performed at the lowest temperatures we reach in our experiment. All the data with $\ln(k_F a_{2D}) \lesssim 3$ has therefore been taken below the transition temperature T_c to a superfluid [Rie15b]. We extract the Fermi wavevector k_F of the system by averaging over the density profile of the cloud and over several oscillations of the breathing mode.

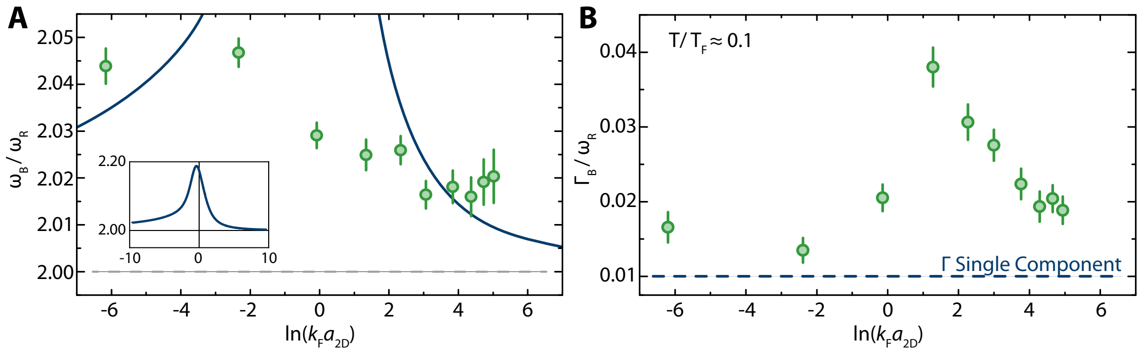

Figure 4.6: **A:** Measured frequency shift of the breathing mode oscillation in dependence of interactions. We compare our data to a theoretical zero temperature prediction by Hofmann [Hof12] (blue line, inset). The errorbars are given by the statistical uncertainties of our fits. **B:** As expected, we measure only very small damping rates that are close to the limit of a non interacting single component gas.

Figure 4.6 shows the measured dependency of the oscillation frequency ω_B and of the damping rate Γ_B on the inter-particle interactions. As expected, we observe that the breathing mode is only very weakly damped at arbitrary interaction strengths and that its frequency shows only very small deviations from $2\omega_R$. We postpone the detailed discussion of the results to the next section and focus now on the momentum distribution measurements instead.

The momentum distributions have been obtained by our modified TOF procedure that was discussed in chapter 3. We have studied the dynamics in the momentum distribution both on small time scales during a single period of the oscillation and on long time scales after many periods. The momentum distribution clearly shows the macroscopic occupation of low momentum modes that is expected for the superfluid phase. On short time-scales we see the oscillation of this condensate peak with the breathing mode frequency $\omega_B \approx 2\omega_R$ (see Figure 4.7 A). For very large oscillation amplitudes we observe a doubling of that frequency to $\omega_B = 4\omega_R$ that we examine closer at the end of this chapter.

On long time scales we see no change in the momentum distribution apart from a slow decay due to residual background heating (see Figure 4.7 B). From the viewpoint of turbulence it follows that it is not possible to excite turbulent dynamics by using the breathing mode. Energy is not transported in momentum space at all since the breathing mode does not contain shear movements.

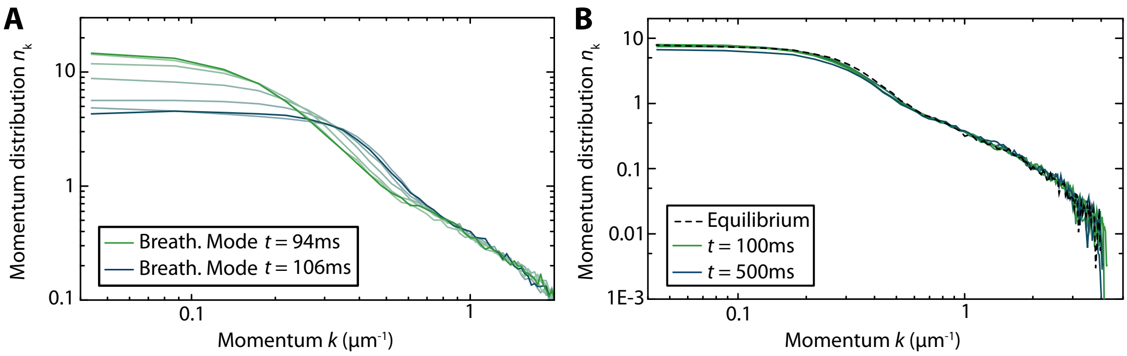

Figure 4.7: **A:** On short time-scales we observe the breathing oscillation of the condensate peak in momentum space. Momentum distributions for different times between one oscillation maximum at hold time $t = 94\,\mathrm{ms}$ and the following minimum at $t = 106\,\mathrm{ms}$ are plotted. **B:** On long time-scales the breathing mode has no effect at all on the momentum distribution of the cloud. Several curves between $t = 100\,\mathrm{ms}$ and $t = 500\,\mathrm{ms}$ are plotted that have been measured at the same phase of the oscillation.

4.3.3 Discussion

The behaviour of the breathing mode is best understood from the viewpoint of symmetries. The $\delta(\boldsymbol{r})$ potential in the Hamiltonian that is used to describe the interactions of cold atoms leads to a scale invariance of the system. This means that under the transformation $\boldsymbol{r} \to \lambda \boldsymbol{r}$ the potential and kinetic energy terms in the Hamiltonian scale the same, i.e. $\mathrm{H}(\boldsymbol{r}) \to \mathrm{H}(\boldsymbol{r})/\lambda^2$. An additional harmonic potential $V \propto \boldsymbol{r}^2$ obviously breaks this scale invariance. It is replaced by a SU(2,1) symmetry in this case. The SU(2,1) group can be represented by the group of rotations in a 2+1 dimensional space-time. Pitaevskii and Rosch [Pit97] were able to show that a trapped gas that inherits this symmetry has a breathing mode with the exact frequency $\omega_\mathrm{B} = 2\omega_R$ independent of the interaction strength.

In line with the previous obervations from [Vog12], our measurements confirm this prediction with deviations from $2\omega_\mathrm{R}$ to a few percent level. From the measurements of the quadrupole mode that are presented in the next section we know that for a range of $-3 \lesssim \ln(k_F a_{2\mathrm{D}}) \lesssim 3$ we are close to the hydrodynamic limit. At this limit the equation $\omega_\mathrm{B} = \sqrt{2\gamma + 2}\,\omega_\mathrm{R}$ holds and it follows that the EOS is polytropic with a polytropic index $\gamma = 1$.

We notice that even though our data agrees on qualitative level with the $2\omega_\mathrm{R}$ prediction, there is also a significant offset to larger frequencies. This can be explained by a *quantum anomaly* that has been predicted to occur in two dimensions. The term quantum anomaly has been introduced in the framework of quantum field theories and describes situations where a symmetry of the classical action is broken by its corresponding regularized quantized theory. In the case of the Fermi gas in a two dimensional harmonic confinement the regularization of the delta potential by a short range cut-off leads to breaking of scale invariance [Tay12]. Different analytical consideration and Monte-Carlo simulations have predicted interaction dependent shifts of the monopole frequency $\omega_\mathrm{B}/\omega_\mathrm{R} = 2$ by this anomaly on scales from one 1 % to 20 % [Ols10; Tay12; Hof12; Gao12]. The predictions agree on the observation that the breathing mode frequency is shifted to larger values.

We compare our data to the zero temperature calculation from Hofmann [Hof12] (see Figure 4.6). We observe the predicted trend to higher frequencies in the right interaction range on a qualitative level, however our deviation is only of the order of 5 %. This could arise from temperature fluctuations since our gas has a non-zero temperature of $T/T_\mathrm{F} \approx 0.1$ or from a coupling to the quadrupole mode. Both lead to a shift to lower frequencies since the quadrupole has a frequency of $\omega_\mathrm{Q} = \sqrt{2}\omega_R$ at these interactions. A weak coupling of quadrupole and breathing mode is for example induced by the small anisotropy of our potential. The temperature dependence of this effect could also explain why Vogt et al. [Vog12] were not able to observe the predicted trend to higher frequencies in the expected regime at temperatures of $T/T_\mathrm{F} \approx 0.4$.

In conclusion, we believe that we see an effect of the quantum anomaly on the exact scale that is expected for non zero temperatures in our cold atom cloud. However, the effect is rather small and thus is it necessary to be aware of all the possible systematic error sources to not mistake some of them for the quantum anomaly. Most of these effects like trap anisotropy and temperature lead to a shift to lower frequencies and can therefore not explain our measurements. The largest remaining sources for errors are the calibration of our trap frequency ω_R and possible anharmonicities. In order to obtain a lower limit for the observed effect we have compared our data to the larger of our two slightly different trap frequencies ω_y instead of the average ω_R. This data shows the same trend to frequencies above $2\omega_\mathrm{R}$ with a maximum of $2.025\omega_\mathrm{R}$. This further increases our confidence in the presence of a real effect.

The damping rates we observe for the breathing modes are very small, close to the non-interacting limit of a single component gas. We observe a sharp feature around $\ln(k_\mathrm{F} a_{2D}) = 1$ that we do not fully understand as of yet. The peak in the damping rate could for example be explained by a coupling to the quadrupole mode due to the anisotropic trap. The quadrupole mode has a larger damping rate at all measured interactions and would thus lead to an increased damping here. This does however not explain why the damping rate drops again for $\ln(k_\mathrm{F} a_{2D}) < 1$, since the trap anisotropy increases monotonously with lower interaction parameters. Another option could be that this peak is somehow connected to the transition into the superfluid that occurs roughly at this point when coming from larger interaction parameters $\ln(k_\mathrm{F} a_{2D}) > 1$.

4.3.4 Outlook

There are several measurements we could perform in the future to improve our confidence in the observation of the quantum anomaly. Firstly, we could vary some of the trap parameters like its frequency or its anisotropy to check what effect these parameters have on our observations. A second option is to prepare a different two component mixture. All the measurements that are presented here were carried out in the $|1\rangle$-$|2\rangle$ mixture. By preparing a gas of the two ground states $|1\rangle$ and $|3\rangle$ instead, we obtain a system that feels the same trap potentials at different interaction parameters $\ln(k_\mathrm{F} a_\mathrm{2D})$. If this leads to a shift of our measured curves in dependence of $\ln(k_\mathrm{F} a_\mathrm{2D})$ we know that our observation has been created by systematic errors and is not an effect of the quantum anomaly. Finally, it would be interesting to take curves at different temperatures, especially in order to get a better understanding of the sharp feature in the damping rate Γ_B and to be able to compare our measurements to the data from [Vog12] directly.

4.4 Quadrupole Mode

In contrast to the breathing mode, the quadrupole mode is a pure surface mode that does contain shear movements and it can therefore be used to probe the shear viscosity of the fluid. A detailed study of the quadrupole mode in a two dimensional Fermi gas was already reported by Vogt et al. [Vog12] in 2012. In this work they observed a very good qualitative agreement of the quadrupole mode frequency and its damping rate with predictions they obtained from kinetic theory. However, due to technical limitations and higher temperatures of their atoms they did measure significantly higher damping rates than the ones predicted. Consequently, they were not able to observe the quadrupole mode very far in the hydrodynamic limit where $\omega_\mathrm{Q} = \sqrt{2}\omega_\mathrm{R}$. For these reasons we repeated the characterization of the quadrupole mode at lower temperatures just above the transition to a superfluid in our systems. We are able to reach the hydrodynamic frequency limit in this way and find a perfect agreement with the theory in addition.

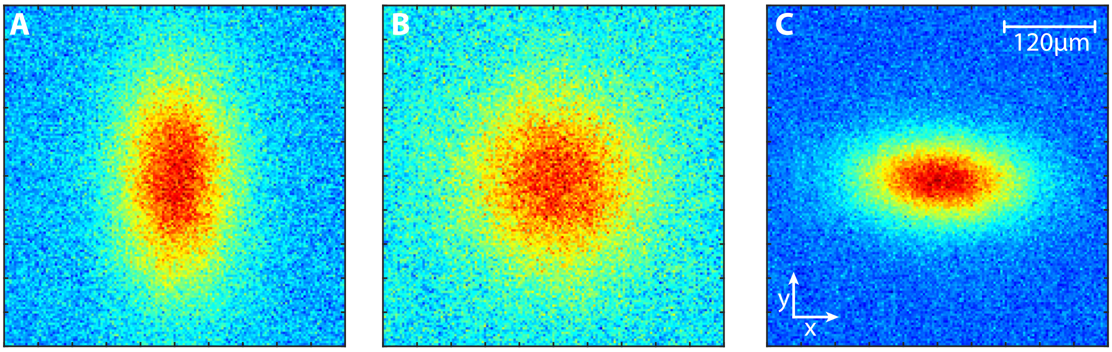

Figure 4.8: Insitu images of the cloud at 0, 4 and 12 μs (**A**-**C**) after exciting a quadrupole mode oscillation. A comparison of Figures **A** and **C** reveals a significant compression of the cloud along with the surface mode.

4.4.1 Excitation

To excite the quadrupole mode of our cloud we resort to our second crossed beam ODT (see Figure 3.8 A). While our atoms are trapped inside the two dimensional confinement we gradually ramp on this trap in addition. This leads to a redistributions of the atom density in our trap such that the cloud becomes elongated along the axis of the crossed beam trap (see Figure 4.8 A). By switching the second potential off again, we initiate a quadrupole motion (see Figure 4.8 B and C).

This technique leads to some additional compression of the cloud while both potentials are superimposed and as a result we observe a substantial contribution from the breathing mode to the oscillations (see Figure 4.9). We note that even at the lowest currently available power setting the ODT laser already excites oscillations with rather high amplitude. Thus, all the measurements that are presented in the following were taken at rather large relative amplitudes of $\sim 25\,\%$.

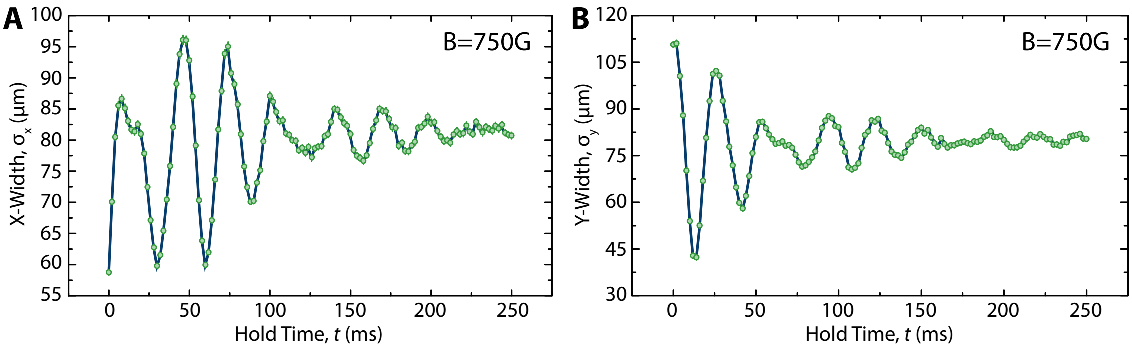

Figure 4.9: Time dependence of the cloud widths in x- and y-direction (**A**, **B**) after slowly ramping on the crossed beam ODT and suddenly switching it back off at $t = 0$.

4.4.2 Measurements

To extract the frequency and damping rate of the quadrupole mode we proceed just like we did when investigating the breathing mode. We excite the oscillation at many different magnetic fields and extract the quadrupole and breathing contribution by taking the difference and sum of the cloud widths σ_x and σ_y at different hold times t (see Figure 4.10). We observe similar amplitudes for both breathing and quadrupole and no, or only negligible contribution of higher order collective modes. This separation into quadrupole and breathing mode is only valid in the limit of an isotropic trap since any isotropy leads to a coupling of the modes. We neglected any residual coupling in this work since our average trap anisotropy is given by only $1\,\%$.

Figure 4.11 A shows measurements at several different magnetic fields. We use the same equation 4.6 as for the breathing mode to extract damping rate and frequency from this data. Evaluated qualitatively, we observe that the damping rate and the breathing mode are connected through the universal relation given in equation 2.27

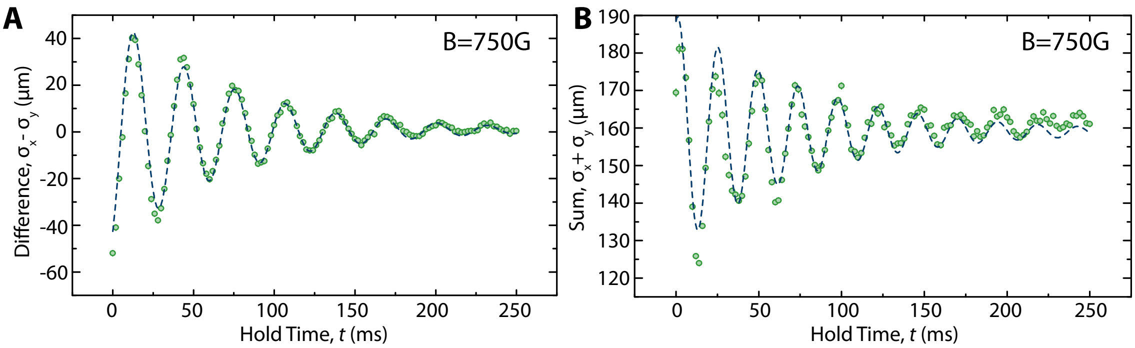

Figure 4.10: **A:** The difference of the cloud widths clearly reveals that we excite a quadrupole mode with the ODT ramping technique discussed in the text. **B:** The sum of the cloud width shows a contribution of a breathing mode of around 50 % to the oscillation. The dashed blue lines are sine fits to the data.

(see Figure 4.11 B). This confirms that we do actually observe the quadrupole mode in the observable $\sigma_x - \sigma_y$ and that it is decoupled well from the breathing mode. The small deviation of measurement at $\ln(k_\mathrm{F}a_\mathrm{2D}) > 0$ for low frequencies can be explained by the small anharmonicity of our trap. The calibration of the trap frequency ω_R has been performed for low amplitudes only and it becomes less accurate in this large amplitude regime. From our measurements of the dipole mode we know that this leads to a systematic error of one or two percent, i.e. on the same scale as the deviations we observe here. For the regime with $\ln(k_\mathrm{F}a_\mathrm{2D}) < 0$ other effects like, for example, a larger background heating rate lead to additional shifts. Nevertheless, our data agrees with the universal relation overall and deviations are on the few percent level only. Additionally, we observe that we reach the hydrodynamic limit of $\omega_\mathrm{Q}/\omega R = \sqrt{2}$ over a large range of interactions. These are the first measurements of the quadrupole mode of the two dimensional Fermi gas this far in the hydrodynamic limit.

The measured dependence of the quadrupole frequency ω_Q and its damping rate Γ_Q on the interaction parameter $\ln(k_\mathrm{F}a_\mathrm{2D})$ are shown in Figure 4.12 together with a theoretical calculation for a classical gas at $T/T_\mathrm{F} = 0.2$. We estimate the average temperature of our cloud by fitting a Boltzmann EOS to the wing of the measured insitu density distribution [Boe16]. By averaging over several quadrupole oscillations this leads to $T/T_\mathrm{F} = 0.22 \pm 0.05$ which is just above the transition temperature to a superfluid [Rie15b]. The results show again that we are in the hydrodynamic limit

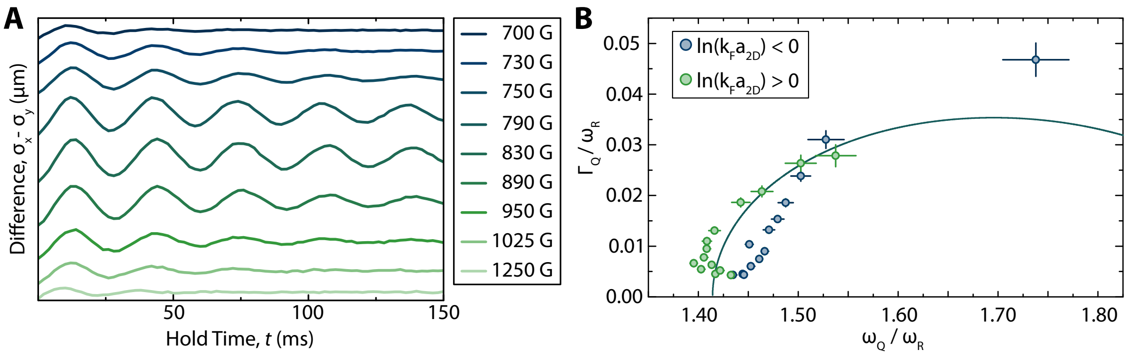

Figure 4.11: **A:** Quadrupole oscillations at different magnetic fields. In contrast to the breathing mode we observe a strong interaction dependence.
B: Damping rate versus frequency of the quadrupole mode. The solid line shows the universal relation that is expected between these two quantities.

for a large range of interactions. We see the onset of the transition to the collisionless regime around $\ln(k_{\mathrm{F}}a_{2D}) \approx 2$, however we are not able to follow the curve up to the limit of $\omega_{\mathrm{Q}} = 2\omega$ since for the broad Feshbach resonance of lithium this would require larger magnetic fields than we can currently reach in our experiment.

To confirm that our gas shows the correct behaviour in the connectionless limit nevertheless we have taken one additional measurement with a single component gas. The latter corresponds to a two component gas at $\ln(k_{\mathrm{F}}a_{2D}) \to \infty$. We measure a frequency of $\omega_{\mathrm{Q}}/\omega_{\mathrm{R}} = 1.99 \pm 0.01$ and a very low damping rate of $\Gamma_{\mathrm{Q}}\omega_{\mathrm{R}} = 0.035 \pm 0.002$. We postpone a detailed discussion of the theoretical models and expectations to the next section and concentrate on the momentum space measurements now.

We have tested several different driving schemes at different magnetic fields in order to study how the quadrupole mode affects the momentum distribution of the gas and whether we can excite turbulent motion in some way. For all the different excitation procedures, among them, for example, a continuous excitation scheme through sinusoidal modulation of the crossed-beam ODT, we qualitatively observe the same behaviour (see Figure 4.13 A). The decay of the quadrupole mode leads to a very quick increase of the temperature of the gas and thus to an increase of the atom number at large momenta. This shift of energy from large to small length scales does not occur locally in momentum space however. Instead the large scale

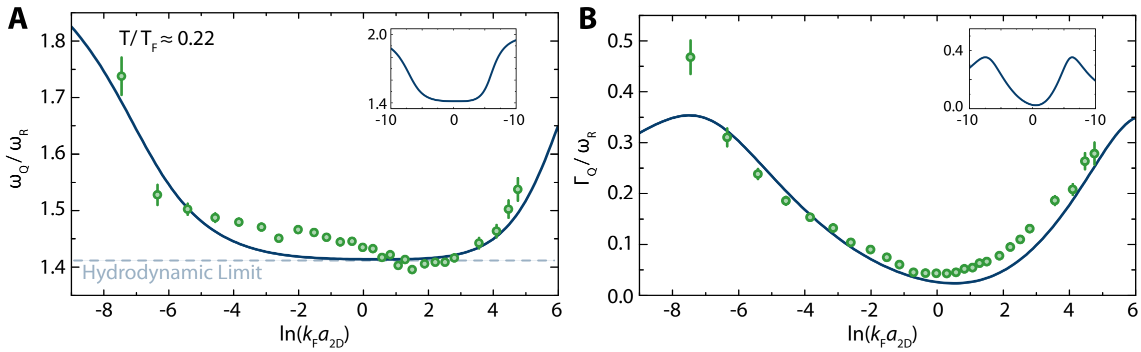

Figure 4.12: **A:** At low temperatures just above the superfluid transition we observe that we stay far in the hydrodynamic regime for a large range of interactions strengths. A theoretical calculation for a classical gas at $T/T_\mathrm{F} = 0.2$ (blue line, inset) shows a remarkable agreement with our data. **B:** We measure very low damping rates, in line with the same theoretical prediction. The single outlier at $B = 690\mathrm{G}$ can be explained by the larger heating rates through three body losses we observe at that field.

motion of the quadrupole mode can dissipate its energy on small scales directly. As a result, the requirement of a purely local interaction of length scales is not given and no turbulent cascade can form. This consideration is confirmed by measurements of equilibrium momentum distributions at different temperatures. By heating the fluid by just leaving it in the trap for some time before the TOF measurement, we are able to reproduce all of the different momentum distributions that we observe in the quadrupole mode also in equilibrium (see Figure 4.13 B).

In summary, we observe that the quadrupole mode always dissipates its energy by directly heating the gas. Thus it is not suited for the creation of turbulent motion even though it is, in contrast to the breathing mode, directly connected to a dissipative mechanism. We draw the conclusion that all the lowest order collective modes that we can excite in our harmonic trap are inapplicable to the task of creating turbulence. Nevertheless, we do not plan to abandon our search for turbulence in the two dimensional Fermi gas. The extension that will be added to our experiment, will hopefully allow us to observe turbulence in the near future.

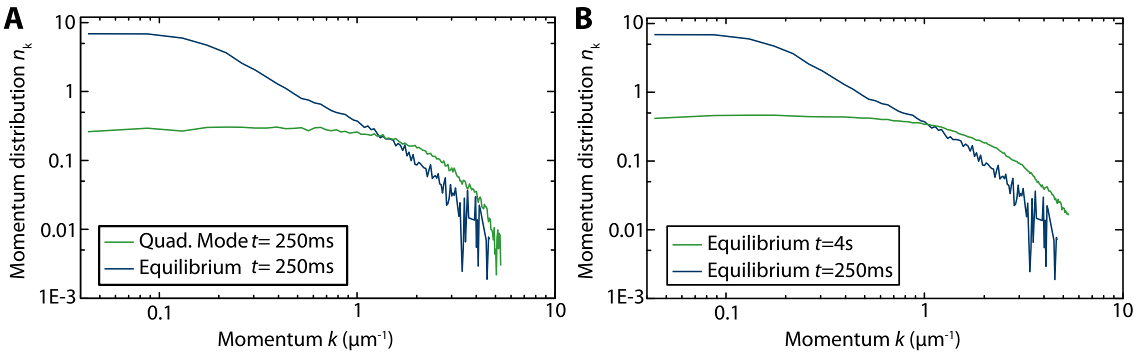

Figure 4.13: **A:** The decay of the quadrupole mode has a strong effect on the momentum distribution. It dissipates its energy through viscous flow which leads to a fast growth of the particle number at high momenta.
B: The same effect can be observed through background heating effects by leaving the atoms in the trap for a long time instead.

4.4.3 Discussion

As derived in section 2.6.4, in the framework of kinetic theory the problem of finding the dependence of the quadrupole frequency and damping rate on interactions is reduced to a computation of the scattering time τ. To this end Baur et al. [Bau13] take different levels of effects into account. The scattering time of gas in the classical limit is proportional to the particle density and is given by

$$\tau_{\mathrm{cl}} = \frac{R'(a_{2\mathrm{D}}, T)}{E_{\mathrm{F}}} = R(a_{2\mathrm{D}}, T)\frac{T}{N\omega_R^2} \tag{4.7}$$

in the harmonic trap, where R is some interaction and temperature dependent coefficient, N is the particle number and T the temperature of the gas. If we consider the case of a quantum degenerate Fermi gas additional effects come into play. Pauli blocking reduces the scattering rate significantly when the temperature is lowered. At the same time, medium effects like the presence of a pairing gap lead to an increase of the scattering rate. It has been found that both effects more or less cancel each other out even at very low temperatures T just above the superfluid transition [Rie08]. Nevertheless, Baur et al. [Bau13] included both effects in their numerical evaluation of the collision integral $I[f]$.

The comparison of this model to the experimental data of Vogt et al. [Vog12] shows a very good qualitative agreement of both the measured frequency ω_{Q} and the damping rate Γ_Q with the theoretical predictions. However, in this experiment they have not been able to observe frequencies in the hydrodynamic limit $\omega_Q = \sqrt{2}\omega_R$, and they have measured a significantly higher damping rate than what is expected in this regime. A significant theoretical effort has been made to explain this increased damping rate. Approches include a detailed study of medium effects [Ens12], a numerical solution of the Boltzmann equation [Wu12] or the inclusion of higher order moments and trap anharmonicity and anisotropy [Chi13]. However, no final picture to explain the increased damping rate could be obtained. Furthermore, due to experimental limitations for smaller magnetic fields, the theoretical expectations for the two dimensional Fermi gas have only been verified on the right hand side of the crossover for $\ln(k_\mathrm{F}a_\mathrm{2D}) > 0$.

We compare our results to the expected values obtained from the simple classical approach while taking a slightly reduced scattering rate through Pauli blocking into account. We got the theoretical results from a theory group we work together with. We observe an impressive agreement of the classical prediction with our measurements just above the superfluid transition at $T/T_\mathrm{F} \approx 0.2$. This applies also to the previously unexplored regime of $\ln(k_\mathrm{F}a_\mathrm{2D}) < 0$ and confirms that the classical model does indeed lead to an accurate description of collective modes even very far in the degenerate regime. In contrast to Vogt et al. [Vog12] we see no significant deviation of the damping rate Γ_Q. Therefore, we conclude that their measurement has to be explained either by systematic errors or by a temperature effect. Since the theoretical model already uses a classical picture, the latter seems unlikely.

The small deviations of our data points from the theoretical prediction can be explained by systematic effects. The errorbars in Figure 4.12 do solely contain the statistical errors of the sine fits. Systematic uncertainties in our temperature determination, for example, have a rather strong effect on the theoretically expected scattering rate. The small growth of the frequency towards the BEC regime could also be explained by the trap anisotropy that leads to a coupling to the breathing mode at $2\omega_\mathrm{R}$. This anisotropy does increase for lower values of $\ln(k_\mathrm{F}a_\mathrm{2D})$ as our measurements show. The significantly higher damping rate for our single data point at $\ln(k_\mathrm{F}a_\mathrm{2D}) = -7$ can be explained by the three-body losses we observe at that field.

In conclusion, we observe an almost perfect agreement with classical theory. This confirms that effects due to the quantum degeneracy do cancel each other out to the largest extend. In both the BEC and BCS limit we observe the transition away from the hydrodynamic regime at the predicted interaction strength. Additionally, our measurements show the characteristic asymmetry of these limits that is expected in the classical picture due to the higher boson density in the BEC limit.

4.4.4 Outlook

In this work we were able to show that classical kinetic theory is sufficient to describe the collective modes of a degenerate Fermi gas in two dimensions even on a quantitative level. However, apart from a single measurement of the single component Fermi gas, we have not been able to reach the collisionless limit due to experimental limitations. In line with the breathing mode we plan to extend our present dataset up to $\ln(k_\mathrm{F}a_\mathrm{2D}) \approx 8$ by switchting to a $|1\rangle$-$|3\rangle$ mixture in the future. Furthermore, by an additional measurement of the temperature dependence of the damping rate we could extract the dependence of the viscosity of the latter. The same measurement was already performed by Vogt et al. [Vog12] at higher temperatures and we could check to what extend we are able to reproduce their findings.

4.5 Additional Observations

4.5.1 Short TOF Measurements

In chapter 2 we presented different observables to reveal the presence of a turbulent state. Up to this point we have only discussed one of them, namely the momentum distribution of the gas. Since our trap is nearly isotropic we are not able to observe an inversion of the aspect ratio of the superfluid cloud when we let our gas expand from the trap. Consequentially, we are not able to distinguish a possible expansion with constant aspect ratio, as expected for a turbulence cloud, from the gas in equilibrium either. We can, however, try to observe phase defects directly by letting the gas expand for a very short time before imaging.

To this end we apply the same technique that was already described in reference [Wen13]. In contrast to our usual TOF imaging sequence, we gradually ramp down the two dimensional confinement on a time scale of 100 to 200 μs and take an image after about 4 ms. This prevents the cloud from expanding too quickly in z-direction and becoming too dilute as a result. Single images of the atom cloud we obtained in this way are shown in Figure 4.14.

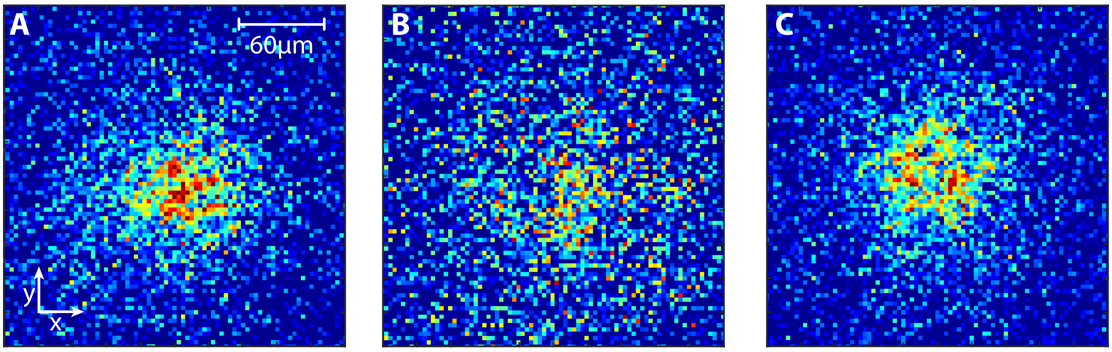

Figure 4.14: Single, i.e. non averaged, images of the atom cloud after a short TOF. Even in equilibrium, at the coldest temperatures we can reach, we observe large density fluctuations (**A**). The damped quadrupole transfers a large amount of heat to the cloud. Thus we cannot observe any phase coherence in this case (**B**). As expected, the breathing mode shows the same density fluctuations we see in equilibrium (**C**).

All our measurement below the superfluid transition show large density fluctuations in the cloud. These originate from phase defects and become visible through interference of the atom cloud with itself. These phase defects are, however, not effects of turbulence but can be observed even in an equilibrium state. Their origin is the inherent property that phase fluctuations are increased in the two dimensional superfluid as discussed in context with the BKT theory in chapter 3. We are not able to observe single vortices in either the quadrupole or breathing mode on the level of our current imaging resolution.

4.5.2 Large Amplitude Breathing Mode

One feature of the breathing mode oscillation we have observed recently in our experiment is a doubling of its oscillation frequency in momentum space. We observe this effect only at very large amplitudes after exciting the breathing mode by a modulation of the magnetic offset field B. Surprisingly, the frequency doubling occurs only in the superfluid phase and it is only visible in momentum space. The evaluation of insitu images shows an oscillation with a small asymmetry between the rising and falling edge of the sine like curve, but with the expected frequency $\omega_{\mathrm{B}} = 2\omega_{\mathrm{R}}$ (see Figure 4.15).

As we observe this effect only in the superfluid phase, our initial approach was to check whether one can already understand it in the framework of Bose-Einstein

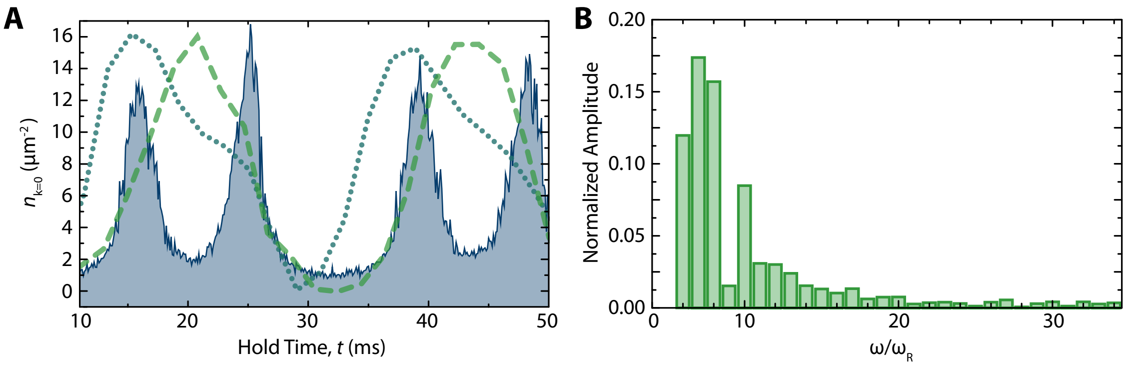

Figure 4.15: **A:** For small amplitudes we observe an oscillation with the expected frequency $\omega_B = 2\omega_R$ in momentum space (green dashed line). If the amplitude is increased, the peaks of the oscillation become sharper and split such that the oscillation frequency is effectively doubled (blue line). The plot shows the height of the condensate peak in momentum space or, equivalently, the density of atoms with $k = 0$. In the oscillations of the insitu cloud width we do not observe the same frequency doubling but we measure a significant deviation of the oscillation from a sine function (dotted line). **B:** The Fourier spectrum of the sharp peaks shows significant contributions from very high frequencies up to $\approx 20\omega/\omega_R$.

condensation. To this end, we use a time-dependent variational ansatz for solving the Gross–Pitaevskii equation for a $T = 0$ condensate that is confined by a harmonic potential. Following Perez-Garcia et al. [Per96], the proper form of the trial wavefunction for our condensate is given by

$$\Psi(x, y, z, t) = A(t) \prod_{\eta=x,y,z} \exp\left[\frac{\eta - \eta_0(t)}{2w_\eta^2} + i\eta\alpha_\eta(t) + i\eta^2\beta_\eta(t)\right]. \tag{4.8}$$

This function describes a Gaussian distribution with time dependent center (x_0, y_0, z_0), amplitude A, width w_η, slope α_η and curvature β_η^{-2}. By inserting this equation into the Lagrangian corresponding to the Gross–Pitaevskii equation and minimizing the action with respect to each of these parameters one arrives at a coupled non-linear evolution equation for each parameter [Per96]. We got the numerical solutions of these equations of motion for initial conditions close to our experiment from a theory group we work with. The preliminary results for the breathing mode are shown in Figure 4.16.

We conclude that we are able to explain the effect we observe, at least qualitatively,

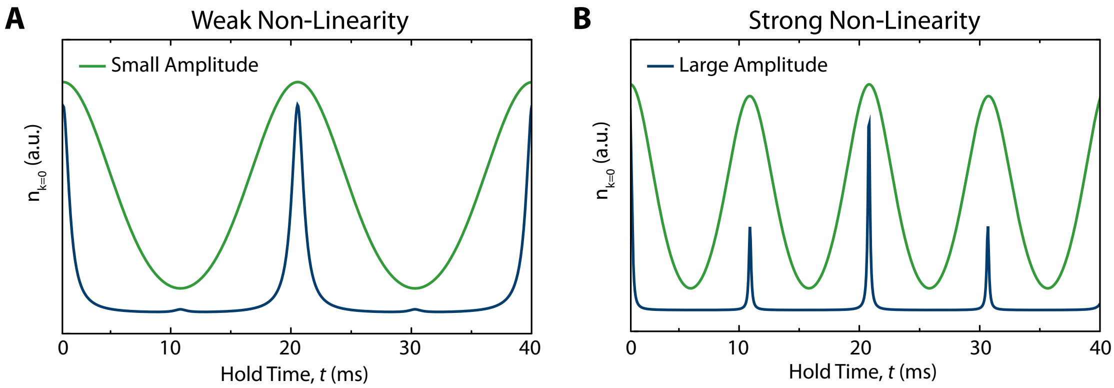

Figure 4.16: **A:** For a weak non-linearity in the Gross–Pitaevskii equation we observe the expected sinusoidal oscillation in momentum space with $\omega = 2\omega_R$ for small amplitudes (green line). If the amplitude is increased the peaks become sharper due to the non-linearity in the equations of motion and an additional small second peak becomes visible (blue line). **B:** For strong non-linearities we observe frequency doubling to $\omega = 4\omega_R$ even at low amplitudes (green) and the same behaviour but with sharper peaks at larger amplitudes (blue). The y-axes of the plots are rescaled and shifted in order to show them in a single figure.

by this bosonic theory at zero temperature. In the regime of large amplitudes and strong non-linearity, or equivalently large interactions, we find the same frequency doubling and sharpening of the peaks we observe in our Fermi gas. Furthermore, the variational solution leads to the following prediction for the relationship between the condensate momentum peak $n_{k=0}$ and its insitu width w

$$n_{k=0} = \frac{w}{\sqrt{\dot{w}^2 w^2 + 1}}. \tag{4.9}$$

The dependence of $n_{k=0}$ on the derivative of w explains why even a small deviation from a sinusoidal oscillation of the insitu width can lead to strong effect in momentum space, in line with our observations in Figure 4.15.

To summarize, our first theoretical attempt to understand the breathing mode at high amplitudes does already explain most of the effects we observe. Since these are already covered by a bosonic ansatz, the fermionic nature of our lithium atoms does not seem to play a major role here. It is not clear yet why we observe the effect of strong non-linearity only at large amplitudes. To solve this question we want to carry out further measurements with weaker interactions in the near future. In this way we should be able to observe a sharpening of the peaks in momentum space without frequency doubling as predicted by our theory (see Figure 4.16 A). This exceptional behaviour of the breathing mode has not been mentioned in literature at all by now. This is probably due to the fact that it occurs only for very large amplitudes, opposite to the regime where the breathing mode is most frequently studied.

5 Outlook

In this chapter we will give an overview over the reconstruction of the experimental setup that was planned, built and tested during the work on this thesis. The add-on has been designed around three main components: a spatial light modulator (SLM) to tailor arbitrary and time dependent potentials for our atoms, a high resolution objective to both manipulate and probe the cloud on length scales down to one micrometer and an extremely sensitive electron multiplying camera (EMCCD) with single photon counting capability. Equipped with the new objective, the camera will allow us to get single atom resolution even when scattering only very few photons per atom.

Together, these components provide us with new tools to significantly extend our experimental capabilities. We will discuss some of their applications at the end of this chapter, among them our plan to assemble many body systems on lattices from small building blocks at extremely low entropy. Single atom resolution and time of flight measurements enable us to measure arbitrary correlation functions in these systems at very low temperature. Finally, we will also explore how these new capabilities can help us to create and detect turbulent states in the two dimensional Fermi gas.

5.1 Spatial Light Modulator

In section 3.2.3 we explained how detuned laser beams can be used to create potentials for neutral atoms that are proportional to the light intensity. It follows that if one is able to shape some arbitrary light intensity distribution, that same distribution forms a potential landscape for the atoms. Many experimentalists have made use of this fact and built various elaborate laser setups like, for example, our two dimensional confinement ODT. Usually, large efforts have to be made to find and set up the correct optical alignment to achieve a desired potential shape.

An idea circulating in the cold atom community for several years now, is to shape the intensity distribution of the light into arbitrary potential by using adaptive optics that allow to create many different potentials within a single optical setup. Spatial light modulators (SLMs) based on liquid crystals and digital micromirror devices (DMDs) in particular have been chosen and used for this purpose. We have decided to implement a phase modulating SLM in our setup for arbitrary potential creation. SLMs in contrast to DMDs switch between two potentials in a continuous way naturally and are thus more suited for the creation of time dependent potentials.

In this section we will provide some background knowledge about potential creation with SLMs and we will present the optical setup that we designed for this purpose. A detailed discussion of spatial light modulators in the context of cold atom experiments is, for example, found in reference [Bij13].

5.1.1 Phase Modulation

A phase modulating SLM is able to imprint an arbitrary phase pattern on the wave front of an incident light field. This is achieved by applying an electric field to cells that contain parallelly aligned liquid crystals (PAN-LC) such that the directions of the birefringent molecules change (see Figure 5.1 A and B). In this way our SLM is able to set the phase of the light field from 0 to 2π in 256 steps independently on an array of 800×600 pixels.

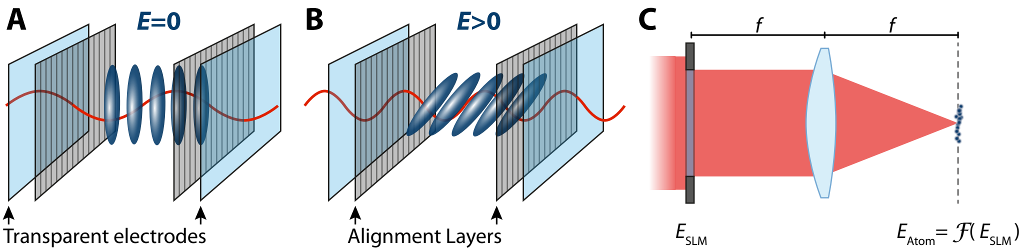

Figure 5.1: Working principle of an SLM. **A:** If no electric field is applied, the rod-like liquid crystal molecules align to the alignment layers and the light beam passes unaltered. **B:** If an electric field is applied, the molecules are polarized and their direction changes. This slows the passing light down and its phase gets shifted compared to the previous case. **C:** In order to use phase modulation to create arbitrary intensity distributions one has to project the Fourier field of the SLM plane onto the atoms. According to Fourier optics this can be achieved by arranging a single lens in a $2f$-setup.

In order to use the phase modulation of the electric light field in the SLM plane

E_{SLM} to create arbitrary intensity patterns in the atom plane one has to resort to Fourier optics. A lens at the focal distance of the SLM will produce a light field that is the Fourier transform of E_{SLM} at its focus (see Figure 5.1 C). Since the intensity distribution after the Fourier transformation is dominated by the wave front of the incident light field this allows us to shape arbitrary two dimensional potentials in the focal plane of the lens. The confinement in the third direction is provided by the same disc shaped ODT we introduced in chapter 3.

5.1.2 Phase Retrieval

Finding the correct phase pattern to obtain a desired trapping configuration, i.e. the process of so-called *phase-retrieval*, is in general an unsolved problem. However there exist several numerical algorithms that are able to closly approximate some target. We mainly rely on the so called mixed-region amplitude freedom iterative Fourier transform algorithm (MRAF-IFTA) [Pas08] and a conjugate gradient descent (CGD) search method [Har14]. We recently implemented graphics card acceleration for both of these algorithms. The latter allows us to stabilize relative intensities of the SLM potentials on time-scales up to the refresh rate of 120 Hz of the SLM in addition to a total intensity stabilisation achieved with acousto optical modulators.

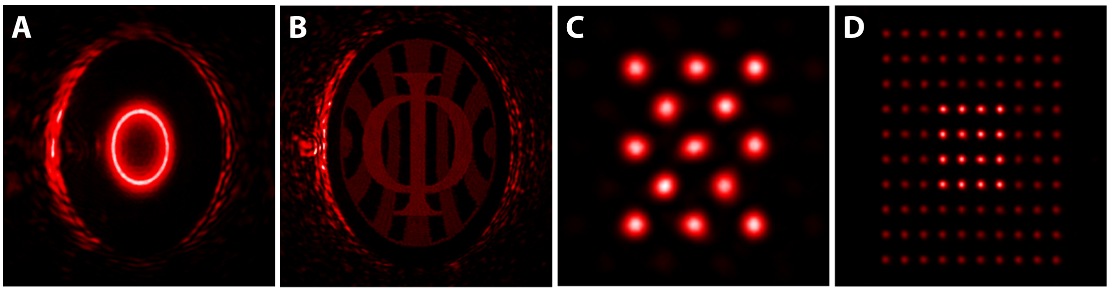

Figure 5.2: Camera images of optical potentials created by the SLM. When using the MRAF algorithm, continuous traps (**A**,**B**) have a lower light utilization efficiency of around 40 % because a lot of light is distributed in so-called *noise regions* on the outside of the trap. When using the gradient minimization approach instead, or in the case of discrete configurations (**C**,**D**), we reach efficiencies up to 90%.

Some examples of created optical potentials are shown in Figure 5.2. In order to shape high quality potentials it is absolutely essential to use a camera feedback loop to factor in optical aberrations in the real-world setup [Bru15]. One outstanding ability of the SLM is that it can be used to both detect and correct optical aberrations of the wavefront [Bij13].

5.1.3 Optical Setup

We built the optical setup for the SLM that is shown in Figure 5.3 with several design goals in mind. First of all, the efficiency of the SLM is highly dependent on the polarization of the incident light. Therefore, we use a polarising beam splitter (PBS) together with a $\lambda/4$-plate to obtain a defined polarization behind the fiber out-coupler (A). Next comes a telescope (f_1 and f_2) to increase the beam diameter, such that we illuminate the whole chip of the SLM. It is important to illuminate the SLM under an angle of less then 20° since its light utilization efficiency severely decreases otherwise.

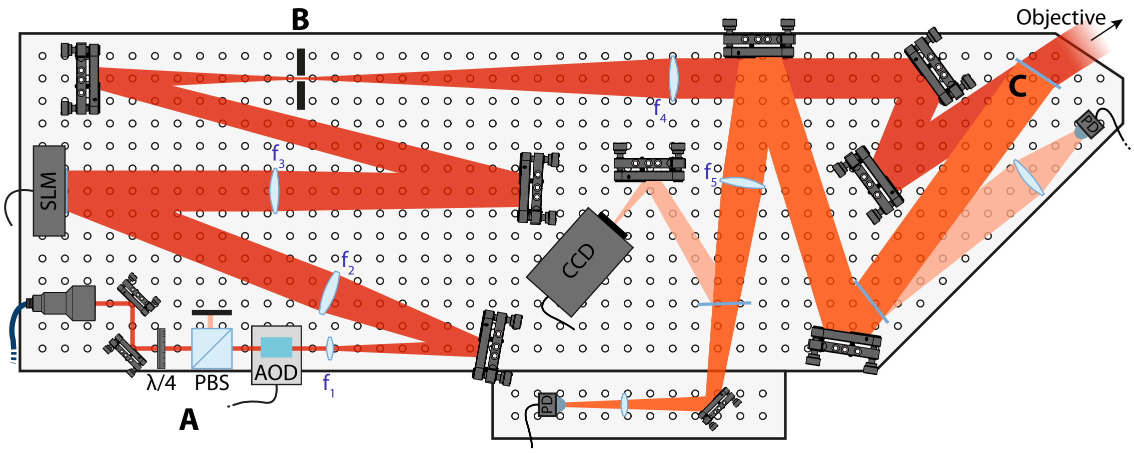

Figure 5.3: Sketch of the optical setup that was build for the SLM.

The final Fourier image of the light in the atom plane is produced by a high resolution objective which is not shown in this figure. The most important goal was to make use of the full aperture of this objective to reach the highest possible resolution. In order to achieve this gaol we had to replace the simple 2f-setup discussed in the previous section by a 6f-setup. To this end we added a telescope between SLM and objective that magnifies the beam to the size of the objective. This telescope is composed of the lenses f_4 and f_3 in the figure. When choosing these lenses one has to keep in mind that the total distance of the SLM to the atom plane d has to be approximately given by $d = 2f_3 + 2f_4 + 2f_{\mathrm{obj}}$. Otherwise the approximations of Fourier optics break down.

One major advantage of the 6f-setup is that it allows us to remove unwanted light in the first Fourier plane at position (B), using an aperture. Unmodulated stray light is for example always produced by the SLM itself due to its limited efficiency.

In order to regulate the total laser intensity and to be able to implement a camera feedback loop we additionally added a beam sampler at position (C) directly before the beam enters the objective. After being partially reflected by this splitter, the beam is divided again until it is finally incident on two photodiodes and a camera. Two separate photodiodes are necessary because we want to work in very different optical power regimes with the SLM. If we produce very small structures small laser powers ($\ll 1\,\mathrm{mW}$) are sufficient and we need a larger fraction of light on the photodiode for power regulation. If we want to produce large lattices or continuous traps more power, i.e. up to several watts may be required and the second photodiode has to be used for regulation. The camera is used both for diagnostics and feedback purposes. Here, the lens f_5 that images the light on the camera has to be chosen such that a sufficient magnification factor with respect to the objective is given (here: $f_5/f_{\mathrm{obj}} \approx 20$).

The last modification we added to our setup is an acousto optical deflector (AOD) at position (A). The AOD allows us to split the beam into several parts with different outgoing angles that sequentially fall on the SLM. This produces multiple copies of the same light distribution in the atom plane which are shifted in position. We could, for example, split a usual regular lattice into a super lattice. The advantage of using the AOD to additionally modify potentials is that it is much more straightforward to implement time dependent potentials and that the AOD is much faster than the SLM. The latter is always limited by its refresh rate of 120 Hz.

This optical setup is already built and aligned and we were able to produce high quality trapping potentials on the diagnostics camera. We were also able to create a second copy of the trapping potential with the AOD, where we could control both the relative intensity and position of the two copies as a function of time. Summarized, the SLM is fully operational and can be added into the experimental setup soon. At a later stage we plan to add an additional power regulation circuit to control the relative power of the different beams that the AOD creates.

5.2 High Resolution Objective

The high resolution objective has been designed by our group in order to achieve the best possible resolution for the constraints that were given by our experimental setup [Ser11a]. First, since the objective had to be placed outside the vacuum chamber a rather large focal length of $f_{\text{obj}} = 20.3mm$ was required and the effect of the vacuum window on the light path had to be taken into account. Furthermore, the objective had to be diffraction limited at both wavelengths of $\lambda = 1064\,\text{nm}$ and $\lambda = 671\,\text{nm}$. The former is used for the ODTs that are created by the SLM while the latter is used for imaging of the ^{6}Li atoms.

The objective that has been developed and extensively tested in our group fulfils all of these requirements with a theoretical numerical aperture of $NA = 0.6$. A simulation of the light path has been used in order to correct for any effect of the vacuum window. As a consequence of this correction a precise alignment of the objective with respect to the viewport proved to be essential. Additionally, the components have been chosen such that chromatic aberrations are minimized and the resolution limit is reached for both wavelengths. The objective has a field of view of $200\,\mu$m with a resolution of $1.08\,\mu$m at $\lambda = 1064\,\text{nm}$ and $0.68\,\mu$m at $\lambda = 671\,\text{nm}$.

5.2.1 Optical Setup

The objective is aligned along the z-axis in our experiment since we want to image in the plane of our two dimensional confinement. This immediately complicates the optical setup, since all the beams passing through the viewport on top of the vacuum chamber have to pass the objective in addition. A complete list of all the implemented beams is given in the following. The colors listed in the brackets are the colors used in Figure 5.4 for the respective beams.

SLM-Beam $(1064\,\text{nm}, red)$

The objective has to image the light coming from the SLM onto the atoms. It acts as the final lens of the $6f$-setup as discussed previously.

Alignment beam $(531\,\text{nm}, blue)$

We implemented an auxiliary alignment beam that is reflected by the vacuum window. This allows us to precisely align the objective to the window. We have seen that their relative angle has to be accurate to a few milliradians in order to achieve the best resolution.

Fluorescence Light (671 nm, *green*)
The light that is emitted by the atoms through spontaneous emission is collimated by the objective. We set up a path for this light to the camera where it is imaged.

Down-Top Absorption (671 nm, *green*)
We want to produce absorption images with the objective as well. Therefore, we added resonant collimated laser beam that is coming from below the chamber and passing trough the objective. Sequentially this beam will take the same route to the camera as the fluorescence light.

Top-Down Absorption (671 nm, *green*)
In our current experiment we use a low resolution absorption imaging path below the chamber which yields images with a larger field of view than the high resolution objective. To keep this imaging path intact, a second absorption beam coming from a source above is required. The objective then collimates the beam in the atom plane.

MOT-Beams (671 nm, *green*)
Our MOT requires trapping beams coming from six different directions. Currently we create the MOT by sending in a beam from above onto a mirror below the chamber where it gets reflected. This setup will be inverted such that the MOT beam will start below the chamber, pass the objective and get reflected sequentially.

Our design of the setup containing all of these beams is presented in Figure 5.4. The complete setup is aligned vertically on breadboards above and below the vacuum chamber.

Starting at the top (A), we implemented a narrow green alignment laser. Its beam is split by a 50 : 50-Beamsplitter such that one path is focused on a camera while the second beam travels through the objective. Some part of this light is reflected by the vacuum window and comes back to the camera. By comparing the position of this beam on the camera with a reflection from the objective we are able to align the objective to the window with an accuracy much better than one millirad.

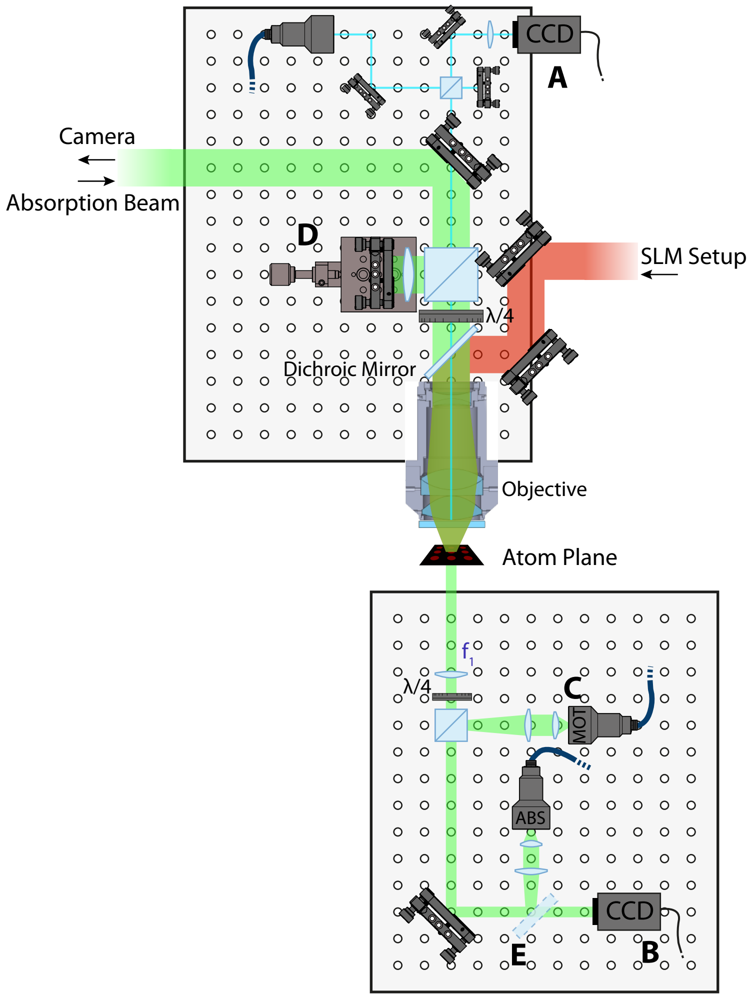

Figure 5.4: Beam paths around the high resolution objective.

The light coming from the SLM (red) is responsible for the quality of our potentials. It is highly sensitive to optical aberrations and in an effort to minimize the latter we inserted the SLM light as close to the objective as possible. The light is coming directly from the SLM board shown in Figure 5.3. To combine it with the 671 nm imaging beams we use a dichroic mirror that only reflects infra-red light.

On the lower breadboard, the lens f_1 is used for absorption imaging in the current experimental setup. It is aligned to the atom plane and focuses the absorption beam coming from above onto a camera below the setup (B). We added a PBS to this beam path such that the MOT-light can be inserted below the chamber (C). This MOT light is collimated by the same lens f_1 used for imaging and passes through the objective sequentially. Having passed the objective, the MOT and imaging light are separated by a second PBS. A mirror reflects the MOT beam and a lens ensures that the light is collimated when passing the atoms a second time (D).

In order to switch between absorption imaging below the chamber with low resolution and a large field of view and absorption imaging above the chamber with high resolution and small field of view we inserted a flippable mirror at position E. When the mirror is flipped out we get back to the exact imaging setup we use currently. When the mirror is flipped in, a resonant absorption beam shines through the chamber and onto the camera at the top. We are going to use a motorized mirror to automate this switching process. It should be noted that switching is only required for absorption imaging, while fluorescence images can always be taken with both cameras simultaneously.

In conclusion, we designed an optical setup that adds the technology of high-resolution and single atom imaging to our current imaging procedures while not giving up any experimental capabilities we have at the moment. These will become very helpful when we align all the new optical components, since we can take images of the atom cloud with our old setup at any stage of the modification process. Furthermore, the setup does not depend on any moveable parts, with the exception of one mirror that has to be switched only rarely. This makes the setup very stable and fail-safe once it is properly aligned. The setup even allows us to take fluorescence images in a MOT after the complete experimental cycle. This procedure can be used to measure the atom number very accurately [Ser11b].

5.3 Electron Multiplying Camera

The last device that we will add to the experiment is the EMCDD. An EMCCD camera consists of an ordinary CCD chip with an additional gain register placed between the shift register and the output amplifier. This register amplifies primary electrons that were produced by photons hitting the chip in an avalanche method similar to that of electron multiplier tubes. As a result EMCCD's are able to detect single photons with very high efficiencies up to 90%. The only limitations are so-called *clock induced charges* (CICs). CIC are background electrons that are produced by the shifting procedure of the CCD chip and cannot be differentiated from real photons. We measured both the CIC count as well as photon detection efficiency of our new HNü 512 camera from NüVü as a function of gain. We found a possible sweet spot for operating the EMCCD (see Figure 5.5 A). At this point we measure a detection efficiency of 78 % while maintaining a low CIC count of only 0.002 per pixel. Using this configuration we expect to at least match if not improve what is currently possible with the other EMCCD from Andor in our second experiment (see Figure 5.5 B). In this experiment atom detection probabilities of above 99 % are achieved with a total of only 300 scattered photons per atom.

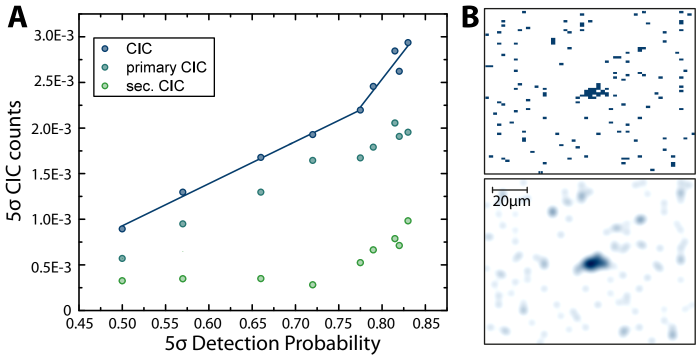

Figure 5.5: **A:** Probability of a CIC per pixel as function of the photon detection probability of the camera. The detection probability increases monotonously with the voltage of the gain register. The dark blue spots show the total CIC number, primary and secondary CICs are created on the chip and in the gain register respectively. **B:** Image of a single atom that was taken with a similar EMCCD in the second experiment of our group. As little as 15 detected photons are enough to clearly identify a single atom. The upper image shows the raw data while the lower image is low-pass filtered. Adapted from [Ber17].

5.3.1 Optical Setup

The camera is mounted on a third horizontally aligned imaging breadboard (see Figure 5.6 A). The goal of the imaging setup is to make as much use as possible of the high camera sensitivity. Therefore, we tried to minimize the amount of components that can cause photon losses on the way to the camera. In the beam path we use 3 mirrors, one high quality PBS, one lens and one beam sampler. This should lead to a sufficient collection rate of around 90 % of the photons that leave the objective.

In order to always work in the optimal regime of the EMCCD, where less than one photon is detected per pixel, we use two flippable lenses in the beam path (B). This allows us to adjust the magnification quickly. In case we want to work at very different magnifications at a later stage we can also move the whole camera breadboard vertically to adjust its distance from the objective.

The second beam that we placed on the same breadboard is the top down imaging beam (C). In its current version the optical setup produces a resonant collimated beam in the atom plane that is used for absorption imaging on the camera below the chamber. Later we plan to add a flippable lens at position D and possibly a DMD or an AOD at position E or F. This will give us the ability to send focused resonant light into the atom plane at a precisely controlled position. As a result, we would, for example, be able to remove atoms of a chosen spin state at a single site of a lattice we created with the SLM and create arbitrarily doped systems.

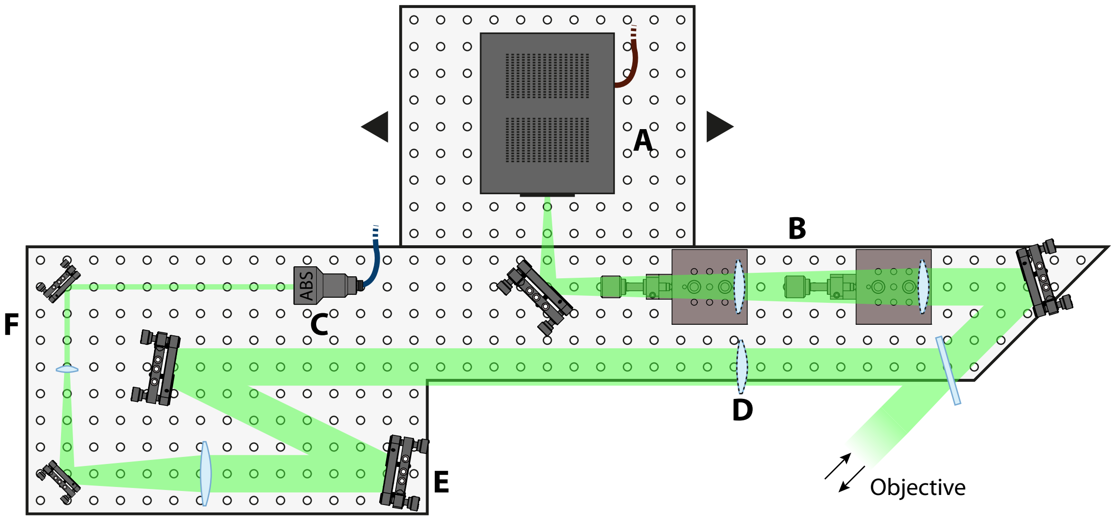

Figure 5.6: Optical setup for imaging on the EMCCD.

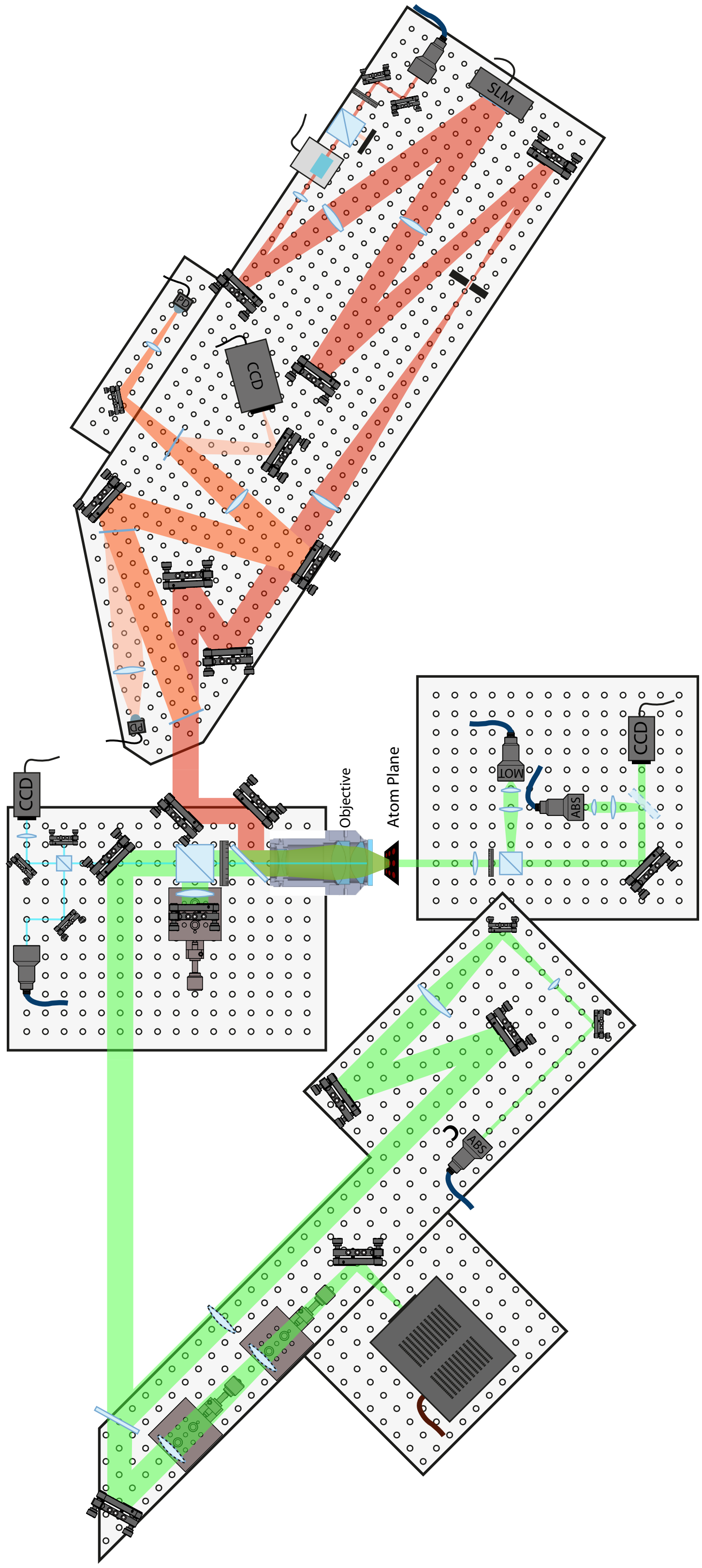

Figure 5.7: The complete optical setup of our extension to the experiment.

5.3.2 Complete Setup

Figure 5.7 shows the complete add-on to the experiment. The two breadboards in the center are mounted vertically, while the SLM and Camera boards are kept horizontally. The latter will be placed above the current experimental setup on large steel posts that are already visible in Figure 3.6 B. The upgrade of the experiment will be carried out in an incremental manner, such that we can verify the functionality of the experiment after each iteration. Along with the optical setups also new software has been developed. The modular program has been written in LabVIEW and in an object oriented style and allows to control both the SLM and multiple cameras.

5.4 Quantum State Assembler

The vision of a *Quantum State Assembler* (QSTA) came up after recent breakthroughs in preparing and detecting few fermion systems in the second, few fermion experiment of our group. In this machine we are able to prepare two fermions in a desired state of a double well with fidelities above 90 % [Mur15a]. To this end, the double well potential is created and manipulated by placing an acousto optical modulator in a red-detuned beam that is sequentially focused onto the atoms by the same high-resolution objective that we will add to our experiment. The quantum state of the system can be extracted by measuring the correlations between the two atoms. This is achieved by a TOF measurement where the positions of both atoms are detected in free space after switching off all confinements [Ber17].

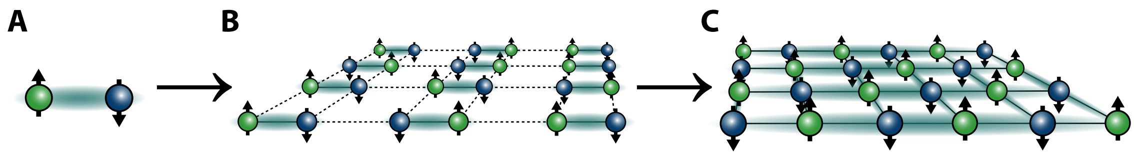

Figure 5.8: The idea of the QSTA is based on the ability to deterministically prepare two atom in a double well (**A**). In the first step many building blocks are prepared separately (**B**). Sequentially a many-body system at very low entropy is created by merging these building blocks adiabatically (**C**).

The underlying idea of the QSTA is to extend these abilities to larger systems which means that in contrast to the most common procedure, a many body potential is not loaded directly from a bulk gas but assembled from many small building blocks (see Figure 5.8). The latter are preprepared independently in advance. The simple building block of a double well is already enough to create many different interesting many body systems like chains, ladders and hexagonal or regular lattices (see Figure 5.9).

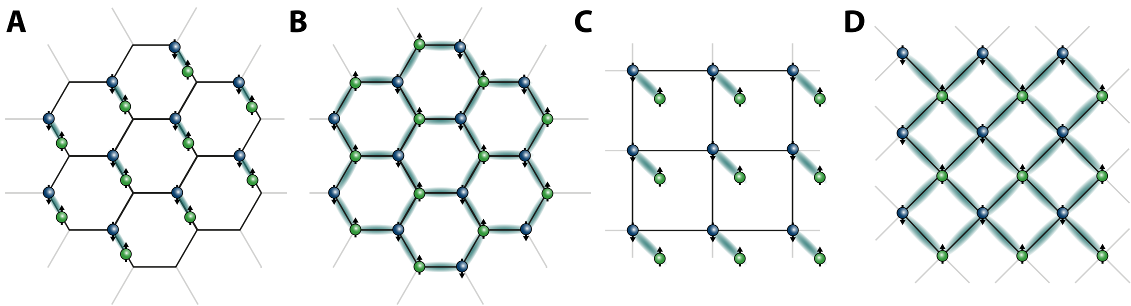

Figure 5.9: Different lattice geometries that can be created from double wells. First the atoms have to placed in some configuration such that tunnelling between different double wells is suppressed (**A**, **C**). In the next step the AOD is used to adjust the position of one of the two wells slightly and to connect the small blocks to a large many-body system (**B**, **D**).

The quantum state of many separated blocks is not necessarily connected adiabatically to the ground state of the many-body system. Only if this condition holds and there is, in addition, a gap between the ground and excited states that is large enough, it is possible to assemble many-body systems at very low entropy. Otherwise excitations are produced at arbitrarily slow merging rates. Optimizing trapping geometries and finding the best merging procedures will be the first challenges we have to face with the QSTA. An analytical study of four atoms in four wells was performed in our group, confirming that the ground state of this system is in fact adiabatically connected to the ground state of two double wells. Thus this system provides a basis from which we can test and expand the assembly process.

To realize this vision of a QSTA in our experiment we tried to stay as close as possible to the original few fermion setup discussed above, while adding the required tools for multiplying and assembling building blocks at the same time. To this end we use the same combination of an AOD and an objective to create the double wells (see Figure 5.7).

The AOD provides us with the technology to directly control the position and depth of each of the two created wells via regulated radio frequency signals. The parallelization of the deterministic preparation will be achieved using our SLM which is able to create exact copies of the double well at arbitrary positions in the atom plane (see Figure 5.9). We plan to realize the dynamic merging process using the AOD, since it is not limited by refresh rates, and time dependent potentials are readily implemented using radio frequency ramps.

To detect the final quantum state of our system a whole list of techniques is at our disposal. As discussed before, all of these rely on either absorption or fluorescence imaging of the atoms. Our high resolution objective allows us to image the system in the merged many-body state directly, after separating the double well state suddenly or after separating the double wells adiabatically. The latter can be used to test the adiabatic of the merging process.

To get access to correlation functions and the momentum distribution of our quantum systems we want to apply the same TOF imaging procedure that has been developed in the second experiment of our group. This technique relies on the detection of two atoms during TOF with a very small amount of scattered photons. By increasing the imaged region of interest, this procedure is immediately extendable to larger atom numbers. By letting our cloud expand from the lattice into our two dimensional confinement ODT we will be able to determine the momentum of every single atom of the systems of possibly up to hundreds of atoms. Together with *two state imaging* this enables us to extract arbitrary momentum correlations.

There is a whole landscape of systems where the QSTA could lead to significant improvement in our understanding of strongly correlated fermion systems. Examples include the Fermi Hubbard model on various lattice geometries, for example graphene like hexagonal systems or spin ladders. In all of these systems the QSTA naturally allows us to study the transition from few to many body physics. Whether the assembly can be executed successfully relies on very precise control and noise regulation of all the devices that are involved. These are the requirements to be fulfilled to reach many-body states at very low entropy. We expect that it will take us a considerable amount of time to get all devices under control well enough to work with real atoms. In the meantime, quantum turbulence, being a lot less susceptible to imperfect and noisy potentials, could allow us to acquire a large amount of the necessary capabilities for the QSTA. As already discussed in detail, it is an area that is more or less completely unexplored for the case of fermionic cold atoms systems.

5.5 Applications for Quantum Turbulence

The essential requirement for the excitation of turbulent cold gases is the creation of a time dependent Hamiltonian that takes the system out of equilibrium. In our current setup we can only vary the overall potential depth and the magnetic offset field to this end. Our add-on introduces both the SLM and the AOD as additional tools to create time dependent potentials. Different approaches for the creation of turbulence become available consequent, enabling us to implement most if not all of the excitation schemes discussed in section 2.4.1.

Using the AOD alone, we can sweep potential wells of the size of our resolution limit of $1\,um$ along straight lines through our cloud at arbitrary velocities. This excites the superfluid on rather small length scales and is therefore most likely to excite ultraquantum turbulence. The SLM can be used to rotate the cloud on large length scales, for example, with a paddle-like potential. In contrast to the AOD the SLM is not able however to reach arbitrary rotation speed since its frame rate is limited. If we want to use at least 30 distinct phase patterns per rotation we estimate that this excites approximately 25 vortices in our superfluid. This is well above the number of vortices that have been observed in the turbulent BEC experiments we discussed in chapter 2.

Finally, we could also combine SLM and AOD to excite the cloud at arbitrary length scales. The most promising method is to first create some potential with a characteristic length scale, for example a lattice, with the SLM. The AOD is then able to sweep this potential through the two dimensional cloud at arbitrary speeds and to excite turbulence at a well defined length scale.

In addition to the excitation procedures, the add-on also provides us with new technologies to detect the presence of turbulence. Our current imaging resolution improves by a factor of four from $\sim 4\,\mu$m to $\sim 1\,\mu$m. This allows us to characterize phase defects in our cloud after short TOF much more precisely. We estimated that the healing length ξ of our system is on the order of 0.1 to $1\,\mu$m, depending on the interaction strength, which is close to the resolution of our new objective. As a result the observation of single vortices after very short expansion becomes possible. By creating anisotropic potentials using the SLM and studying TOF measurements afterwards we can also access an expansion with constant aspect ratio as additional observable for turbulence.

In summary, we believe that the add-on provides us with all the required technologies to make an observation of turbulence in our cloud feasible in the near future. On a longer term we plan to study turbulence in potentials different from our harmonic confinement as well, for example in boxes and ring traps or between two connected reservoirs.

5.6 Conclusion

In this thesis we have studied collective modes of a two dimensional Fermi gas in a harmonic confinement from the perspective of turbulence. To this end we have measured the effect of these modes on the momentum distributions of the gas. We have seen that all of the lowest order collective modes are not applicable for the excitation of turbulence. Nevertheless, we plan to further pursue the goal of exciting turbulence in our cloud after the experimental add-on we set up is built in.

In addition to the momentum space measurements we have also repeated the insitu study of the dependence of the breathing and the quadrupole mode on the inter-particle interactions that were initally reported by Vogt et al. [Vog12]. We were able to reproduce their results in general and could extend their data in the low temperature regime.

Considering the breathing mode, we see strong evidence for the presence of a previously unobserved quantum anomaly that has been predicted for the two dimensional Fermi gas. We plan to increase our confidence in this observation by cautiously characterising all systematic errors in our system.

Our data of the quadrupole mode extends previous measurements to both the low temperature limit just above the superfluid transition and to the BEC regime. In contrast to reference [Bau13], we measure no significantly increased damping rate and we are able reach the hydrodynamic limit. Our data shows excellent agreement with the predictions from classical kinetic theory, also in the previously unexplored regime where $\ln(k_{\mathrm{F}} a_{2\mathrm{D}}) < 0$.

In measurements of the momentum distribution of the breathing mode we found a frequency doubling effect that has not been discussed in literature so far. We explain this observation in the picture of an oscillating condensate with strong non-linearities in its equations of motion. We obtained these equations through a variational ansatz for the solution of the Gross–Pitaevskii equation.

We want to extend our dataset on collective modes with measurements in the $|1\rangle$-$|3\rangle$ mixture in the future. In addition, the SLM will enable us to study arbitrary higher order collective modes by redistribution of the initial atom density in our two dimensional confinement before it is switched off. This could also be used to take measurements of the quadrupole oscillation at lower amplitudes.

At the moment we also explore completely different ideas apart from quantum state assembly and turbulence we can use our experiment for after it has been reconstructed. We find possible applications for the SLM in many fields, among them many-body localization or measurements of transport properties using connected reservoirs. Many of these require very precisely controlled potentials, just like the QSTA. Turbulence represents a field with many open questions where small deviations in the potentials used for excitation play no major role. Thus it enables us to become familiar with our new experimental setup while studying unexplored regimes in physics at the same time. In the long run we will then try to achieve the milestone of realizing the quantum state assembler.

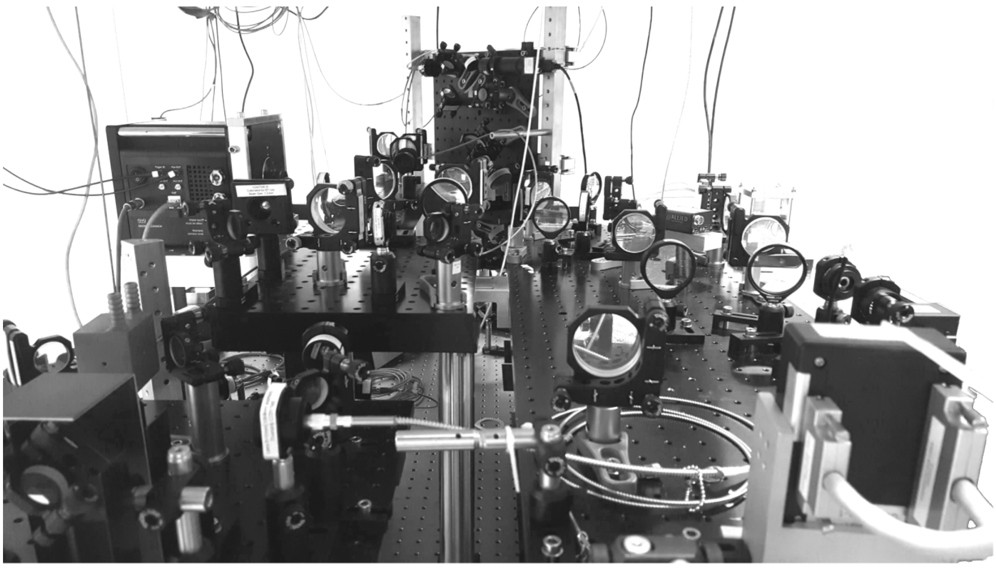

Figure 5.10: Picture of the complete add-on.

A Appendix

A.1 List of Figures

B Bibliography

[Ada12] Allan Adams et al. "Strongly correlated quantum fluids: ultracold quantum gases, quantum chromodynamic plasmas and holographic duality". In: *New Journal of Physics* 14.11 (Nov. 2012), p. 115009. DOI: 10.1088/1367-2630/14/11/115009.

[All14] AJ Allen et al. "Quantum turbulence in atomic Bose-Einstein condensates". In: *Journal of Physics: Conference Series*. Vol. 544. 1. IOP Publishing. 2014, p. 012023.

[All38] JF Allen and AD Misener. "Flow of liquid helium II". In: *Nature* 141.3558 (1938), p. 75.

[And12] Jason Laurie Andrew W. Baggaley and Carlo F. Barenghi. "Vortex-Density Fluctuations, Energy Spectra, and Vortical Regions in Superfluid Turbulence". In: *Phys. Rev. Lett.* 109 (Nov. 2012), p. 205304. DOI: 10.1103/PhysRevLett.109.205304.

[Ans84] F. Anselmet et al. "High-order velocity structure functions in turbulent shear flows." In: *Journal of Fluid Mechanics* 140 (Apr. 1984), pp. 63–89. DOI: 10.1017/S0022112084000513.

[Bag12] Andrew W Baggaley et al. "Thermally and mechanically driven quantum turbulence in helium II". In: *Physical Review B* 86.10 (2012), p. 104501.

[Bar14] Carlo F Barenghi, Ladislav Skrbek, and Katepalli R Sreenivasan. "Introduction to quantum turbulence". In: *Proceedings of the National Academy of Sciences* 111.Supplement 1 (2014), pp. 4647–4652.

[Bar16] CF Barenghi, YA Sergeev, and AW Baggaley. "Regimes of turbulence without an energy cascade". In: *Scientific Reports* 6 (2016).

[Bar57] John Bardeen, Leon N Cooper, and John Robert Schrieffer. "Theory of superconductivity". In: *Physical Review* 108.5 (1957), p. 1175.

[Bar83] CF Barenghi, RJ Donnelly, and WF Vinen. "Friction on quantized vortices in helium II. A review". In: *Journal of Low Temperature Physics* 52.3 (1983), pp. 189–247.

[Bau13] Stefan K Baur et al. "Collective modes of a two-dimensional spin-1/2 Fermi gas in a harmonic trap". In: *Physical Review A* 87.4 (2013), p. 043612.

[Ber17] Andrea Bergschneider. "Strong correlations in few-fermion systems". PhD thesis. Universität Heidelberg, 2017.

[Ber72] VL Berenzinskii. "Destruction of long-range order in one-dimensional and two-dimensional systems possessing a continuous symmetry group. II. Quantum systems". In: *Sov. Phys. JETP* 34 (1972), pp. 610–616.

[Bij13] Rick Martinus Wilhelmus van Bijnen. "Quantum engineering with ultracold atoms". PhD thesis. Technische Universiteit Eindhoven, 2013.

[Boe16] Igor Boettcher et al. "Equation of state of ultracold Fermions in the 2D BEC-BCS crossover region". In: *Physical review letters* 116.4 (2016), p. 045303.

[Bof12] Guido Boffetta and Robert E. Ecke. "Two-Dimensional Turbulence". In: *Annual Review of Fluid Mechanics* 44.1 (Jan. 2012), pp. 427–451. DOI: 10.1146/annurev-fluid-120710-101240.

[Bra12] Ashton S Bradley and Brian P Anderson. "Energy spectra of vortex distributions in two-dimensional quantum turbulence". In: *Physical Review X* 2.4 (2012), p. 041001.

[Bru15] Graham D Bruce et al. "Feedback-enhanced algorithm for aberration correction of holographic atom traps". In: *Journal of Physics B: Atomic, Molecular and Optical Physics* 48.11 (2015), p. 115303.

[Bul16] Aurel Bulgac, Michael McNeil Forbes, and Gabriel Wlazłowski. "Towards quantum turbulence in cold atomic fermionic superfluids". In: *Journal of Physics B: Atomic, Molecular and Optical Physics* 50.1 (2016), p. 014001.

[Cao11] Chenglin Cao et al. "Universal quantum viscosity in a unitary Fermi gas". In: *Science* 331.6013 (2011), pp. 58–61.

[Chi10] Cheng Chin et al. "Feshbach resonances in ultracold gases". In: *Reviews of Modern Physics* 82.2 (2010), p. 1225.

[Chi13] Silvia Chiacchiera et al. “Damping of the quadrupole mode in a two-dimensional Fermi gas”. In: *Physical Review A* 88.5 (2013), p. 053616.

[Cho17] Soonwon Choi et al. “Observation of discrete time-crystalline order in a disordered dipolar many-body system”. In: *Nature* 543.7644 (2017), pp. 221–225.

[Dav95] Kendall B Davis et al. “Bose-Einstein condensation in a gas of sodium atoms”. In: *Physical review letters* 75.22 (1995), p. 3969.

[Eis15] Jens Eisert, Mathis Friesdorf, and Christian Gogolin. “Quantum many-body systems out of equilibrium”. In: *Nature Physics* 11.2 (2015), pp. 124–130.

[Ens12] Tilman Enss, Carolin Küppersbusch, and Lars Fritz. “Shear viscosity and spin diffusion in a two-dimensional Fermi gas”. In: *Physical Review A* 86.1 (2012), p. 013617.

[Fey55] Richard P. Feynman. “Application of quantum mechanics to liquid helium”. In: *Progress in low temperature physics* 1 (1955), pp. 17–53. DOI: 10.1016/S0079-6417(08)60077-3.

[Fon14] Enrico Fonda et al. “Direct observation of Kelvin waves excited by quantized vortex reconnection”. In: *Proceedings of the National Academy of Sciences* 111.Supplement 1 (2014), pp. 4707–4710.

[Fri95] Uriel Frisch. *Turbulence: The Legacy of A.N. Kolmogorov.* Vol. 1. Cambridge University Press, 1995.

[Gae11] B. M. Gaensler et al. “Low-Mach-number turbulence in interstellar gas revealed by radio polarization gradients”. In: *Nature* 478.7368 (Oct. 2011), pp. 214–217. DOI: 10.1038/nature10446.

[Gao12] Chao Gao and Zhenhua Yu. “Breathing mode of two-dimensional atomic Fermi gases in harmonic traps”. In: *Physical Review A* 86.4 (2012), p. 043609.

[Gio07] Stefano Giorgini, Lev P. Pitaevskii, and Sandro Stringari. “Theory of ultracold Fermi gases”. In: (June 22, 2007). DOI: 10.1103/RevModPhys.80.1215. arXiv: 0706.3360v2 [cond-mat.other].

[Gol15] M. L. Goldstein et al. “Kinetic scale turbulence and dissipation in the solar wind: key observational results and future outlook”. In: *Philosophical Transactions of the Royal Society of London A: Mathematical, Physical and Engineering Sciences* 373.2014 (Apr. 2015), p. 20140147. DOI: 10.1098/rsta.2014.0147.

[Gri00] Rudolf Grimm, Matthias Weidemüller, and Yurii B Ovchinnikov. “Optical dipole traps for neutral atoms”. In: *Advances in atomic, molecular, and optical physics* 42 (2000), pp. 95–170.

[Had09] Zoran Hadzibabic and Jean Dalibard. “Two-dimensional Bose fluids: An atomic physics perspective”. In: *arXiv preprint arXiv:0912.1490* (2009).

[Har14] Tiffany Harte et al. “Conjugate gradient minimisation approach to generating holographic traps for ultracold atoms”. In: *Optics express* 22.22 (2014), pp. 26548–26558.

[Hen09] E. A. L. Henn et al. “Emergence of Turbulence in an Oscillating Bose-Einstein Condensate”. In: *Physical Review Letters* 103.4 (July 2009). DOI: 10.1103/physrevlett.103.045301.

[Hof12] Johannes Hofmann. “Quantum anomaly, universal relations, and breathing mode of a two-dimensional Fermi gas”. In: *Physical review letters* 108.18 (2012), p. 185303.

[Kap38] P Kapitza. “Viscosity of liquid helium below the l-point”. In: *Nature* 141.3558 (1938), p. 74.

[Kol41] A. N. Kolmogorov. “The Local Structure of Turbulence in Incompressible Viscous Fluid for Very Large Reynolds Numbers”. In: *Dokl. Akad. Nauk SSSR* 30.4 (1941), pp. 301–305.

[Kos73] John Michael Kosterlitz and David James Thouless. “Ordering, metastability and phase transitions in two-dimensional systems”. In: *Journal of Physics C: Solid State Physics* 6.7 (1973), p. 1181.

[Kra80] R. H. Kraichnan and D Montgomery. “Two-dimensional turbulence”. In: *Reports on Progress in Physics* 43.5 (May 1980), pp. 547–619. DOI: 10.1088/0034-4885/43/5/001.

[Kru05] Mark R. Krumholz and Christopher F. McKee. “A General Theory of Turbulence-regulated Star Formation, from Spirals to Ultraluminous Infrared Galaxies”. In: *The Astrophysical Journal* 630.1 (Sept. 2005), pp. 250–268. DOI: 10.1086/431734.

[Kwo14] Woo Jin Kwon et al. “Relaxation of superfluid turbulence in highly oblate Bose-Einstein condensates”. In: *Physical Review A* 90.6 (2014), p. 063627.

[Lan81] L. D. Landau and E. M. Lifshitz. *Quantum Mechanics Non-Relativistic Theory*. Elsevier LTD, Oxford, Dec. 11, 1981. 696 pp. ISBN: 0750635398. URL: http://www.ebook.de/de/product/3740084/l_d_landau_e_m_lifshitz_quantum_mechanics_non_relativistic_theory.html.

[Lan87] Lev D. Landau and Evgeny Mikhailovich Lifshitz. *Fluid mechanics*. Vol. 6. Pergamon Press, 1987.

[Mau98] J Maurer and P Tabeling. “Local investigation of superfluid turbulence”. In: *EPL (Europhysics Letters)* 43.1 (1998), p. 29.

[Mer66] N David Mermin and Herbert Wagner. “Absence of ferromagnetism or antiferromagnetism in one-or two-dimensional isotropic Heisenberg models”. In: *Physical Review Letters* 17.22 (1966), p. 1133.

[Mur14] PA Murthy et al. “Matter-wave Fourier optics with a strongly interacting two-dimensional Fermi gas”. In: *Physical Review A* 90.4 (2014), p. 043611.

[Mur15a] Simon Murmann et al. “Two fermions in a double well: Exploring a fundamental building block of the Hubbard model”. In: *Physical review letters* 114.8 (2015), p. 080402.

[Mur15b] PA Murthy et al. “Observation of the berezinskii-kosterlitz-thouless phase transition in an ultracold fermi gas”. In: *Physical review letters* 115.1 (2015), p. 010401.

[Mur17] Puneet A Murthy et al. “High temperature pairing in a strongly interacting two-dimensional Fermi gas”. In: *arXiv preprint arXiv:1705.10577* (2017).

[Nas17] Nasa. *Jupiter from Below*. NASA / JPL-Caltech / SwRI / MSSS / Roman Tkachenko. Feb. 2017.

[Nav16] Nir Navon et al. “Emergence of a turbulent cascade in a quantum gas”. In: *Nature* 539.7627 (Nov. 2016), pp. 72–75. DOI: 10.1038/nature20114.

[Naz11] Sergey Nazarenko. *Wave Turbulence*. Springer Berlin Heidelberg, 2011. DOI: 10.1007/978-3-642-15942-8.

[Nee13] T. W. Neely et al. “Characteristics of Two-Dimensional Quantum Turbulence in a Compressible Superfluid”. In: *Physical Review Letters* 111.23 (Dec. 2013). DOI: 10.1103/physrevlett.111.235301.

[Nei17] Mathias Neidig. “Many-Body Pairing in a Two-Dimensional Fermi Gas”. PhD thesis. Universität Heidelberg, 2017.

[Now13] Boris Nowak et al. “Non-thermal fixed points: universality, topology, & turbulence in Bose gases”. In: *arXiv preprint arXiv:1302.1448* (2013).

[Oku89] Akira Okubo and Simon A. Levin. “A Theoretical Framework for Data Analysis of Wind Dispersal of Seeds and Pollen”. In: *Ecology* 70.2 (Apr. 1989), pp. 329–338. DOI: 10.2307/1937537.

[Ols10] Maxim Olshanii, Hélene Perrin, and Vincent Lorent. “Example of a quantum anomaly in the physics of ultracold gases”. In: *Physical review letters* 105.9 (2010), p. 095302.

[Ons49] Lars Onsager. “Statistical hydrodynamics”. In: *L. Nuovo Cim* 6 (1949), pp. 279–287. DOI: 10.1007/BF02780991.

[Pao11] Matthew S. Paoletti and Daniel P. Lathrop. “Quantum Turbulence”. In: *Annual Review of Condensed Matter Physics* 2.1 (Mar. 2011), pp. 213–234. DOI: 10.1146/annurev-conmatphys-062910-140533.

[Pas08] Matthew Pasienski and Brian DeMarco. “A high-accuracy algorithm for designing arbitrary holographic atom traps”. In: *Optics express* 16.3 (2008), pp. 2176–2190.

[Per96] Victor M Perez-Garcia et al. “Low energy excitations of a Bose-Einstein condensate: A time-dependent variational analysis”. In: *Physical review letters* 77.27 (1996), p. 5320.

[Pet02] Christopher J Pethick and Henrik Smith. *Bose-Einstein condensation in dilute gases*. Cambridge university press, 2002.

[Pit97] LP Pitaevskii and A Rosch. “Breathing modes and hidden symmetry of trapped atoms in two dimensions”. In: *Physical Review A* 55.2 (1997), R853.

[Ran14] Mohit Randeria and Edward Taylor. “BCS-BEC crossover and the unitary Fermi gas”. In: *Annual Review of Condensed Matter Physics* 5.1 (2014), pp. 209–232.

[Ree13] Matthew T Reeves et al. “Inverse energy cascade in forced two-dimensional quantum turbulence”. In: *Physical review letters* 110.10 (2013), p. 104501.

[Ree17] Matthew T Reeves et al. “Enstrophy Cascade in Decaying Two-Dimensional Quantum Turbulence”. In: *arXiv preprint arXiv:1702.04445* (2017).

[Ric26] Lewis Fry Richardson, Oliver M. Ashford, and Philip Gerald Drazin. *The Collected Papers of Lewis Fry Richardson*. Vol. 1. CUP Archive, 1926.

[Rie08] Stefan Riedl et al. “Collective oscillations of a Fermi gas in the unitarity limit: Temperature effects and the role of pair correlations”. In: *Physical Review A* 78.5 (2008), p. 053609.

[Rie15a] Martin Gerhard Ries. “A Two-Dimensional Fermi Gas in the BEC-BCS Crossover”. PhD thesis. Universität Heidelberg, 2015.

[Rie15b] MG Ries et al. “Observation of pair condensation in the quasi-2D BEC-BCS crossover”. In: *Physical review letters* 114.23 (2015), p. 230401.

[Sch07] V. Schweikhard, S. Tung, and E. A. Cornell. “Vortex proliferation in the Berezinskii-Kosterlitz-Thouless regime on a two-dimensional lattice of Bose-Einstein condensates”. In: (Apr. 2, 2007). DOI: 10.1103/PhysRevLett.99.030401. arXiv: 0704.0289v3 [cond-mat.mes-hall].

[Sch15] Michael Schreiber et al. “Observation of many-body localization of interacting fermions in a quasirandom optical lattice”. In: *Science* 349.6250 (2015), pp. 842–845.

[Sch85] KW Schwarz. “Three-dimensional vortex dynamics in superfluid He 4: Line-line and line-boundary interactions”. In: *Physical Review B* 31.9 (1985), p. 5782.

[Ser11a] Friedhelm Serwane. “Deterministic preparation of a tunable few-fermion system”. PhD thesis. Universität Heidelberg, 2011.

[Ser11b] Friedhelm Serwane et al. "Deterministic preparation of a tunable few-fermion system". In: *Science* 332.6027 (2011), pp. 336–338.

[Set09] Gary Settles. *Candle plume imaged with schlieren mirror.* Mar. 2009.

[Skr11] L Skrbek. "Quantum turbulence". In: *Journal of Physics: Conference Series* 318 (2011). DOI: 10.1088/1742-6596/318/1/012004.

[Smi16] Jacob Smith et al. "Many-body localization in a quantum simulator with programmable random disorder". In: *Nature Physics* 12.10 (2016), pp. 907–911.

[Tay12] Edward Taylor and Mohit Randeria. "Apparent low-energy scale invariance in two-dimensional Fermi gases". In: *Physical review letters* 109.13 (2012), p. 135301.

[Tis38] Laszlo Tisza. "Transport phenomena in helium II". In: *Nature* 141.3577 (1938), p. 913.

[Tsa15] Marios C. Tsatsos et al. "Quantum turbulence in trapped atomic Bose-Einstein condensates". In: *Physics Reports 622 (2016) 1-52* (Dec. 16, 2015). DOI: 10.1016/j.physrep.2016.02.003. arXiv: 1512.05262v3 [cond-mat.quant-gas].

[Tsu08] Makoto Tsubota. "Quantum turbulence". In: *Journal of the Physical Society of Japan* 77.11 (2008), pp. 111006–111006.

[Tsu13] Makoto Tsubota. "Turbulence in quantum fluids". In: *J. Stat. Mech. (2014) P02013* (Nov. 30, 2013). DOI: 10.1088/1742-5468/2014/02/P02013. arXiv: 1312.0092v2 [cond-mat.quant-gas].

[Vog12] Enrico Vogt et al. "Scale invariance and viscosity of a two-dimensional Fermi gas". In: *Physical review letters* 108.7 (2012), p. 070404.

[Vog13] Enrico Vogt. "Collective modes and polarons in two-dimensional fermi gases". PhD thesis. University of Cambridge, 2013.

[Wen13] Andre Niklas Wenz. "From Few to Many: Ultracold Atoms in Reduced Dimensions". PhD thesis. Universität Heidelberg, 2013.

[Whi12] Angela C White, Carlo F Barenghi, and Nick P Proukakis. "Creation and characterization of vortex clusters in atomic Bose-Einstein condensates". In: *Physical Review A* 86.1 (2012), p. 013635.

[Wla15] Gabriel Wlazłowski et al. “Life cycle of superfluid vortices and quantum turbulence in the unitary Fermi gas”. In: *Physical Review A* 91.3 (2015), p. 031602.

[Wu12] Lei Wu and Yonghao Zhang. “Applicability of the Boltzmann equation for a two-dimensional Fermi gas”. In: *Physical Review A* 85.4 (2012), p. 045601.

[Zak92] Vladimir E. Zakharov, Victor S. L’vov, and Gregory Falkovich. *Kolmogorov Spectra of Turbulence I*. Vol. 1. Springer, 1992. ISBN: ISBN 978-3-642-50052-7.

[Zha17] J Zhang et al. “Observation of a discrete time crystal”. In: *Nature* 543.7644 (2017), pp. 217–220.

[Zwi05] M. W. Zwierlein et al. “Vortices and superfluidity in a strongly interacting Fermi gas”. In: *Nature* 435.7045 (June 2005), pp. 1047–1051. DOI: 10.1038/nature03858.

Danksagung

An dieser Stelle möchte ich mich bei allen bedanken die mich während der Entstehung dieser Arbeit unterstützt haben:

Zuerst bei Selim für die großartige Unterstützung und Betreuung während der letzten Jahre.

Bei allen Mitgliedern der Ultracold Gruppe für die schöne Arbeitsatmosphäre und die vielen gemeinsamen Aktivitäten auch außerhalb der Physik. Insbesondere geht mein Dank auch alle diejenigen die meine Arbeit korrekturgelesen haben.

Bei Matthias Weidemüller bedanke ich mich für die Übernahme der Zweitkorrektur dieser Arbeit.

Und zuletzt natürlich bei meiner Familie und meinen Freunden für die schöne Zeit während der letzten Jahre.

Erklärung:

Ich versichere, dass ich diese Arbeit selbstständig verfasst habe und keine anderen als die angegebenen Quellen und Hilfsmittel benutzt habe.

Heidelberg, den (Datum) . . . .